Zirconia nanocomposites for biomedical applications

Vijay Vythilingum

1.

A dissertation submitted to the Faculty of Engineering and the Built Environment, of the University of the Witwatersrand, Johannesburg, in fulfillment of the requirements for the degree of Master of Science in Engineering

Johannesburg, 2012

Declaration

I declare that this dissertation is my own unaided work. It is being submitted for the degree of Master of Science in Engineering to the University of the Witwatersrand, Johannesburg. It has not been submitted before for any degree or examination to any other university.

……...

Vijay Nadasen Vythilingum

……. Day of …….. Year ……

Abstract

Fully stabilised zirconia (8 mol% yttria) does not exhibit any transformation toughening effects such as those found in partially stabilised zirconia (3 mol% yttria), hence to produce a quality bioceramic a composite ceramic must be made, and this can further be aided by using nanopowders as the staring material. In this work nanosized reinforcing powders, titanium carbide and titanium nitride, were sintered with a nanosized fully stabilised zirconia matrix. These composites were sintered using spark plasma sintering, which allows for rapid heating and cooling rates and hence shorter sintering times. These allow for improved hardness and fracture toughnesses because of minimal grain growth during sintering.

When dealing with nanopowders, processing problems are increased due to the higher agglomeration tendencies and oxidation of the reinforcing powders. This agglomeration problem was mitigated by creating a suspension of the powders, using a suitable dispersant and solvent, thereby allowing for homogenous nanocomposites to be made. First a suitable dispersant that could disperse each of the powders had to be found. Furthermore the solvent for the dispersant had to prevent oxidation of the reinforcing powders. The dispersant and solvent were found by testing various dispersants on micron sized powders, since micron sized powders are significantly cheaper than nanosized ones. The dispersant found was Lubrizol 2155 with hexane as the solvent. Composites materials made from micron sized powders, ZrO_2-50%TiC and ZrO_2-50%TiN, were prepared and sintered using Lubrizol 2155 and hexane to determine whether it would produce a homogenous distribution of the powders in a sintered sample. These were analysed using SEM, which proved that Lubrizol was a successful dispersant. The micron sized composites were used as a comparison for the nanocomposites

Rheology studies were then carried out on the nanopowders to determine the optimal amount of dispersant and solid loadings. These were carried out on the individual nanopowders and on the ZrO_2-10vol% TiC, ZrO_2-50vol% TiC, ZrO_2-10vol% TiN and the ZrO_2-50vol% TiN nanocomposite systems. The results obtained were used to create suspensions of the nanocomposites for sintering of 3, 10, 30 and 50 volume percent of TiC and TiN respectively to the fully stabilised zirconia, these were mixed by a ball mill prior to sintering. The samples were then sintered using various conditions in the spark plasma sintering furnace.

The densification of the nanocomposites showed that there was a decrease in density with increases composition of the reinforcing powders. This was particularly apparent for the composites that contained above 30 vol. % of the reinforcing component. It is believed that this is as a result of the percolation limit being surpassed. The oxygen content also proved to be a factor in the densification.

The hardness values of the ZrO_2-TiN system were found to typically be higher than in the ZrO_2-TiC system. In both systems the highest hardness were found in the 30 volume percent samples. For the ZrO_2-TiC nanocomposites hardness values of up to 13.75 GPa were achieved, with hardness values of up to 15.79 GPa achieved for the ZrO_2-TiN system. The hardness values determined were in accordance with those found in literature.

An increase in fracture toughness with increasing the reinforcing component composition was found in both systems with higher fracture toughness found in the TiN system. The highest fracture toughnesses were found for samples with a relative density above 97 percent, were 2.65 and 3.64 $MPa.m^{1/2}$ respectively for the TiC and TiN systems. These values were slightly higher than those found in literature for fully stabilised zirconia, however were significantly lower than partially stabilised zirconia composites found in literature.

Table of Contents

List of Figures

List of Tables

1. Introduction

Zirconia ceramics have been widely developed for bioceramic applications due to their chemical inertness and hardness. These properties are exploited for implant purposes, where zirconia ceramics are used as the structural parts in hip and knee joints [(1)]. Zirconia has properties that overcome the problem associated with alumina bioceramics i.e. the brittleness of that material. This is most evident in partially stabilised zirconia (3Y-ZrO_2, 3 mol% yttria), which has a phase transformation toughening mechanism that helps prevent cracks from propagating. However, partially stabilised zirconia in the presence of bodily fluids undergoes an undesirable roughening of the surface and micro-cracking [(2) (3)].

Fully stabilised zirconia (8Y-ZrO_2, 8 mol% yttria) does not exhibit this transformation and hence may overcome this problem; however, because of this it has lower fracture toughness than partially stabilised zirconia. Furthermore it exhibits significantly higher grain growth during sintering than partially stabilised zirconia [(4)], with similar hardness values. Because of these properties of 8Y-ZrO_2 quality bioceramics can potentially be produced by making composites comprising of 8Y-ZrO_2 as matrix and a reinforcing, hard second phase, such as TiC or TiN. Furthermore, better properties of such composites may be realized if nanosized powders are used as starting materials.

Titanium carbide and titanium nitride have shown great potential in orthopaedic materials; this is due to their chemical inertness and resilience in harsh mechanical and chemical environments [(5)]. Nanoceramics have been widely developed in the past few years and have been shown to improve certain properties of materials due to the resulting nanoscale microstructure [(6)].

Hence creating a composite of 8Y-ZrO_2 with titanium carbide or titanium nitride as reinforcing powders could increase the mechanical properties and reduce grain growth during sintering. Furthermore by creating a nanocomposite of these materials, by using nanosized staring powders, could minimise the final grain size of the zirconia grains and also produce a ceramic with better mechanical properties. However, with the use of nanopowder comes greater processing risks such as contamination and agglomeration [(7)].

Thus the main aim this work is to successfully sinter ceramic nanocomposites of zirconia(8Y)-titanium carbide and zirconia(8Y)-titanium nitride, by overcoming the technical difficulties involved in development of nanocomposite materials. The main difficulties being to produce a homogeneous mixture of zirconia and reinforcing powder, due to the greater agglomeration tendencies of nanopowders, and to minimise the oxidation of the reinforcing powders during processing. This can be done through the optimisation of the particle suspensions by electrostatic dispersion and the use of surfactants.

Furthermore, investigation into whether titanium carbide or titanium nitride will improve the mechanical properties of the zirconia nanocomposite will be made. Likewise the optimal sintering conditions and compositions of these nanocomposites will be investigated. This will be achieved by establishing the densification mechanisms and sintering kinetics of the system at different sintering temperatures, pressures and times.

The optimization of the suspension will be carried out using a rheometer, with the optimal dispersant and solvent having to be found first. The consolidation of the composites will be carried out through the use spark plasma sintering (SPS). This technique offers high heating and cooling rates with an applied pressure. This would reduce grain growth during sintering because the overall sintering time is significantly reduced, and potentially ensure that the composites will have a nanoscale microstructure.

2. Literature Review

2.1 Introduction

This section will summarise the literature associated with this project. It will first discuss, in a summary format what bioceramics are, some of the most popular bioceramics and their chemical and physical properties. This will be followed by what nanoceramics are, the need and typical route to create suspensions for nanoceramic powders, a comparison between the different types of zirconia available and finally some of the sintering techniques that have been successful in creating zirconia nanocomposite ceramics.

2.2 Bioceramics

2.2.1 Introduction

The innovation of ceramics materials for skeletal reconstruction and repair has been one of the major advances in medical materials in recent times [(8)]. These materials are often referred to as bioceramics, because they are biocompatible with the human body. The materials used include: glasses, glass ceramics and ceramic-filled bioactive composites. All these may be manufactured either in porous or in dense form in bulk, as granules or in the form of coatings [(8)].

Bioceramics can be produced in crystalline and amorphous forms, and they are generally classified from their chemical compositions into two groups: calcium phosphates (CP) and others [(2)]. They can be further classified largely into three divisions according to their properties, functions, types of bioceramics used and their interaction with the host tissue [(8)]. These are bio-inert, bioactive and bio-absorbable. Bio-inert ceramics are chemically stable, bioactive ceramics are those which combine with bones directly, and bio-absorbable ceramics are those which undergo decomposition and absorption in perspective of chemical reactivity [(9)].

The desirable properties of biomaterial implants are summarised below [(10)]. They need to:

- Be non-toxic.
- Be mechanically stable i.e. do not fracture, or deform excessively.
- Have no foreign body reaction.

- Not stimulate of undesirable growths or chemical reactions in body fluids and tissues.
- Either: Not dissolve or corrode
  Or: Resorb at a desired rate.

2.2.2 Biocompatibility

Before any materials can be placed in the human body they must be tested for their biocompatibility. There are four main responses an implant can have with the surrounding tissue, as are listed below [11]:

- If the material is toxic, the surrounding tissue dies.
- If the material is nontoxic and biologically inactive (nearly inert), a fibrous tissue of variable thickness forms.
- If the material is non-toxic and biologically active (bioactive), an interfacial bond forms.
- If the material is non-toxic and dissolves, the surrounding tissue replaces it.

For solid materials to be biocompatible they must elicit a minimum of adverse reactions in the human body. These adverse reactions can result from several causes, such as direct toxicity of the implant materials to tissue as well as the organs, and the toxicity of products from the implant which can negatively impact tissue and organs [10].

Certain foreign solid materials, when placed in the human body may provoke an undesirable foreign body reaction. This occurs when cells and proteins from blood and neighbouring tissues try to remove the foreign material by attempting to encapsulate it; such a severe local foreign body reaction can destroy physiological functions and cause tissue damage [10].

2.2.3 Current Biomaterials

Some of the current biomaterials are summarised in this section.

2.2.3.1 Alumina

Alumina (Al_2O_3) is the most widely used oxide ceramic material [2]. It has mechanical properties that make it very attractive for dental and bone implants, since it is very hard

compared to most ceramics, chemically durable and stable even at high temperatures [10]. Furthermore it has low friction and excellent wear and corrosion resistance [2].

High purity alumina ceramics with purity greater than 99.99%, have been developed for orthopaedic applications as alternatives for metal alloys for hip replacement applications. For this purpose the material must be free of porosity and it must have a fine and homogeneous microstructure, as this will allow the material to achieve a long-term stability [2].

However the main problem with alumina is its brittleness, which makes parts made with it to be prone to fracture. This hard but brittle combination of material properties means that certain design restrictions apply [2].

2.2.3.2 A-W glass-ceramic

Apatite-wollastonite glass-ceramic is an assembly of small apatite particles effectively reinforced by wollastonite, and is used as a bone substitute. It is a dense and homogeneous composite, which comprises the following: 28 weight percent Wollastonite, 34 weight percent Oxyfluoroapatite and 28 weight percent Glass [8].

The bending strength, fracture toughness and Young's modulus of A-W glass-ceramic are the highest among bioactive glass and glass ceramics, enabling it to be used in some major compression load bearing applications [8].

2.2.3.3 Bioglass

Bioglass was developed because of the need for materials that would help in the repair of tissues by forming a direct bond with them rather than the interfacial scar tissue as is the case with metallic and polymetric implants [8].

Bioglasses are amorphous silicate based materials that are biocompatible with the human body. They bond directly to the bone and while dissolving over time, they can stimulate new bone growth. Through this process they have the ability to restore diseased or damaged bone to its original state and function [2].

45S5 Bioglass, bioglass with a composition of 45 weight percent SiO_2 and a ratio of CaO to P_2O_5 of 5, undergoes a complex surface reaction which occurs very rapidly, this is a multi-

staged process which results in the formation of a biologically active hydroxy-carbonate apatite (HCA) layer that is chemically and structurally similar to the mineral phase in bone [8].

2.2.3.4 Biolox

There are two separate types of Biolox materials which are both produced by CeramTec; these are Biolox Forte and Biolox Delta. Biolox Forte is a pure alumina material while Biolox Delta is an alumina matrix composite material. Biolox Delta has been engineered to improve the mechanical properties of pure alumina so that new applications can be developed such as spine and knee components as well as larger and thinner components compared to Biolox Forte [2].

Table 1: The physical and mechanical properties of Biolox® Delta and Forte **[2]**

Property	**Biolox Delta**	**Biolox Forte**
Density (g/cm_3)	>4.36	3.9
Young's modulus (GPa)	350	380
Flexural strength (MPa)	1203 ± 101	466 ± 106
Fracture toughness ($MPom_{1/2}$)	4.1	2.75
Hardness (HV)	1840 ± 60	1878 ± 60
Grain size (µm)	0.6	3

Biolox Forte

Biolox Forte is a bioinert material which has excellent dimensional stability, is highly resistant to all chemical reactions and has extremely good corrosion resistance, because of the strong bond between aluminium and oxygen atoms. This is the main reason for its excellent biocompatibility with the human body. It has a high Vickers hardness, approximately three times that of metal, and it remains undamaged if scratched during implantation. This is not the case with metals on the surface of which a groove would form over time. It also possesses other excellent mechanical properties such as extremely high elastic modulus and high compressive strengths [2].

Biolox Delta

Biolox Delta is an alumina matrix composite composed of approximately 75% alumina and approximately 25% yttria-stabilised tetragonal polycrystalline zirconia (Y-TZP). It combines

the excellent material properties of alumina and zirconia. Other additives provide improved mechanical properties. Alumina has excellent ceramic properties in terms of its chemical and hydrothermal stability with extremely low wear, good mechanical strength and fracture toughness. The increase in strength and toughness is attributable to the stress-induced transformation-toughening mechanism of partially stabilized zirconia as a result of the introduction of the optimal amounts of fine zirconia particles. This toughening mechanism is achieved through the transformation of the zirconia particles from the metastable tetragonal phase to the stable monoclinic phase as a crack propagates grows through the ceramic. This change is associated with a 3-4% volume increase. This in turn produces compressive stresses in the alumina matrix at the proximity of the crack tip. These stresses close the crack and act as an energy barrier to further crack growth [(2)].

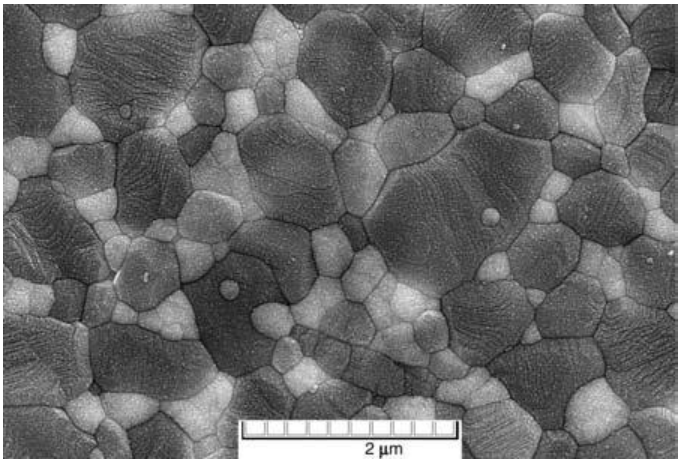

Figure 1: SEM image of Biolox® Delta showing alumina matrix grains, zirconia grains and mixed oxide platelets **[(2)]**

The microstructure of Biolox Delta is shown in Figure 1. The dark grains are the alumina matrix which are generally less than 0.8 µm in size. Within this matrix are smaller light-coloured grains of zirconia and fewer elongated oxides of chromium and strontium [(2)].

2.2.3.5 Zirconia

Zirconia was introduced in orthopaedics to overcome the problem of alumina brittleness, alumina being the most widely used oxide bioceramic. The remarkable mechanical properties of zirconia are mainly due to the tetragonal to monoclinic phase transformation. This transformation, which can be induced by external stresses, results in a 4% increase of volume. That causes localized compressive stresses to develop about the crack tip, and for a crack to propagate this clamping constraint must be overcome. This property explains the

increased fracture toughness of zirconia compared with other ceramics [2]. This phase transformation from tetragonal to monoclinic can only occur above a critical grain size; this critical grain size was reported to be 18 nm [12].

The main problems with zirconia bioceramics are also due to the phase transformation described above. Phase transformation is beneficial when localized and confined around a propagating crack, but it may also occur at the surface of the bioceramic implants in the presence of body fluids. This leads to progressive roughening and micro-cracking, often referred to as ageing [2].

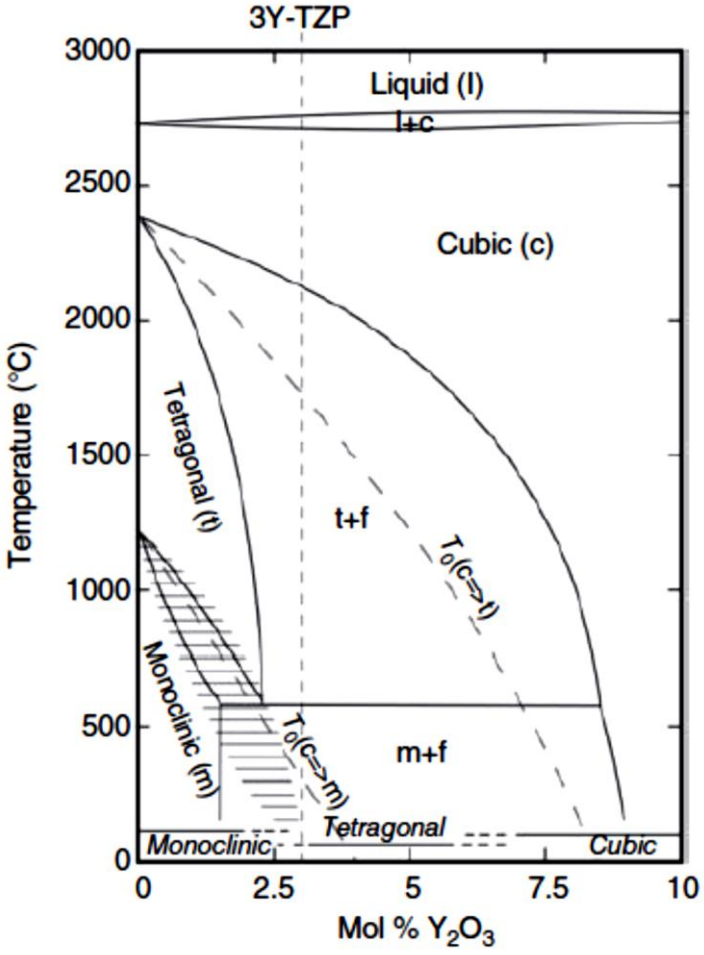

Figure 2: ZrO_2-Y_2O_3 Phase Diagram **[13]**

The transformation toughening of zirconia hinges upon stabilizing the high temperature tetragonal form. Partial or whole stabilization is achieved by adding certain oxides, of which the most commonly used are Y_2O_3, MgO, and CaO [13]. For this review only yttria (Y_2O_3) will be examined. The zirconia-yttira phase diagram is shown in Figure 2. There are three

main zirconia based types of ceramics; these are termed CSZ, TZP and PSZ. The term CSZ, cubic-stabilized zirconia, refers to material with a fully-stabilized cubic (not tetragonal) crystal structure which cannot take advantage of the toughening phase transformation mechanism [(13)]. TZP, tetragonal zirconia polycrystal, contains the least amount of oxide additive, with a structure that is in essence single-phase; this material is several times stronger than other types of zirconia-toughened ceramics. In partially-stabilized zirconia, PSZ, small tetragonal-crystals are dispersed as a precipitate throughout a matrix of coarser cubic grains [(14)].

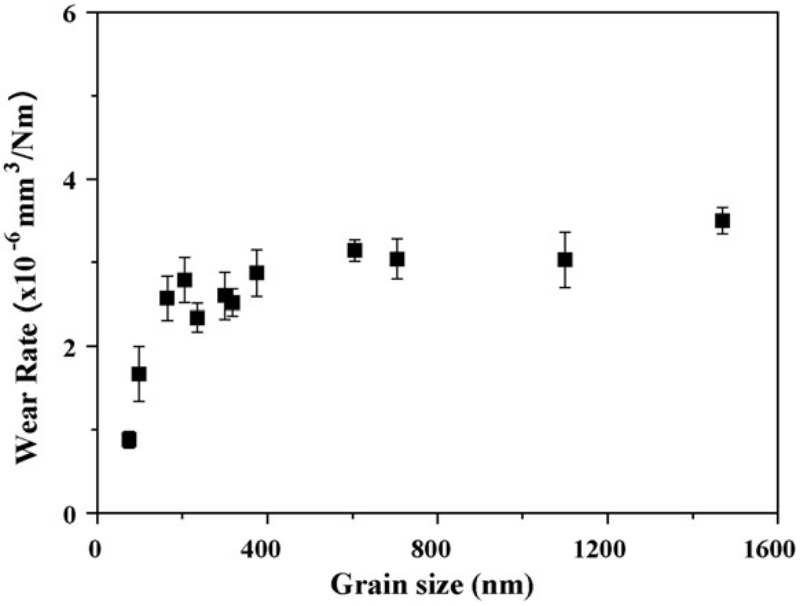

Figure 3: Wear rate with grain size in the developed Y-TZP ceramics **[(15)]**

Particle size plays an important role in ceramic properties. In a study on the effect of grain size on wear behaviour of zirconia ceramics, it was found that the wear rate decreases with decreasing grain size, as shown in the figure above [(15)]. The grain size however should not be below 18 nm, the critical grain size, as at this point a decrease in grain size results in a decrease in hardness [(16)]; hence a grain size close to the critical grain size will be most favourable. Furthermore, for zirconia, the grain size should not be below 18 nm, as phase transformation from tetragonal to monoclinic can occur only above a critical grain size of 18 nm [(12)].

Cubic zirconia, CSZ, is stabilized with yttria and is formed using higher concentrations of yttria (Y_2O_3), compared to other zirconia types. The application of this type of cubic zirconia is often limited by the high sintering temperature, lack of transformation toughening and

severe grain growth [17] [13]. CSZ is reported to have large grains, greater than 10 µm, and high grain growth rate ranging from 30 to 250 times greater than tetragonal yttria stabilized zirconia (Y-TZP) [4]. This is shown in Figure 4 below, which shows a comparison between the differences in grain sizes for similar processed 3 mol% Y_2O_3-TZP (3Y-TZP) and 8 mol% Y_2O_3-CSZ (8Y-CSZ), each having a starting powder size of 20 nm and sintered at the same temperature of 1400°C.

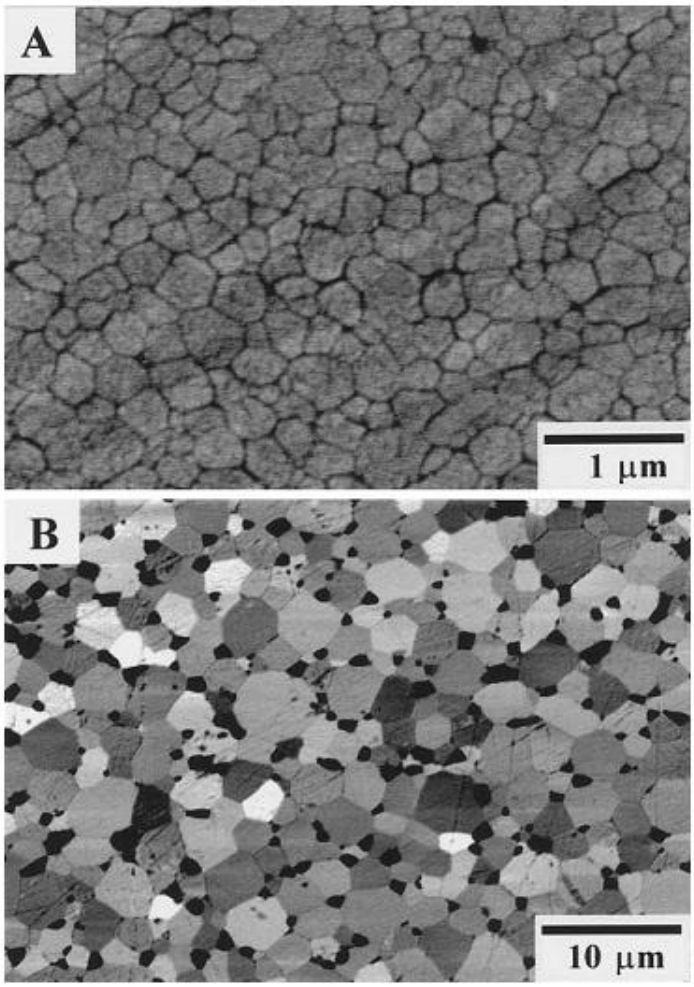

Figure 4: Difference in grain sizes of (A) 3Y-TZP and (B) 8Y-CSZ both sintered at 1400°C **(4)**

2.3 Nanoceramics

Nanoceramics/nanocomposites are defined as novel bulk materials or coatings with microstructural architecture, characterized by at least one of the ceramic phases having a length scale between 1 and 100 nm. The major drive for wider interest in nanoceramics and its composites has been the fact that one can potentially achieve better and in some cases

unusual material properties by manipulating the length scale in the nano range. Therefore, better performance and newer applications of the materials have now been made possible [6].

2.3.1 Suspensions

Agglomeration needs to be avoided when dealing with powders. Nano-sized powder particles, because they have a large surface area, are prone to agglomeration to minimize the total surface area or interfacial area of the system. The driving force of this agglomeration is caused by the attractive van der Waals forces acting between the particles [18]. As a result of this agglomeration tendency, problems arise when trying to create a homogenous mixture of nano-sized particles. This has to be overcome if a high quality nanoceramic is to be produced; a general practice in dealing with this issue is to create a stable suspension, in which all particles repel each other. This is achieved through the use of dispersing agents and adjusting the pH [19]. The optimum pH or amount of dispersant to create a stable suspension can be experimentally found through rheological measurements.

Rheology is the science of deformation and flow characteristics of matter. During rheological measurements the flow behavior is monitored in a response to an applied shear stress. A key rheological parameter is the viscosity of suspensions. Rheological measurements are necessary to characterize the properties of colloidal suspensions; specifically such measurements are used in order to determine the optimal amount of dispersant required to stabilize a suspension. This is done by measuring the viscosity of a suspension against varying dispersant concentrations [20].

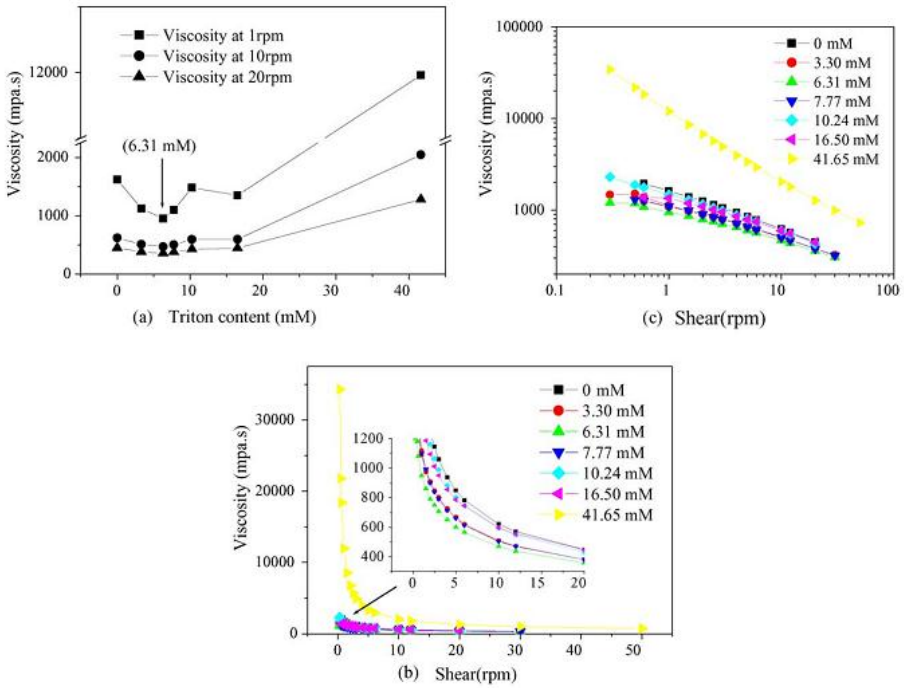

Figure 5: Viscosity of 35 vol% ZrO_2 slurries vs. Triton X-114 content (pH = 6±0.1): (a) viscosity at different shear conditions; (b) linear coordinate; (c) logarithm coordinates [21]

Figure 5, above, shows the viscosity of a 35% volume percent slurry as a function of varying dispersant content. The dispersant tested was Triton X-114, and the test was conducted at a pH of 6 [21]. It can be seen in the figure that as the dispersant content increases the viscosity of the slurry decreases until an optimum amount of dispersant is reached at 6.31 mM, after which a further increase in the dispersant concentration results in an increase in the viscosity of the slurry.

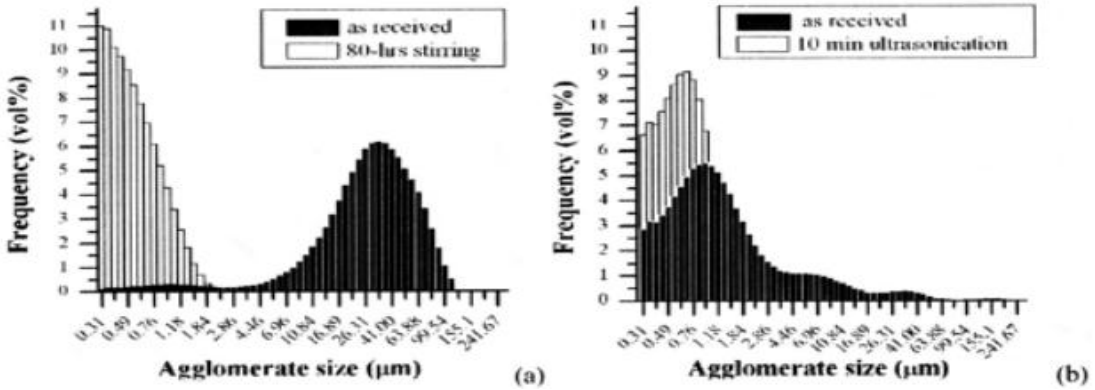

Figure 6: Granulometric analyses of received and dispersed powders: a) alumina; b) zirconia [22]

Figure 6, above shows the particle size distribution by volume of two powders, alumina (a) and zirconia (b), as received and after dispersion. The wide particle size distributions of each of the powders are a result of large agglomerates, which could be broken down by 80 hours of magnetic stirring and 10 minutes of ultrasonic dispersion [22].

A study by Donzel and Roberts [23] shows that the dispersion of zirconia to achieve a stable suspension can be done by first ultrasonically dispersing the powder for 20 minutes and then adding the dispersive agent Dispex A4. Dolapix CE64 is a suitable dispersant for sub-micron zirconia particles; it was shown that 8 mg of this dispersant per gram of zirconia was the optimum dosage; at this concentration, Dolapix CE64 could disperse a solids loading of about 60 wt% at pH 8 [24]. In one case no dispersants were used and zirconia was ball mixed with ethanol and then sieved to remove the hard agglomerates, which still produced a composite with a density greater than 99% [25]. Another suitable dispersant for zirconia was found to be Triton X-114 at a pH=4 with a concentration of 6 mM; at this configuration, this dispersant could successfully disperse up to 45 vol% solids loading [21].

2.3.2 Sintering

2.3.2.1. Spark Plasma Sintering

Spark Plasma Sintering (SPS), also known as Field Assisted Sintering, or Pulsed Electric Current Sintering (PECS) is a sintering technique that involves passing a DC current pulse through a powder compact contained in a graphite die, under an applied pressure of 30–50 MPa; this technique allows the production of fully dense materials within minutes while applying high heating rates (in excess of 200°C) and short dwell times. [19] The high heating rates are a result of the use of direct heating current passing through the graphite die which is in close thermal contact with the sample. The same rates can be achieved even if the sample is not electrically conducting, as all heating is generated in the graphite die set [26]. The main advantage of using SPS is that high densification rates may be achieved with minimal grain growth. This is ideal for producing dense ceramics from nanosized powders [19].

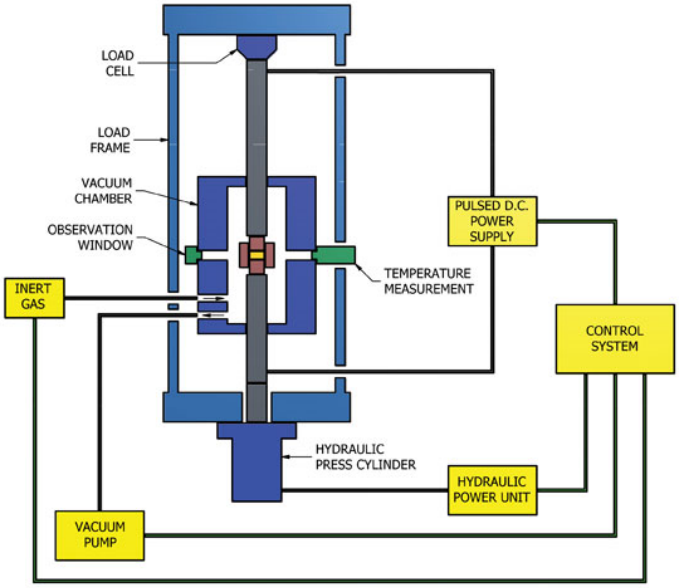

Figure 7: Basic configuration of an SPS machine [27]

2.3.2.2. Hot Press Sintering

Sintering while using heat and pressure is termed hot press sintering, if the applied pressure is uniaxial. [29]. Hot press sintering is a solution to inadequate densification during heating in either the case of solid-state or liquid-phase sintering. The applied pressure has the effect of increasing the driving force for densification without significantly affecting grain growth [19].

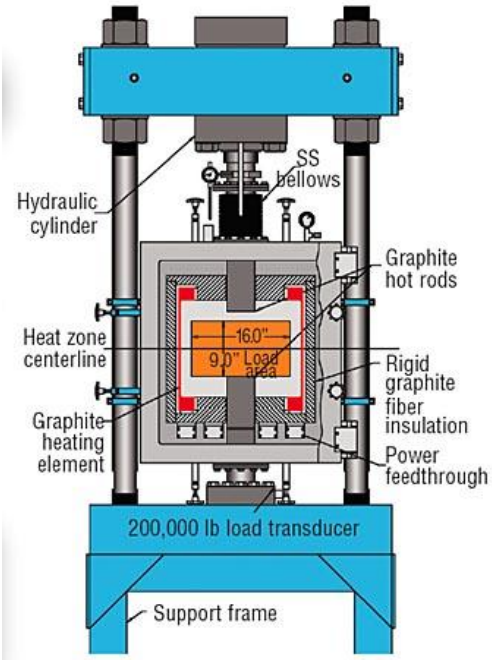

Figure 8: Cross section of 100-ton hot press furnace with graphite hot zone [28]

2.3.2.3. Sintering of Zirconia

SPS, Spark-plasma sintering, in a relatively new sintering technique which allows for the rapid consolidation of ceramic materials in a short time compared to conventional sintering [30]. The shorter sintering time and high heating rates, are advantageous in suppressing exaggerated grain growth, which allows for superior mechanical properties, if the ceramic produced is near the theoretical density [30]. The mechanical properties for fully stabilized zirconia (8YSZ) have been increased while using SPS sintering as a result of the grain growth being limited [31].

Spark plasma sintering (SPS) of zirconia nano-particles was found to produce high density nanoceramics with up to 99% of theoretical density [32] [33]. A Vickers hardness of 13.76 GPa with a fracture toughness of 15.4 $MPa.m^{1/2}$ was achieved for a sintering temperature of 1300°C [33]. SPS was also shown to be effective in producing fully densified nanocrystalline zirconia at a low temperature and short sintering time as compared to that of hot press sintering [15]. The mechanical properties of some zirconia nanoceramics and nanocomposites, sintered by SPS and hot pressing, are summarised in the table below.

Table 2: Mechanical properties of nanoceramics and nanocomposites [34], [35], [23], [36], [37] [38], [39], [2] [11]

Material	Preparation Method	Relative Density (%)	Hardness (GPa)	Fracture Toughness ($MPa.m^{1/2}$)	Bending Strength (GPa)
3Y-ZrO_2	SPS, 1300°C, 50 MPa, 5 min	>99%	13.3	5.3	-
3Y-ZrO_2	SPS, 1500°C, 50 MPa, 5 min	>99%	12.8	5.39	-
3Y-ZrO_2	HP, 1225°C, 160 MPa, 60 min	99.50%	12.9	>5	910
8Y-ZrO_2/ 5 vol. % SiC	HP, 1710°C, 20 MPa, 60 min	99.80%	13.81	1.27	-
8Y-ZrO_2/ 5 vol. % SiC	HP, 1680°C, 20 MPa, 60 min	99.70%	14.98	1.95	-
8Y-ZrO_2/ 5 vol. % SiC	HP, 1300°C, 20 MPa, 60 min	99.70%	15.02	1.47	-
3Y-ZrO_2/ 8.3 vol. % TiC	HP, 1500°C, 25 MPa, 60 min	>98%	17	4.1	-
3Y-ZrO_2/ 9.39 vol. % TiC	HP, 1450°C, 25 MPa, 60 min	97.8%	14.9	4.2	-
3Y-ZrO_2/ 9.39 vol. % TiC	HP, 1500°C, 25 MPa, 60 min	98.3	17	4.1	-
3Y-ZrO_2/ 20 vol. % TiN	HP, 1500°C, 30 MPa, 60 min	>98.5%	14.9	4.4	900
3Y-ZrO_2/ 35 vol. % TiN	HP, 1550°C, 28 MPa, 60 min	99-100%	13.75	7.1	909
3Y-ZrO_2/ 50 vol. % TiN	HP, 1550°C, 28 MPa, 60 min	99-100%	13.49	6.3	1429
3Y-ZrO_2/ 10 mol% Al2O3	SPS, 1300°C, 50 MPa, 5 min	>99%	14.6	5.91	-
3Y-ZrO_2/ 10 mol% Al2O3	SPS, 1500°C, 50 MPa, 5 min	>99%	13.9	6.5	-

Densification of ceramics is mainly a process of eliminating voids in the unsintered compacts through the use of elevated temperature. During heating, shrinkage and grain growth may take place simultaneously to different extents. Exaggerated grain growth is in general most undesirable, primarily because it decreases the final density and degrades the final properties of the ceramic products. Therefore, the control of grain growth, in most cases, is one of the most important subjects on densification [(40)].

The advancement of powder processing technology makes ceramic products with a high relative density and ultrafine microstructure highly feasible. Starting with ultrafine and pure powder particles are the issues principally responsible for the resulting ultrafine microstructure. Therefore, the use of ultrafine pure ceramic powders has become one of the increasingly important considerations in the fabrication of advanced ceramics. Furthermore, the smaller the powder particle size used, the lower is the temperature required to achieve full density and this may ensure to some extent a finer microstructure [(40)].

Grain growth in ceramics has to be limited so that the ceramics produced will be nanostructured. This is achievable by using SPS under high pressure. This approach can deliver dense compacts with nanosized grains [(41)].

3. Experimental Procedure

3.1. Materials Used

The materials used in the project are summarised in the table below, with specific supplier information.

Table 3: Summary of Materials used

Material	**Mean Particle Size (from Supplier)**	**Specific Surface Area (m^2/g) (from Supplier)**	**Purity (%)**	**Density (g/ cm^3)**	**Supplier**
8Y-ZrO_2 (submicron)	~700 nm	5.5 m^2/g	99.9% trace metals basis (purity excludes ~2% HfO_2)		Sigma-Aldrich
8Y-ZrO_2 (nano)	28 nm	16±3 m^2/g	-	5.90	Tosoh
3Y-ZrO_2 (nano)	26 nm	16±3 m^2/g	-	6.05	Tosoh
TiC (micron)	-	-	-		Element Six
TiC (nano)	20 nm	-	99+% Nano	4,930	Abcr
TiN (micron)	-	-	-		Element Six
TiN (nano)	40 nm	40-55 m^2/g	97+% Nano	5,220	Abcr
Lubrizol	-	-	-		Carst and Walker
Hexane	-	-			Merck

3.2. Powder Characterisation

This section will describe all the equipment used to characterise the powders as received from the suppliers.

3.2.1. Particle size distribution

3.2.1.1. Micron Powders

The micron sized particle size distribution was analysed on a Malvern Mastersizer 2000. This can measure particles in the size region of 0.01 μm to 3 mm and so was used for the coarser powders.

Before each particle size analysis, the Malvern Mastersizer was cleaned of any remnant slurry to avoid contamination of the sample. The instrument was cleaned by circulating 600 ml of distilled water through the tubing for 3-5 minutes.

The powders were made into a weak suspension and dispersed using ultrasonic and the dispersant hexa-meta-phosphate. Small amounts of this suspension were added to a 500 ml beaker with distilled water, until the obscuration was between 10-20%. The particle size was then measured 3 times and an average particle size distribution was generated by the instruments software.

3.2.1.2. Nano powders

The nano sized particles were analysed on a Malvern Zetasizer Nano ZS, which measures the particle size distribution using dynamic light scattering.

The nanopowders were milled for varying times depending on how long it took to break up the agglomerates and achieve a unimodal particle size distribution. This was done in hexane and with dispersant Lubrizol 2155, in a ball mill using a zirconia milling pot, and the particle size was analysed every 30 minutes. 1 g of zirconia and 0.5 g of TiC and TiN were milled, each separately. 0.1 ml of this milled powder was mixed with 0.9 ml of hexane, to ensure that the attenuation reading is between 6 and 9. An average was taken from three measurements which each consist of 12 runs.

3.2.2. Specific Surface Area

The specific area of all powders was determined by nitrogen adsorption using the multipoint BET method on a Quantachrome Autosorb-1. The BET technique makes use of pressure/volume measurements to determine the amount of adsorbate gas before and after exposure to the adsorbent. As adsorption or desorption occur the pressure in the sample cell changes until equilibrium pressure reflects the difference between the amount of gas admitted or removed and the amount required to fill the space around the adsorbent.

At least about 0.2 g of samples were degassed in N_2 at 150°C for 4 hours prior to analysis using a Micromeritics Flow Prep 060, sample degas system. The surface areas and pore size distributions were then obtained at 196°C. The pore size distribution with specific surface areas of the samples were determined via N_2 adsorption/desorption according to the BET method using a Micromeritics Tristar, surface area and porosity analyzer. In order to confirm the accuracy of the results, the analysis was repeated at least twice for all samples and the measurements were in good agreement.

3.2.3. XRD analysis

The analytical technique which was used to characterize the ceramic powders was X-Ray Diffraction (XRD). The phase purity was determined by X-ray diffraction, using a Bruker D2 phaser XRD machine. This uses Cu Kα irradiation operated at 30 kV and 10 mA. All measurements were taken using a step scan of 0.020^0 recorded in the 2θ regime of $10\text{-}90^0$. Patterns were collected and phase identification was done using X'Pert HighScore software containing ICDD (International Centre for Diffraction Data) files for comparison.

3.2.4. SEM

Scanning electron microscopy (SEM) was used to analyze the size of the powders and determine the extent of agglomeration. Two separate SEM microscopes were used depending on which one was available. Of the two microscopes used, the one was a FEI Quanta 400 FEG, located in the biology building at the University of the Witwatersrand. The other SEM used was a Philips XL30 FEG ESEM and was located at Elememt Six. Both microscopes that were used could operate at high maginifications with high resolutions in both secondary electron and back-scatter modes.

A small amount of the ceramic powder was sprinkled carefully on a double sided graphite tape which was stuck on a stub. The stub, with the powder, was then carbon coated twice to ensure conduction of the powders. The coated stubs were then placed in the SEM and analysed.

3.3. Dispersion

This section describes the dispersion studies carried out firstly to find a suitable dispersant for the each powder and secondly to determine the optimum amount of the dispersant for each individual powder and mixture of powders.

3.3.1. Dispersant

The correct dispersant used for the rheology studies was found by testing a number of dispersants on micron sized ZrO_2, TiC and TiN. The dispersants tested were PEG 200, PEG 400, Dolapix CE 64 and Lubrizol 2155.

This was done by creating a 'test' suspension from each powder, with a solids loading of 30%. Dispersants were added in small increments until the suspension was dispersed or it was decided that the dispersant was not suitable for the system.

3.3.2. Rheological Measurement

The rheological properties of the slurry were measured by an Anton Paar RheolabQC rheometer with a concentric cylinder (CC27/P1) with a gap between the inner and outer cylinder walls of 1.33 mm. This is a computer controlled rheometer system with Rheoplus software. This instrument was used to measure the rheological properties of liquid or paste-like materials. The measuring cup used had a concentric geometry which required a sample volume of 22 ml.

It was found that Lubrizol 2155 was the most suitable dispersant for each powder. Hence for the Rheological measurements Lubrizol 2155 was used with hexane as the solvent.

A suspension was created by mixing relevant amounts of powder to hexane and the appropriate weight percent dispersant, to obtain 24 ml of suspension. The suspension was weighed immediately so that the amount of hexane evaporated prior to the rheology

measurement could be known. It was then dispersed for 10 minutes in an ultrasonic bath, reweighed and topped up with hexane and lightly stirred, before the measuring cup was filled with 22 ml of suspension. The measuring cell was inserted into the cup. Using the measuring profile flow curve/with pre-shear the sample was presheared for 160 seconds to ensure thorough blending of ingredients, and held for 30 seconds before each measurement. The viscosity was monitored over the entire shear rate range between 0 and 1000 s^{-1}.

3.4. Powders Preparation

3.4.1. Milling

A planetary mill, Fritsch Pulverisette 6, was used during wet mixing of powders, using hexane as a solvent and Lubrizol 2155 as a dispersant; the amount of the dispersant for each system was found in the rheology study.

The mixing of the nanopowders was done using a zirconia lined milling pot of the above planetary ball mill, with a capacity of 250 ml. Zirconia balls of 2.5 mm in diameter were used as milling media. The mill was operated at a speed of 300 rpm for 4 hours.

The mixing of the micron powders was done using the same operating conditions but in a tungsten carbide milling pot and using 2 mm alumina balls.

3.4.2. Drying

After the mixing process the powder mixtures were dried using a rotary evaporator. A Heidolph laborota 4010 digital rotary evaporator was used which has a speed range of 20 – 270 rpm, a power dissipation of 1410 W, a 1000 mL evaporating round bottomed flask and a 1000 mL receiving flask. The bath was able to operate from 20°C to 180°C; however if water was used in the bath a maximum of 100°C is recommended. The evaporator has a digital display of water bath temperature and rotation speed. The powder inside the evaporating flask is dried by the heating from the water bath and the vacuum pressure from the condenser tube. The solvent evaporated up the condenser tube where it is condensed due to cold water running inside the tube. This condensed solvent flowed into the receiving flask. The rotary evaporator was operated at a speed of 120 rpm with a bath temperature of 60°C.

3.4.3. Sieving

After drying, the powders were sieved. This was done using Retsch test sieves with an inner diameter of 200 mm and a height of 50 mm. The sieving was done with a large mesh size and decreased to a small one. The sieves used had a mesh size of 400 μm, 250 μm and 150 μm , in descending order. The sieving was carried out by hand in a glove bag under an inert atmosphere of argon, to prevent oxidation through exposure to air. The sieved powders were stored in containers, in a vacuum desiccator, before the Lubrizol was burned out.

3.4.4. Dispersant Burnout

A tube furnace (Elite TSH17/75/150/Elite Thermal Systems Limited) with capabilities of running to a maximum temperature of 1600^{o}C was used for the Lubrizol burnout. The ceramic tube is made of aluminium oxide. Rectangular alumina crucibles were used as the sample holder and placed at the centre (hot zone area) of the tube furnace. The furnace had a Eurotherm microprocessor that controlled the temperature profile executed during the burnout. The burnout was carried out at a temperature of 500°C for an hour, using a ramp rate of 5°C/min, in an inert atmosphere of 5% H_2 – Argon gas.

After the burnout, the samples in the crucibles were transported immediately into glove bags, so as to prevent exposure to air, and weighed into vials. The amounts of powder weighed were such that samples of 20 mm in diameter and 4 mm thick, when fully dense, could be produced. The vials were then stored under an inert atmosphere in a desiccator.

3.5. Sintering

All the composite powders were sintered in a Spark Plasma Sintering (SPS) / Field Assisted Sintering (FAST) furnace, FCT HP-D5. A heating rate of 250°C/min was used and slowed to 100°C/min for the final 100°C before the final sintering temperature was reached; this is to ensure that the temperature did not overshoot the sintering temperature. The samples were sintered for 5 minutes at the sintering temperature and cooled at a rate of 250°C/min. A pressure of 30 MPa or 50 MPa was used for the various samples sintered; the pressure was first applied. This was followed by application of heat after the full load had been applied. The load was released during the cooling stage at 1000°C.

3.6. Sample Characterisation

3.6.1. Density and Open Porosity

Density and open porosity measurements were done based upon Archimedes principle. Each of the compacts was boiled in distilled water for 3 hours to replace the air in the surface pores with water, using a hot plate.

After boiling, the mass of the compact, when suspended in water was measured. This is referred to as the suspended mass (W_3). The compacts were then lightly rubbed dry and weighed in air. This was called the wet mass (W_2). The compacts were then dried at 120^{o}C for 20 minutes to remove all the water from the pores. The dried compacts were then weighed in air. Their mass is referred to as dry mass (W_1). The density of water is symbolised by ρ_w.

This enables the bulk density and open porosity of samples to be determined by making use of the following equations from German [42]. The derivations of these equations are shown in Appendix A – Archimedes' Principle. The relative density was calculated by calculating the percentage of the bulk density compared to that of the theoretical density. The method of calculating the theoretical density is shown in Appendix B – Theoretical Density.

$$\boldsymbol{True\ Density\ of\ sample = \frac{W_1 \rho_w}{W_1 - W_3}} \qquad \textbf{Equation 1}$$

$$\boldsymbol{Bulk\ Density = \frac{W_1 \rho_w}{W_2 - W_3}} \qquad \textbf{Equation 2}$$

$$\boldsymbol{Volume\ Fraction\ of\ Open\ Porosity = \frac{W_2 - W_1}{W_2 - W_3}} \qquad \textbf{Equation 3}$$

3.6.2. Cutting, Mounting and Polishing

After the samples were measured for densities they were then cut in half and mounted before they were polished. Once this was finished further characterisation could be carried out.

3.6.2.1. Cutting

The samples were cut using a Struers Secotom-10 precision cut-off machine, using Struers diamond cut-off wheel for hard and brittle materials. The conditions for cutting were done using a wheel speed of 3500 rpm with the sample being fed at a rate of 0.015 mm/s.

3.6.2.2. Mounting

After the samples were cut one half was mounted using a Struers CitoPress - 10 and Polyfast mounting resin. Polyfast is a thermosetting, bakelite resin with carbon filler, which is suitable for fast mounting and for examination in a SEM, and hence was chosen. The CitoPress has built-in operating conditions for this resin which were used.

3.6.2.3. Polishing

Once the samples were mounted they were ground and polished using a Leco Spectrum System 2000. This machine allowed for six samples to be polished at a time. The overall process is summarised in the Table 4 below.

Table 4: Summary of grinding and polishing procedure, using Struers grinding and polishing discs

Step	Disc	Grit Size (μm)	Time (min)	Lubricant	Suspension
1	MD-Piano	220	5	Water	No
2	MD-Piano	1200	30	Water	No
3	MD-Largo	-	20	Diamond Extender (Blue)	9 μm DP
4	MD-Dac	-	15	Diamond Extender (Blue)	3 μm DP
5	MD-Nap	-	8	Diamond Extender (Blue)	1 μm DP
6	MD-Chem	-	2	-	OPS 0.04 μm Al_2O_3

The grinding was carried out to remove damaged or deformation surface material, while introducing only limited amounts of new deformation. The grinding discs used were Struers MD-Piano #220, MD-Piano #600 and MD-Largo. The MD-Piano disc used water as a lubricant with no diamond powder suspension (DP suspension), while the MD-Largo disc

uses a 9 µm DP suspension and a diamond extender, each of which were supplied from Struers.

Like grinding, polishing must remove the damage introduced by previous operations. This is achieved with steps of successively finer abrasive particles. The polishing discs used were Struers MD-Dac, MD-Nap and MD-chem. For the discs, MD-Dac, MD-Nap, DP suspension of 3 and 1 µm were used respectively with a diamond extender, and for the MD-Chem and OPS 0.04 µm alumina solution was used with no extender.

3.6.3. Hardness and Fracture Toughness

The hardness and fracture toughness of the sintered materials were measured by the indentation technique using a Vickers indenter with a LECO V-100-A2 Vickers Hardness Tester machine. A load of 5 kg was used for each of the samples. The length of the cracks generated by the indentation was measured (Figure 9) and the crack lengths were used to calculate the fracture toughness (K_{1C}) of the materials.

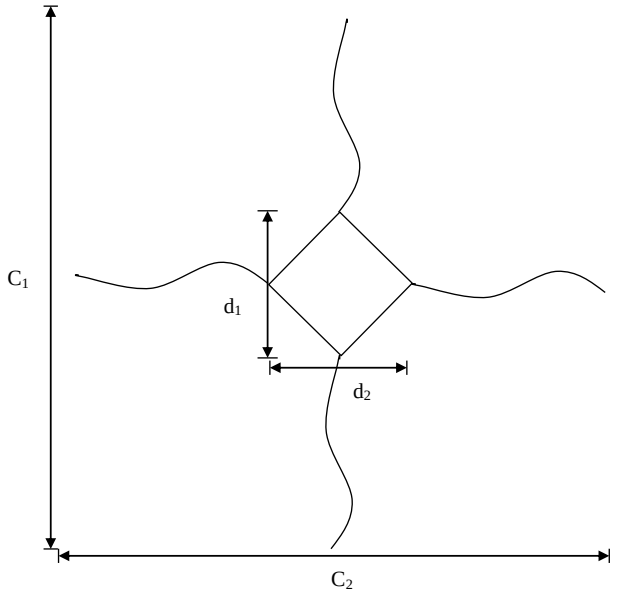

Figure 9: Schematic representations of a Vickers indent

Where, d_1 = vertical indentation length

d_2 = horizontal indentation length

c_1 = vertical length spanned by indentation cracks

c_2 = horizontal length spanned by indentation cracks

d = average indentation length

c = average length spanned by indentation cracks

The hardness values were calculated from Equation 4 [43]

$$\boldsymbol{HV = \frac{1.8544P}{d^2}} \qquad \textbf{Equation 4}$$

Where *P* is the applied load in Newton (N) and *d* is the arithmetic mean of the two diagonals in micrometers (μm). The hardness can then be converted into GPa using the relationship shown in Equation 5 [43].

$$\boldsymbol{H(GPa) = 0.009817HV} \qquad \textbf{Equation 5}$$

The fracture toughness was calculated from Equation 6 [43] , which is the half penny fracture toughness equation; this is reported to be suitable for zirconia systems [44] [45].

$$\boldsymbol{K_{IC} = \xi \sqrt{\frac{E}{H}} \times \left(\frac{L}{c_{ave}}\right)} \qquad \textbf{Equation 6}$$

Where, K_{1C} = Fracture Toughness ($MPa.m^{1/2}$)

ξ = 'calibration' constant = 0.016

E = Young's Modulus (GPa)

H = Hardness (GPa)

L = Load (N)

c_{ave} = Average crack length (m)

3.6.4. Microstructure

The microstructure was analysed using SEM. This was also done using the SEM microscopes described for the powder characterisation, a FEI Quanta 400 FEG and Philips XL30 FEG ESEM. The samples were mounted and polished to a high finish as described earlier. Each of the samples was sputter coated twice with carbon prior to the analyses to prevent charging of the samples, prior to the analysis.

3.6.5. XRD

The XRD analysis for the sintered samples was also done on a Bruker D2 phaser XRD machine. The half of the sample that was not mounted was ground on the surface using an MD-Piano 220 disc so that the surface was flat and would not interfere with the analyses. Again, all measurements were taken using a step scan of 0.020^0 recorded in the 2θ regime of $10\text{-}90^0$. The phase identification was done using X'Pert HighScore.

4. Results

4.1 *Materials based on micron-sized powders*

This section describes the powder study done on 8Y- stabilised Zirconia with TiN and TiC as the reinforcing compounds, each with a particle size in the micron sized range. This was done primarily as an introduction to each system, since these powders are significantly cheaper than nanopowders, but would also serve as a comparison to the nanopowder studies.

4.1.1. Results of Powder Characterisation and Preparation before Sintering

4.1.1.1. Results of Particle Size Measurements

The particle size distribution of each of the micron powders are shown in Figure 10, Figure 11 and Figure 12, this was measured using a Malvern Mastersizer 2000.

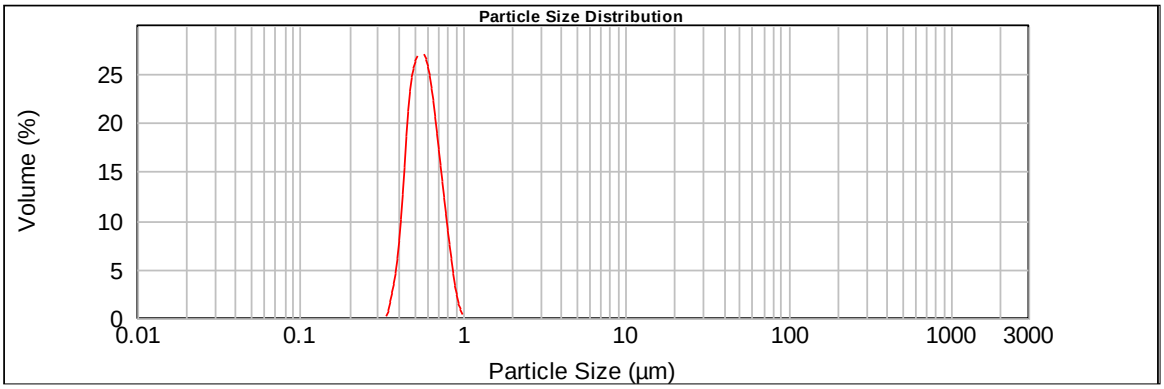

Figure 10: Particle size distribution micron-sized 8Y-ZrO_2

Figure 10, shows the particle size distribution of the micron-sized fully stabilized Zirconia which was supplied by Sigma-Aldrich. The powders were found to have a D(0.1)=0.44 µm, D(0.5)=0.57 µm, and D(0.9)=0.75 µm, which is consistent with the 700 nm particle size given by the supplier.

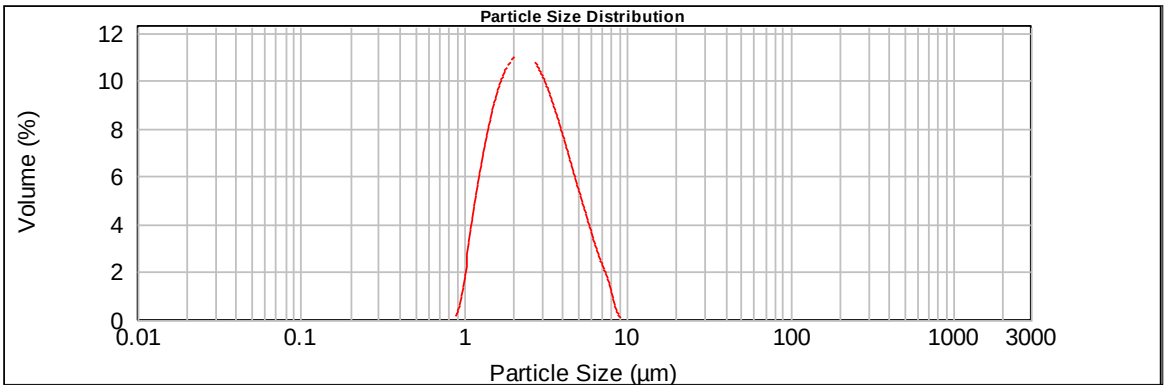

Figure 11: Particle size distribution micron-sized TiC

Figure 11, above shows the particle size distribution of the micron-sized TiC, which was supplied by Element Six. It was found to have a D(0.1)=1.37 µm, D(0.5)=2. µm, D(0.9)=5.04 µm.

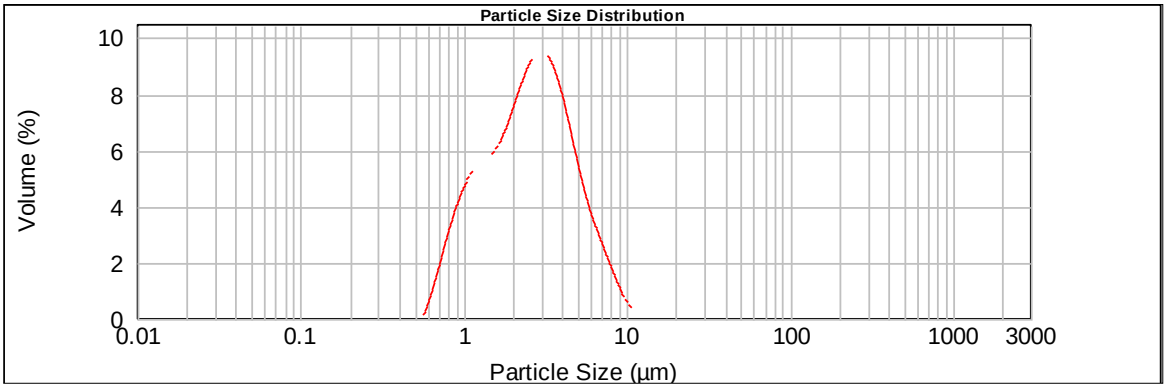

Figure 12: Particle size distribution micron-sized TiN

The above figure, Figure 12, shows the particle size distribution of the micron-sized TiN, which was also supplied by Element Six. It was found to have a D(0.1)=0.73 µm, D(0.5)=2.58 µm, and a D(0.9)=5.02 µm.

The particle size of the micron sized 8Y-Zirconia was in accordance with the supplier, however, there were no data given by Element Six Ltd for the micron sized TiC and TiN and hence no comparison could be made.

4.1.1.2. Results of BET Measurement

The results for BET were obtained from the School of Chemistry at the University of the Witwatersrand; this was carried out on a Quantachrome Autosorb-1. The results from the

BET measurements are summarised in Table 5 below. The specific area results for the micron powders were as expected, with the TiC and TiN having similar specific area result to each other since they have very similar particle sizes, D(0.5)=2.50 μm and D(0.5)=2.58 μm for TiC and TiN respectively. The particle size of the 8Y-Zirconia is much smaller than that of the reinforcing powders and so a higher surface area was expected.

Table 5: BET results for micron-sized powders

Sample	**Surface Area (m^2/g)**
ZrO_2	5.5
TiC	1.9
TiN	1.9

4.1.1.3. Results of Rheology Studies

This section shows the rheology studies carried out on each of the individual micron-sized powders, followed by 50 volume percent mixtures of Zirconia-TiC and Zirconia-TiN. These were all measured using an Anton Paar Physica MCR300 rheometer with Lubrizol 2155 as the dispersant and hexane as the solvent. A solids loading of 30% was used for the individual Zirconia system and a solids loading of 50% was used for the TiN and TiC systems. For the composite studies a 40% solids loading was used. The weight percentage Lubrizol was calculated in comparison to the mass of powder required to achieve the stated solids loading.

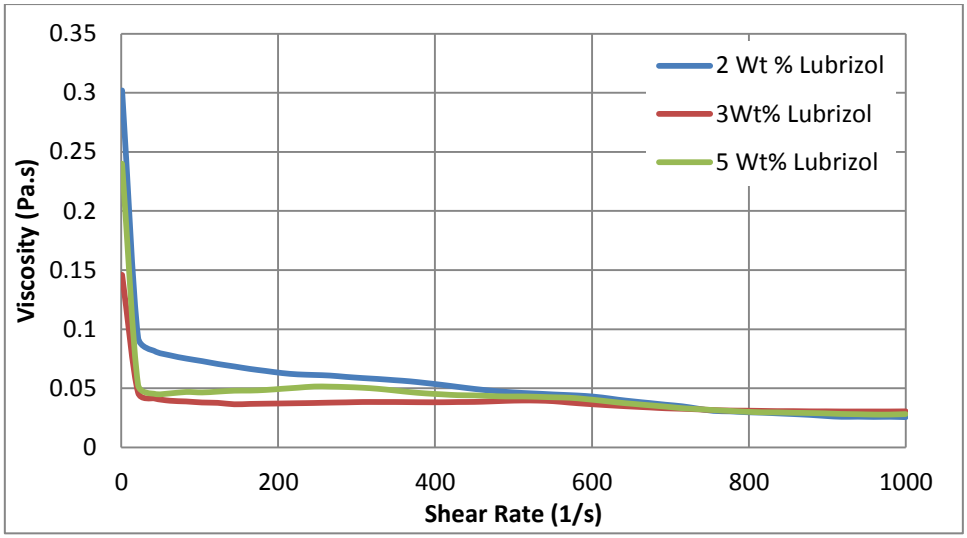

Figure 13: Relationship between viscosity and shear rate for the micron-sized Zirconia-8Y for various concentrations of Lubrizol 2155

Figure 13 shows the rheology study carried out on the micron-sized fully stabilized Zirconia, 8Y-ZrO_2. As can be seen, the viscosity changed with shear rate at different weight percentages of Lubrizol. It can be seen that the lowest viscosity at varying shear rates was achieved using a Lubrizol content of 3 weight percent. Using this data and data obtained from the studies on the micron-sized TiC and TiN the following figure was generated.

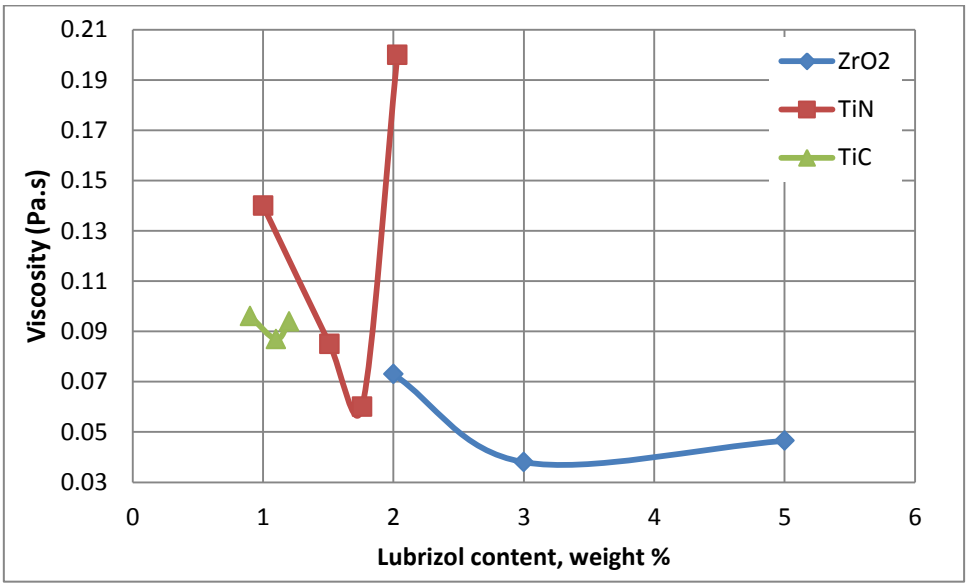

Figure 14: Relationship between viscosity and the amount of Lubrizol 2155 added at a shear rate of 100/s for the each of the micron-sized powders

Figure 14 shows the viscosity of each of the micron sized powders at a shear rate of 100/s at different weight percentages of Lubrizol. From the figure it can be seen that the optimal

amount of Lubrizol is 3, 1.1 and 1.8 weight percent Lubrizol for the micron-sized ZrO_2, TiC and TiN respectively.

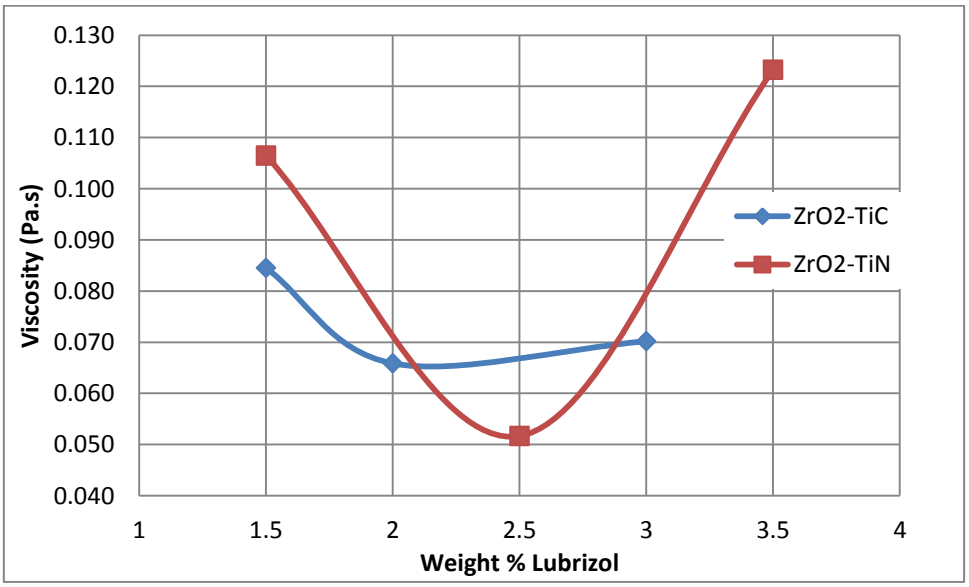

Figure 15: Relationship between viscosity and the amount of Lubrizol 2155 added at a shear rate of 100/s for the 50 vol% TiC-8Y-ZrO_2 system and 50 vol% TiN-8Y-ZrO_2

Figure 15 shows the relationship between viscosity and the amount of Lubrizol 2155 added at a shear rate of 100/s for the 50 vol% TiC-8Y-ZrO_2 system and 50 vol% TiN-8Y-ZrO_2. A 50% solids loading was tested. It can be seen that the optimum amount of Lubrizol for the ZrO_2-TiC and ZrO_2-TiN micron-sized systems is 2 and 2.5 wt. % respectively.

Combing the BET and rheology results the following table was generated, which shows the mass of Lubrizol per unit area of each specific powder at the optimal Lubrizol contents.

Table 6: Summary of powder characterisation and rheology results for micron powders

Sample	**Particle Size (nm)**	**Surface Area (m^2/g)**	**Optimal Lubrizol Content (wt. %)**	**Solid loading (Volume %)**	**Mass Lubrizol per unit area powder (mg/m^2)**	**Viscosity (@100, Pa.s)**
8Y-ZrO_2	570	5.5	3	30	5.45	0.038
TiC	2500	1.9	1.1	50	5.79	0.087
TiN	2580	1.9	1.7	50	8.95	0.066

4.1.2. Sintering Results of Micron-sized Composites

This section shows the results obtained from sintering micron powder mixtures of 50% TiC and TiN by volume with Zirconia. The results reported are the: density, microstructure and mechanical properties. The powders were mixed using a ball mill, for 4 hours at 300 rpm in a tungsten carbide milling pot, with the optimum amount of Lubrizol found in the rheology study for each system. The powders were then dried using a rotary evaporator before the Lubrizol was burnt off using a tube furnace at 500°C for 1 hour. The powder mixtures were then sintered at different temperatures, for 5 minutes with a ramp rate of 250°C/min with a pressure of 30 MPa.

4.1.2.1. Density Results

The densities of the sintered samples were calculated using the Archimedes principle. The density results for each system and sintering conditions are summarised in Table 7.

.

Table 7: Density results of micron-sized powder system

Sample	**Temperature (°C)**	**Pressure (MPa)**	**Bulk Density (g/cm^3)**	**Theoretical Density (g/cm^3)**	**Relative Density (%)**
ZrO_2-50% TiC	1500	30	5.528	5.490	100
ZrO_2- 50% TiN	1500	30	5.545	5.725	96.9
ZrO_2-50% TiN	1400	30	5.385	5.725	94.7

4.1.2.2. Microstructure of sintered samples

This section shows the SEM micrographs of the sintered samples; this was performed to ensure that the densities measured were correct, and the extent of dispersion and mixing were analysed, and to finally ensure that there was no residual carbon after the Lubrizol burn off.

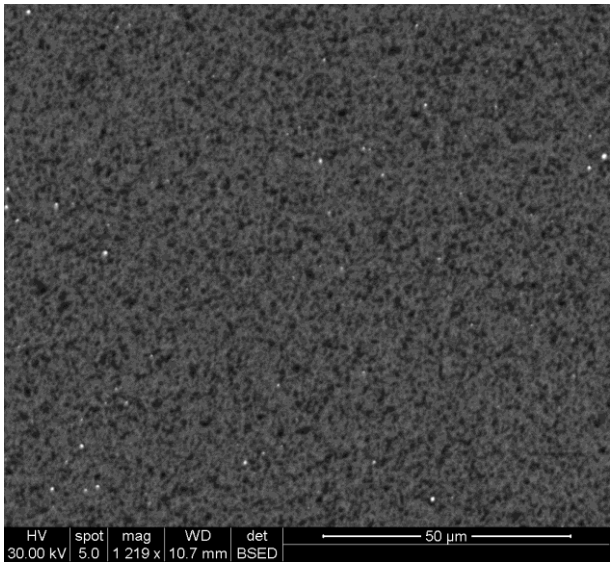

Figure 16: SEM micrograph of 8Y-ZrO_2-50%TiC sintered at 1500°C

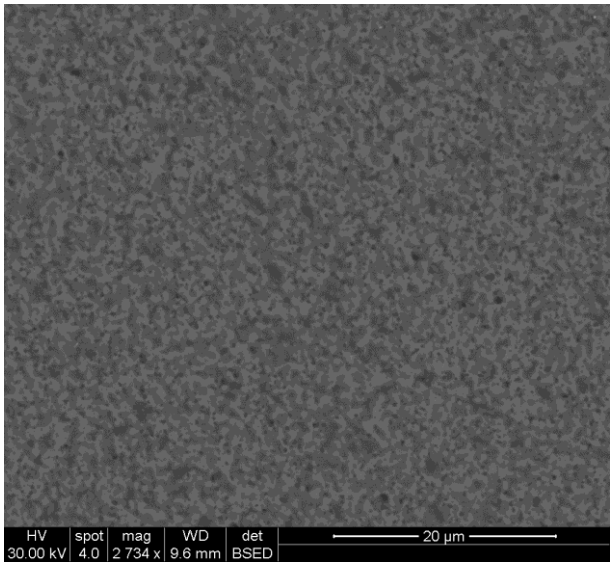

Figure 17: SEM micrograph of 8Y-ZrO_2-50%TiN sintered at 1400°C

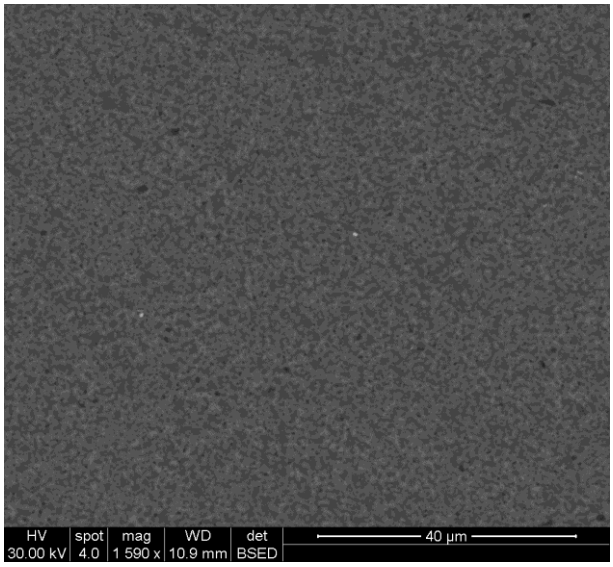

Figure 18: SEM micrograph of 8Y-ZrO_2-50%TiN sintered at 1400°C

Each of the figures above show very well dispersed systems, with no large agglomerate of the reinforcing or matrix powders. The white particles in Figures 16 and 18 are tungsten carbide which were added to the sample during milling. This was done in a tungsten carbide milling pot. The lower densities of the TiN system can be attributed to porosity which was shown as black spots in Figures 17 and 18.

4.1.2.3. Hardness and Fracture Toughness

The hardness was tested using the Vickers micro-hardness tester with a load of 5 kg. The fracture toughness was then calculated using the Half-Penny Crack method [(43)] .

Table 8 summarises the mechanical properties obtained for the micron sized systems.

Table 8: Hardness and fracture toughness results for micron based materials

Material	**Temperature (°C)**	**Relative Density (%)**	**Hv (GPa)**	**KiC (Mpa.m$^{1/2}$)**
ZrO_2-TiC	1500	100	10.1 ± 0.4	3.43 ± 0.5
ZrO_2-TiN	1500	96.9	9.8 ± 0.3	3.49 ± 0.3
ZrO_2-TiN	1400	94.1	10.6 ± 0.4	3.07 ± 0.3

4.2 *Materials based in nanosized powders*

This section shows the results obtained from the powder characterisation and preparation, as well as the results from the sintering of the nanopowders. The powders that were used for this study are shown in the table below, with properties given by the manufacturers.

Table 9: Characterisation data from suppliers of the nanosized powders used

Material	**Mean Particle Size**	**Specific Surface Area (m^2/g)**	**Purity (%)**	**Density (g/cm^3)**	**Supplier**
8Y-ZrO_2 (nano)	28 nm	16±3	-	5.90	Tosoh
TiC (nano)	20 nm	-	99+	4,930	Abcr
TiN (nano)	40 nm	40-55	97+	5,220	Abcr

4.2.1. Results of Powders Characterisation and Preparation before Sintering

4.2.1.1. BET

The results for BET were obtained from the School of Chemistry; these measurements were carried out on a Quantachrome Autosorb-1. The results from the BET measurements are summarised in Table 10. These show similar surface areas to that given by the suppliers for 8Y-ZrO_2 and TiN. No data on the surface area of the TiC was given by the suppliers and therefore no comparison could be made in this case.

The specific area results from the BET measurements showed that the TiN powder had the highest surface area which was consistent with the fact that this powder had the smallest average particle size. The SSA value measured, of 61.26 m^2/g is close to the range given by the manufacturer of 40-55 m^2/g. The nanosized 8Y-Zirconia had a SSA of 15.3 m^2/g, in the range given by the manufacturer of 16±3 m^2/g. This was lower than that of the TiC, 23.1 m^2/g, even though the 8Y-Zirconia powder had a smaller particle size.

Table 10: BET results for nanopowders

Sample	Surface Area from suppliers (m^2/g),	Measured Surface Area (m^2/g)
8Y-ZrO_2	16±3	15.3
TiC	-	23.7
TiN	40-55	61.3

4.2.1.2. Phase composition

The phase composition of the nanosized powder was determined using X-ray diffraction (XRD). This was done using a Bruker D2 phaser XRD machine.

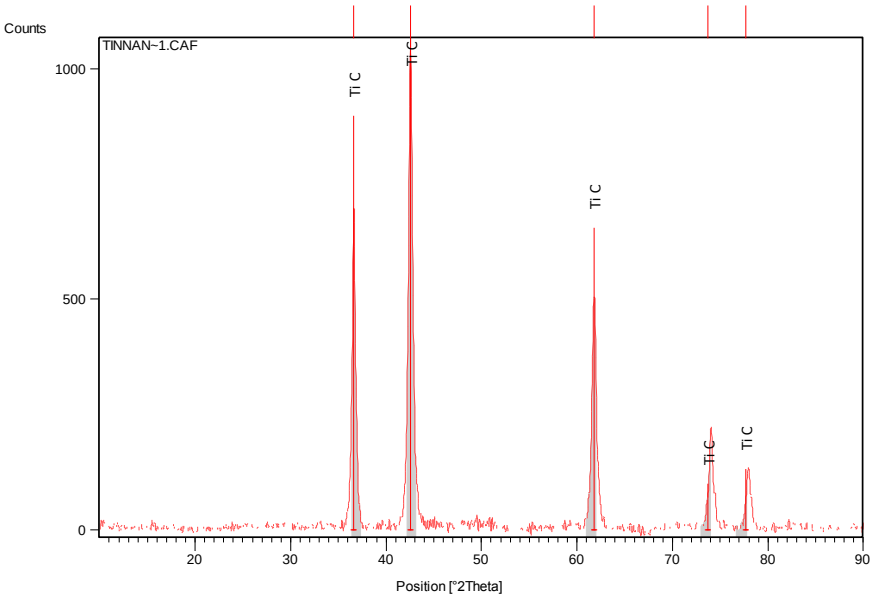

Figure 19: XRD pattern for the nano TiC powder

Figure 19 shows XRD pattern for the nano TiC powder, as received from the supplier. It can be seen that there were no crystalline impurities in the powder.

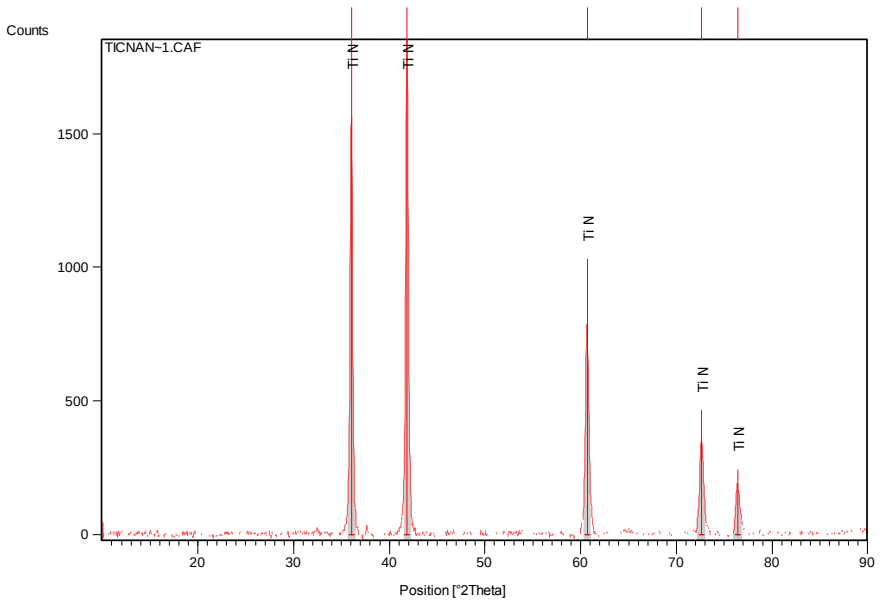

Figure 20: XRD pattern for the nano TiN powder

The XRD pattern for the TiN nanopowder, as received from the supplier, can be seen in Figure 20. The peaks were identified as TiN. As with the TiC powder, there were no crystalline impurities in the powder.

4.2.1.3. Rheology

This section shows the rheology studies carried out on each of the individual nano-sized powders, followed by 50 and 10 volume percentage mixtures of the Zirconia-TiC and Zirconia-TiN. Again, as with the coarse studies, all measurements were done using an Anton Paar Physica MCR300 rheometer with Lubrizol 2155 as the dispersant and hexane as the solvent, but with varying solids loading percentages. Again, the weight percentages of Lubrizol were calculated with reference to the mass of powder required to achieve the stated solids loading.

For the pure nanopowders a solids loading of 30, 15 and 3.2% was used for the ZrO_2, TiC and TiN respectively. A 30 volume% solid loading was chosen for the nanosized ZrO_2 as this was the loading used for the micron sized ZrO_2. This was done although the nanosized ZrO_2 had a larger surface area than the micron sized. It was possible to disperse the nanosized ZrO_2 at that solids loading level.

For the nanosized TiC and TiN a solids loading of 50%, as was used in the case of the micron powder, could not be dispersed. In fact, even significantly lower solids loadings could not be dispersed. Hence a test suspension was made for each of the powders to find a suitable solids loading. This was done gradually adding hexane to a fixed mass of powder, the amount being monitored, until the powder no longer absorbed the hexane and the mixture began to behave as a liquid. Based on the amount of hexane that was used to achieved this and the mass of powder involved in this test, a suitable solids loading for TiC and TiN could be calculated. This was found to be 15 and 3.2% for the TiC and TiN respectively.

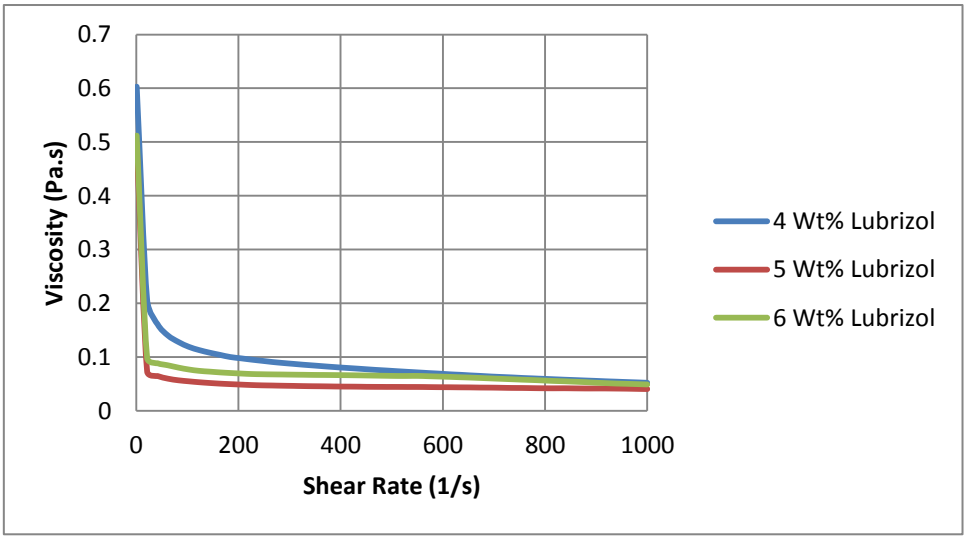

Figure 21: Relationship between viscosity and shear rate for the nano 8Y-Zirconia for various concentrations of Lubrizol 2155, at 30 volume % solids loading

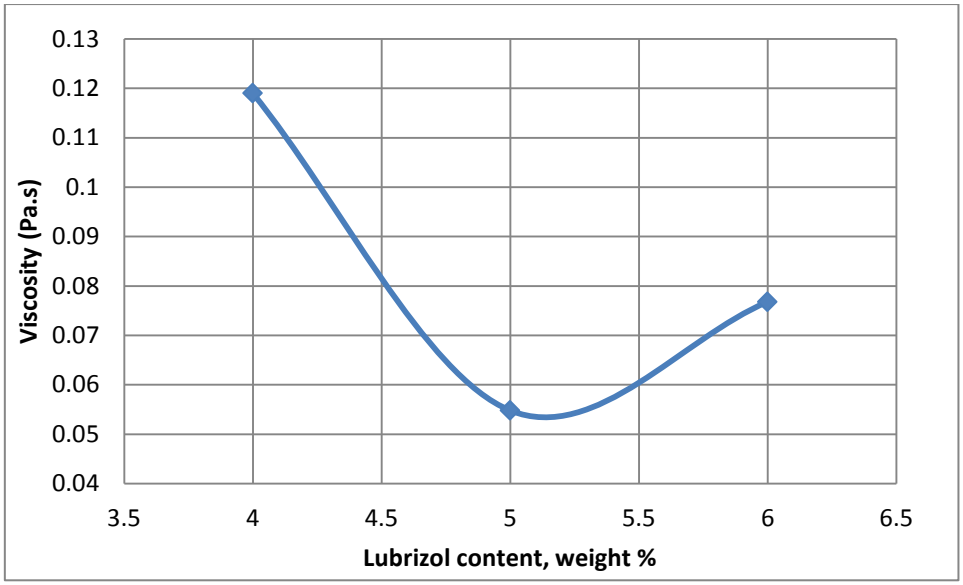

Figure 22: Relationship between viscosity and the amount of Lubrizol 2155 added at a shear rate of 100/s for the nano 8Y-Zirconia, at 30 volume % solids loading

Figures 21 and 22 show the rheology studies carried out on the nanosized fully stabilized Zirconia, 8Y-ZrO_2. From these figures it was shown that the optimum amount of Lubrizol to disperse the coarse Zirconia was 5 weight percent.

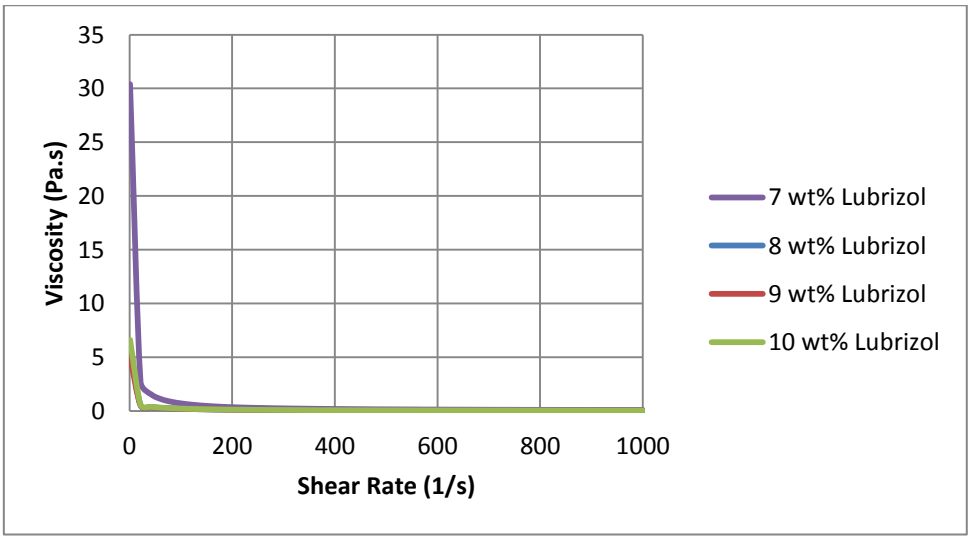

Figure 23: Relationship between viscosity and shear rate for the nano TiC for various concentrations of Lubrizol 2155, at 15 volume % solids loading

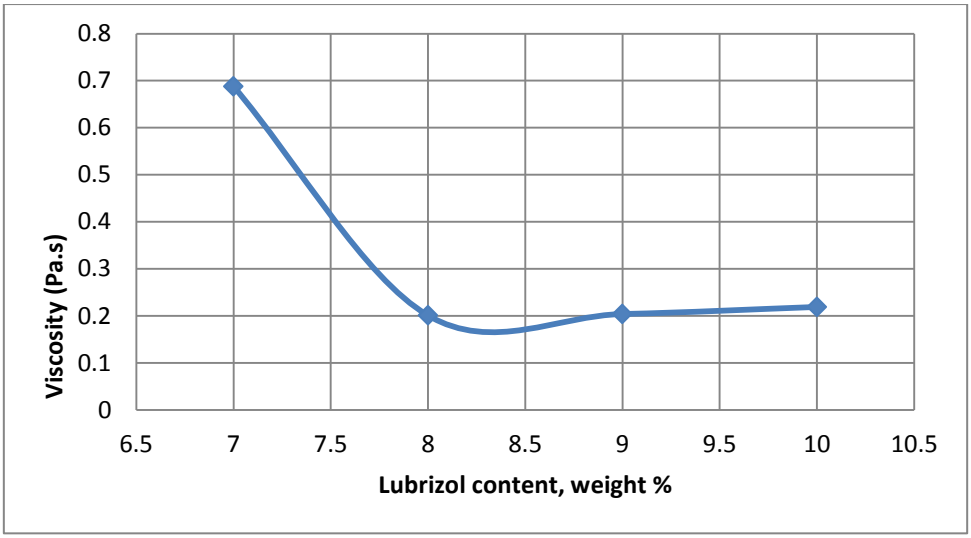

Figure 24: Relationship between viscosity and the amount of Lubrizol 2155 added at a shear rate of 100/s for the nano TiC, at 15 volume % solids loading

Figures 23 and 24 show that the optimal amount of Lubrizol 2155 needed to generate a stable suspension for the nano TiC was 8 weight percent.

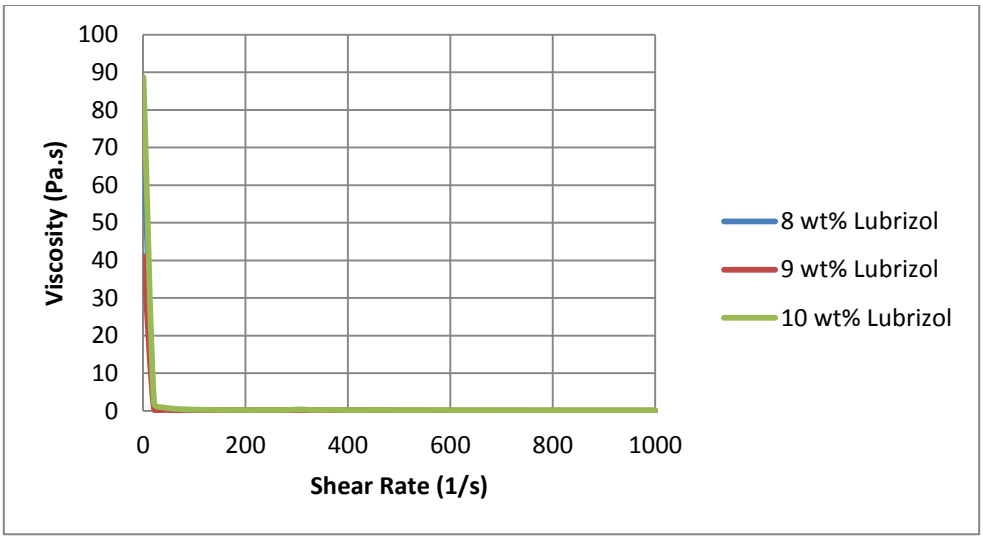

Figure 25: Relationship between viscosity and shear rate for the nano TiN for various concentrations of Lubrizol 2155, at 3.2 volume % solids loading

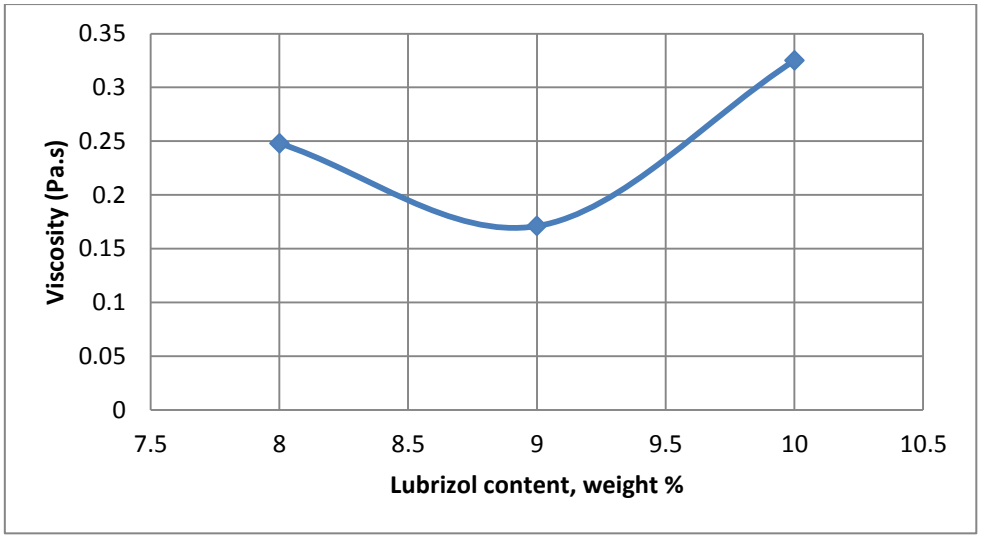

Figure 26: Relationship between viscosity and the amount of Lubrizol 2155 added at a shear rate of 100/s for the nano TiN, at 3.2 volume % solids loading

Figures 25 and 26 show that the optimal amount of Lubrizol to disperse the TiN was 9 weight percent.

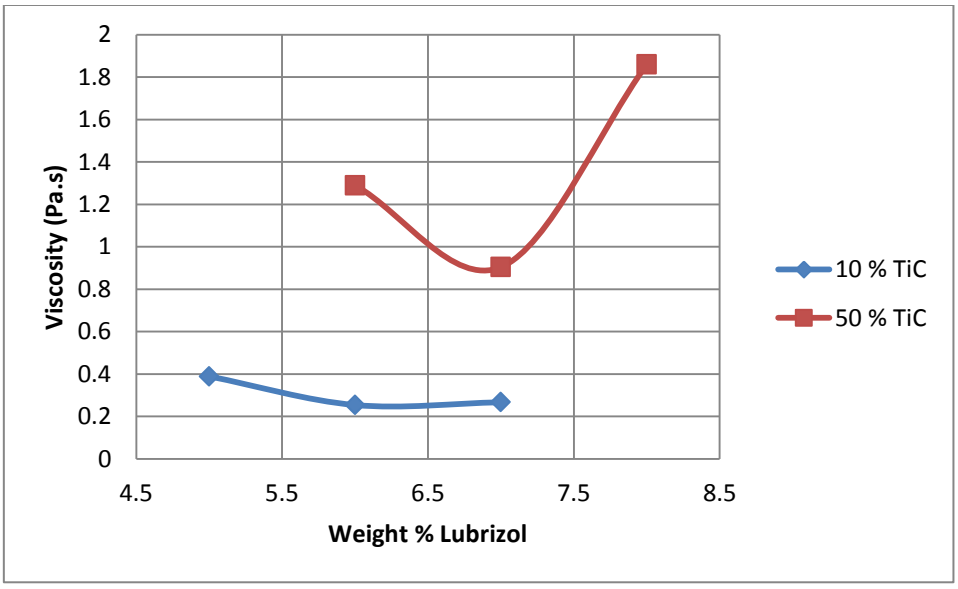

Figure 27: Relationship between viscosity and the amount of Lubrizol 2155 added at a shear rate of 100/s for the mixtures of nano 8Y-Zirconia and TiC for 10 and 50% by volume of TiC

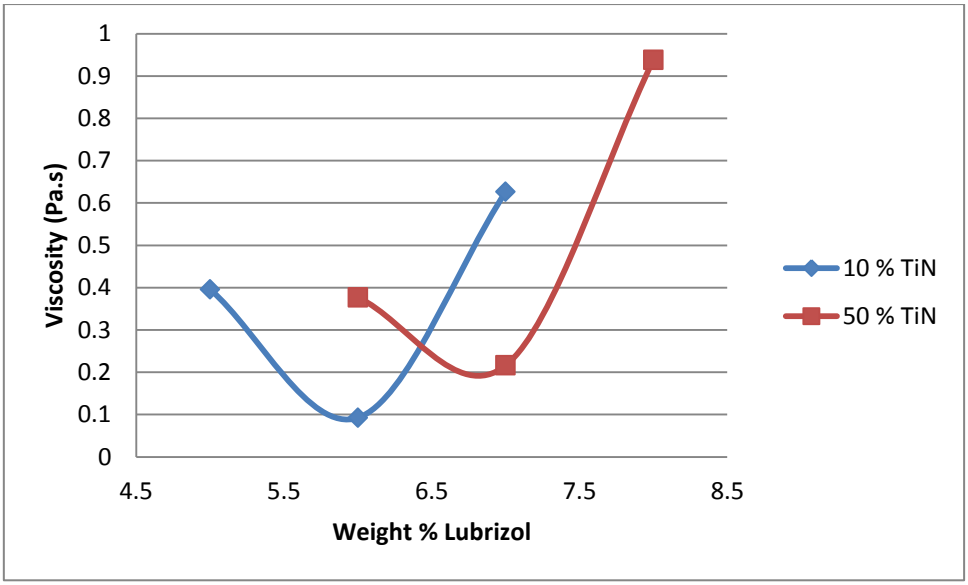

Figure 28: Relationship between viscosity and the amount of Lubrizol 2155 added at a shear rate of 100/s for the mixtures of nano 8Y-Zirconia and TiN for 10 and 50% by volume of TiN

Figures 27 and 28 show the optimal Lubrizol content for the composite mixtures ZrO_2-TiN for 10 and 50 volume % of TiN. For the TiC, the optimal amount of Lubrizol was found to be 6.2 and 6.5% for the 10 and 50 volume % TiC content respectively. For the TiN, the optimal amount was 5.9 and 6.8% for the 10 vol% and 50 vol% TiN contents respectively.

The rheology results for the composite mixtures are summarised in the Table 11.

Table 11: Summary of rheology results for nano composites mixtures

Material		**Composition (Vol. %)**	**Solid loading (Vol. %)**	**Optimal Amount of Dispersant (Wt. %)**
ZrO_2	TiC	10	28.5	6.2
		50	22.5	6.9
	TiN	10	27.3	5.9
		50	5	6.8

4.2.1.4. Results of particle size measurements

The characterisation of the nanopowders began with SEM. SEM images were taken of the powders, as received from the supplier, to aid in the determination of the particle sizes. The particle size characterisation was done after the rheology studies; this is because of the

agglomeration tendencies that are present in nanopowders, and hence particle size analysis could only be done once an adequate method of dispersion could be found.

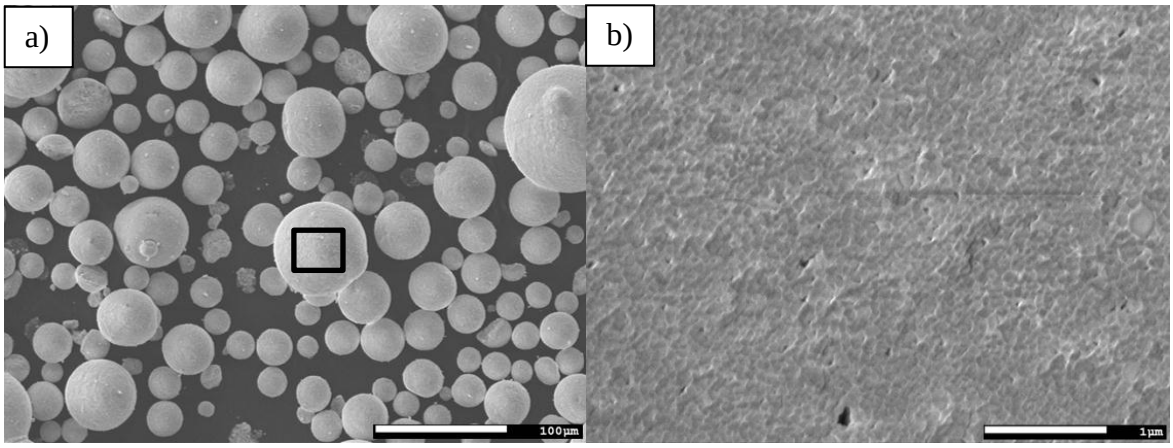

Figure 29: SEM image of nano fully stabilized Zirconia a) lower magnification showing granular form b) high magnification on granular particle

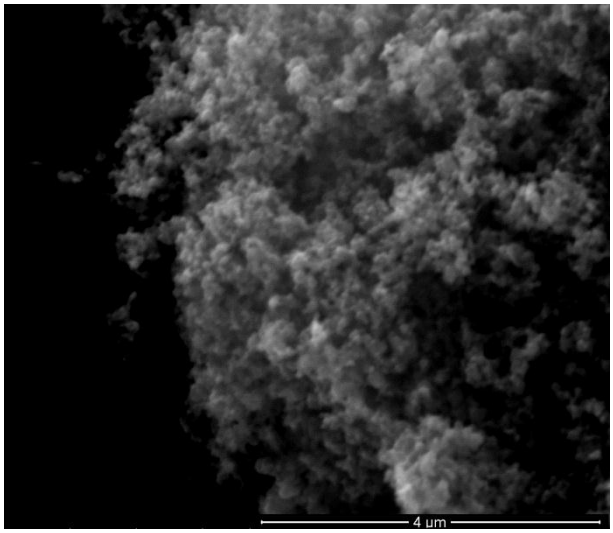

Figure 30: SEM image of nano TiC

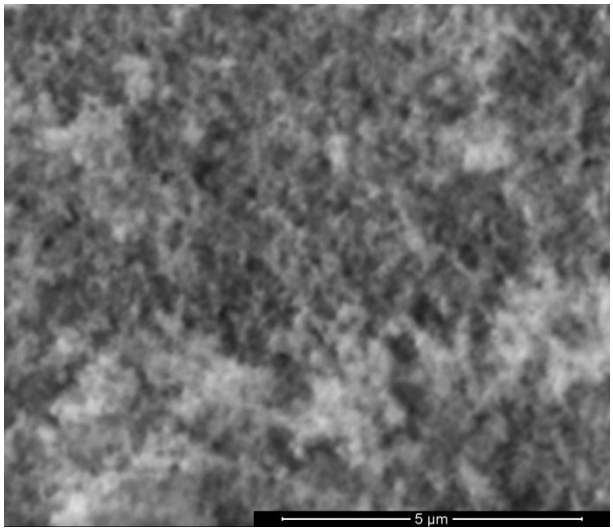

Figure 31: SEM image of nano TiN

The results from the SEM of the nanopowders show that the ZrO_2 was in granular form for easy handling. This was stated by the manufacturer [46] and is shown in Figure 29a. Upon further magnification of a single granule, shown by the marked area in Figure 29a, it can be seen that the granule did in fact contain particles in the nano range. This is shown in Figure 29b. Both the TiC and TiN could be seen to be highly agglomerated, from Figures 30 and 31; however, it can be seen that the size range for both powders was in the nano range.

The particle size measurements were conducted on a Malvern Zetasizer Nano. Prior to the particle size measurements a 30% solids loading of the 8Y-Zirconia was milled in 150 ml of hexane with 5 weight percent Lubrizol 2155 with respect to the powder, those being the optimal dispersion conditions found in the rheology studies. The powders were milled and tested for particle size intensity every 30 minutes until they were fully dispersed. It was found that after 3 hours the fully stabilised Zirconia powder was fully dispersed.

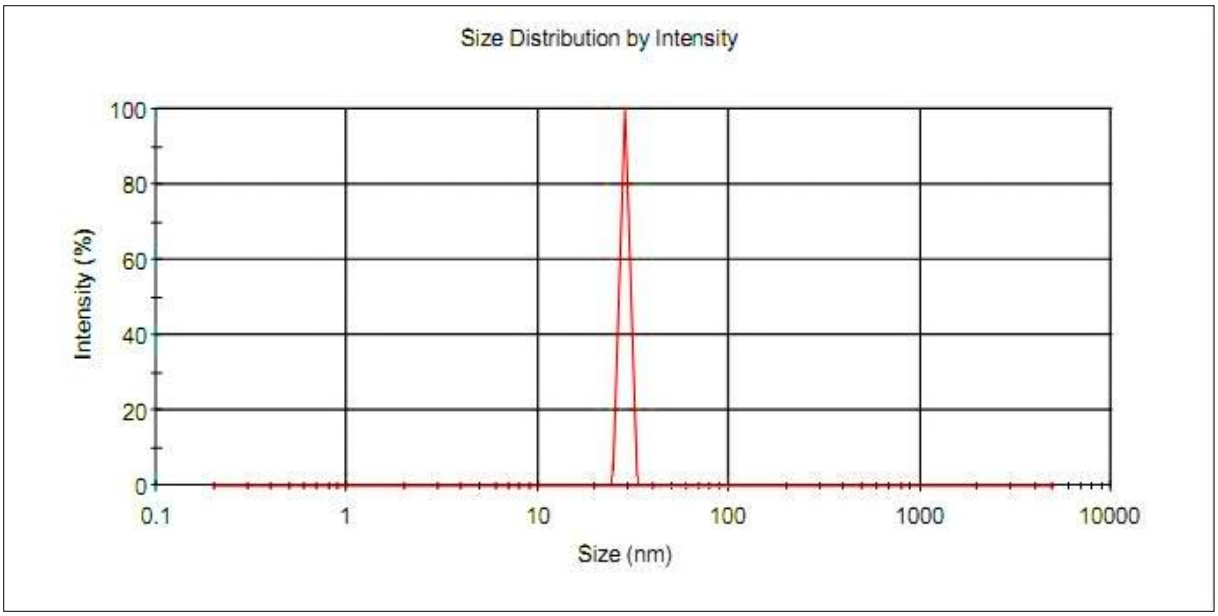

Figure 32: Size distribution intensity of nano 8Y-ZrO_2 powder after 3 hours milling with Lubrizol 2155 and hexane

Figure 32 shows the particle size distribution by intensity of the nano fully stabilized Zirconia from Tosho after 3 hours of milling in hexane with Lubrizol; the figure shows a peak intensity of 28.6 nm. The results were consistent with the average particle size given by the manufacturers who claimed the powder to have an average particle size of 28 nm.

The nano TiC powder was dispersed in a similar way to the Zirconia. This was done, however, using a 15% solids loading, again in 150 ml of hexane with 8.3 weight percent of Lubrizol 2155 with respect to the amount of powder. As with the 8Y-Zirconia, the powder was milled and tested for particle size intensity every 30 minutes until fully dispersed. It was found that after 3 hours the TiC powder was fully dispersed. For the nano TiN a similar process was followed, using a 3.2% solids loading with a 9 weight percent of Lubrizol used. This powder was found to be dispersed after 4 hours.

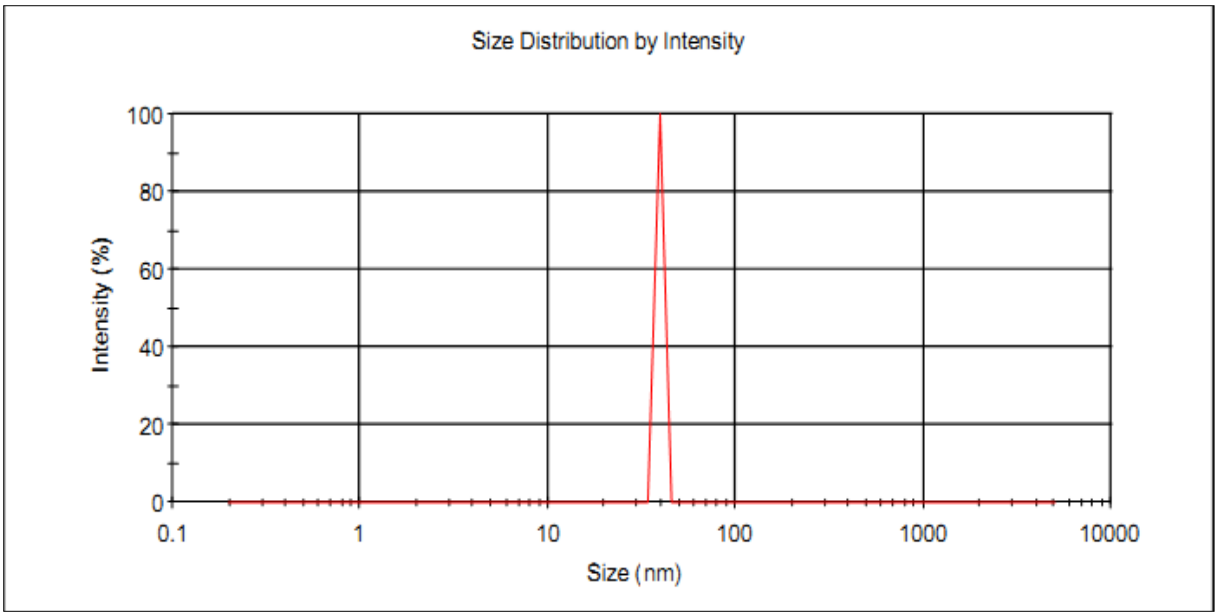

Figure 33: Size distribution of nano TiC powder after 3 hours milling with Lubrizol 2155 and hexane

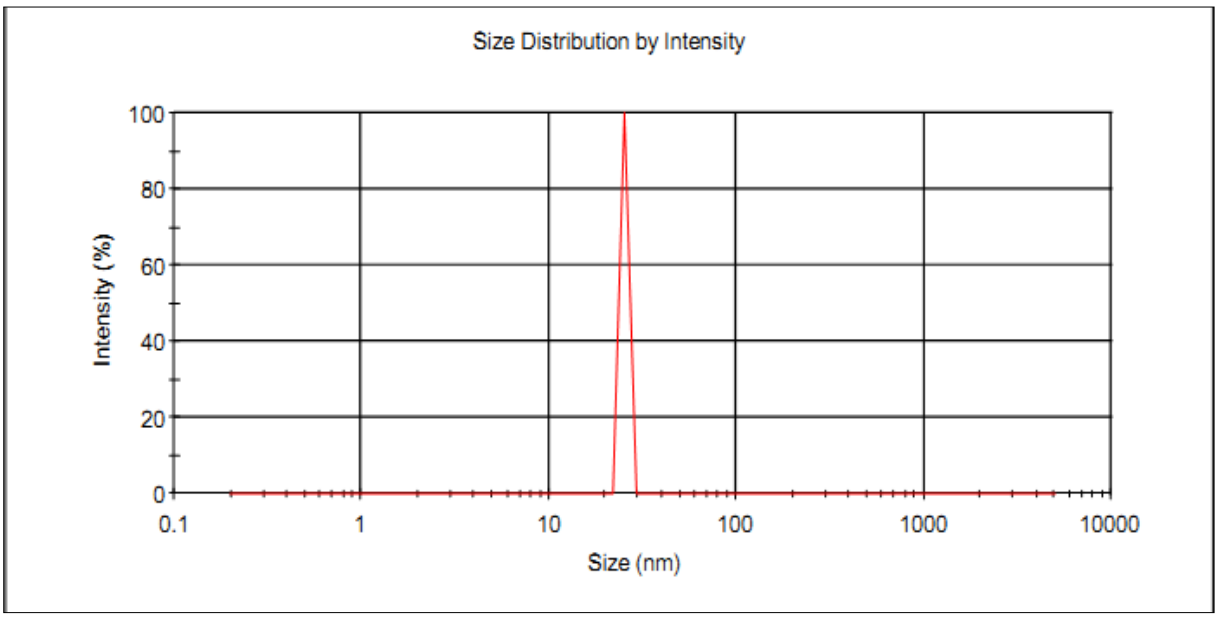

Figure 34: Size distribution of nano TiN powder after 4 hours milling with Lubrizol 2155 and hexane

Figures 33 and 34 show the particle size distribution by intensity of the nano TiC and TiN respectively which were purchased from Abcr. The figures showed a particle size of 39.4 and 25.4 nm for TiC and TiN respectively. Each powder was said, by the manufacturers, to have a particle size of 40 nm and 20 nm respectively which was consistent with the particle size

measured. The powders were milled for 3 and 4 hours respectively, with Lubrizol before measurements were carried out.

The particle sizes for the nanopowders were found to be in accordance with the size given by the manufacturer. The amount of time to mill each of the powders were found to be 3 hours for the ZrO_2 and TiC and 4 hours for the TiN. This was due to the extent of agglomeration which was greater in finer powders [47], with the TiN having the finest particle size of 25.4 nm compared to 28.6 and 39.4 nm for the ZrO_2 and TiC respectively.

4.2.1.5. Oxygen Content

Because of the size of the nanopowders, hence the surface area of the particles, the TiC and TiN could be easily oxidised and contain some oxygen contamination. Hence these powders were tested for oxygen content using Leco. The results from the Leco test are summarised in Table 12.

Table 12: Oxygen content of the nanosized TiC and TiN powders

Powder	**Oxygen Content (wt. %)**
TiC	3.54
TiN	8.44

It was assumed that the oxygen present would be in the form of TiO_2, rutile, which is the most stable form of titanium in oxygen [48]. Using the oxygen content the mass of TiC/TiN and TiO_2 was calculated, as shown in Appendix C – Equations for Oxygen Content, and new theoretical densities were calculated which is shown in in Tables 13 and 14 for TiC and TiN respectively.

Table 13: Recalculated theoretical densities for TiC systems

Sample Name.	**Theoretical Density excluding oxide content (g/cm^3)**	**Theoretical Density including oxide content (g/cm^3)**
3 vol% TiC	5.851	5.832
10 vol% TiC	5.784	5.723
30 vol% TiC	5.594	5.421
50 vol% TiC	5.405	5.357

Table 14: Recalculated theoretical densities for TiN systems

Sample Name.	Theoretical Density excluding oxide content (g/cm^3)	Theoretical Density including oxide content (g/cm^3)
3 vol% TiN	5.865	5.853
10 vol% TiN	5.831	5.792
30 vol% TiN	5.735	5.622
50 vol% TiN	5.640	5.457

4.2.2. Sintering Results of Nanocomposites

The sintering results from the nanopowders ZrO_2 composites are shown in this section. These comprise of the density, microstructure and mechanical properties. Each composition was milled with the optimal Lubrizol content, found in the rheology study, for 3 hours, and then dried in a rotary evaporator. After this the Lubrizol was burnt off in argon atmosphere containing 5% hydrogen, in a tube furnace for an hour at 500°C. The powders were then stored in a vacuum desiccator to prevent any oxidation of the reinforcing powders, prior to sintering.

4.2.2.1. Density Results

The powder mixtures were sintered at different temperatures, for 5 minutes with a ramp rate of 250°C/min, at pressures of 30 MPa and 50 MPa. Tables 15 and 16 shows a summary on the sintering results of the composites, the first being the ZrO_2-TiC composite system and the latter the ZrO_2-TiN composite system. The relative sample densities were compared for the cases when the theoretical density excluded or included oxygen contamination. The sample names are given in the following manner: composition, sintering temperature (°C) and sintering pressure (MPa). Each sample was sintered for 5 minutes.

Much better densities were reported when using a theoretical density including the oxygen content. Furthermore the densities calculated when taking the oxygen content into account relate much better with the microstructure of the sintered samples, hence all further theoretical densities included the oxygen content.

Table 15: Densities for nanocomposites ZrO_2-TiC composite materials

Sample Name.	Theoretical Density (g/cm^3)	Bulk Density (g/cm^3)	Relative Density (%)	Theoretical Density including oxide content (g/cm^3)	Relative Density with oxide content (%)
3 vol% TiC-ZrO_2, 1500°C, 30 MPa	5.851	5.830	99.6	5.832	99.97
3 vol% TiC-ZrO_2, 1600°C, 30 MPa	5.851	5.835	99.7	5.832	100.06
3 vol% TiC-ZrO_2, 1500°C, 50 MPa	5.851	5.837	99.8	5.832	100.09
3 vol% TiC-ZrO_2, 1600°C, 50 MPa	5.851	5.849	100	5.832	100.30
10 vol% TiC-ZrO_2, 1500°C, 30 MPa	5.784	5.684	98.3	5.723	99.31
10 vol% TiC-ZrO_2, 1600°C, 30 MPa	5.784	5.698	98.5	5.723	99.56
10 vol% TiC-ZrO_2, 1500°C, 50 MPa	5.784	5.706	98.7	5.723	99.70
10 vol% TiC-ZrO_2, 1600°C, 50 MPa	5.784	5.722	98.9	5.723	99.98
30 vol% TiC-ZrO_2, 1500°C, 30 MPa	5.594	5.375	96.1	5.421	99.15
30 vol% TiC-ZrO_2, 1500°C, 50 MPa	5.594	5.389	96.3	5.421	99.40
30 vol% TiC-ZrO_2, 1600°C, 50 MPa	5.594	5.406	96.6	5.421	99.72
30 vol% TiC-ZrO_2, 1700°C, 50 MPa	5.594	5.418	96.9	5.421	99.94
50 vol% TiC-ZrO_2, 1500°C, 30 MPa	5.405	4.872	90.1	5.357	90.95
50 vol% TiC-ZrO_2, 1600°C, 30 MPa	5.405	5.085	94.1	5.357	94.93
50 vol% TiC-ZrO_2, 1500°C, 50 MPa	5.405	5.079	94.0	5.357	94.81
50 vol% TiC-ZrO_2, 1600°C, 50 MPa	5.405	5.186	96.0	5.357	96.82
50 vol% TiC-ZrO_2, 1700°C, 50 MPa	5.405	5.207	96.3	5.357	97.21
50 vol% TiC-ZrO_2, 1800°C, 65 MPa	5.405	5.255	97.2	5.357	98.10

Table 16: Densities for nanocomposites ZrO_2-TiN composite materials

Sample Name.	Theoretical Density (g/cm^3)	Bulk Density (g/cm^3)	Relative Density (%)	Theoretical Density including oxide content (g/cm^3)	Relative Density with oxide content (%)
3 vol% TiN-ZrO_2, 1500°C, 30 MPa	5.865	5.824	99.3	5.853	99.51
3 vol% TiN-ZrO_2, 1600°C, 30 MPa	5.865	5.832	99.5	5.853	99.65
3 vol% TiN-ZrO_2, 1500°C, 50 MPa	5.865	5.841	99.6	5.853	99.80
3 vol% TiN-ZrO_2, 1600°C, 50 MPa	5.865	5.852	99.9	5.853	99.98
10 vol% TiN-ZrO_2, 1500°C, 30 MPa	5.831	5.710	97.9	5.792	98.58
10 vol% TiN-ZrO_2, 1500°C, 50 MPa	5.831	5.731	98.5	5.792	98.94
10 vol% TiN-ZrO_2, 1600°C, 50 MPa	5.831	5.745	99.0	5.792	99.18
10 vol% TiN-ZrO_2, 1700°C, 50 MPa	5.831	5.773	98.3	5.792	99.67
30 vol% TiN-ZrO_2, 1600°C, 50 MPa	5.735	5.570	97.1	5.622	99.06
30 vol% TiN-ZrO_2, 1700°C, 50 MPa	5.735	5.594	98.0	5.622	99.49
50 vol% TiN-ZrO_2, 1600°C, 50 MPa	5.640	5.313	94.2	5.457	97.36
50 vol% TiN-ZrO_2, 1700°C, 50 MPa	5.640	5.338	94.7	5.457	97.83

4.2.2.2. Microstructure Results of the Nanocomposites

Zirconia - Titanium Carbide

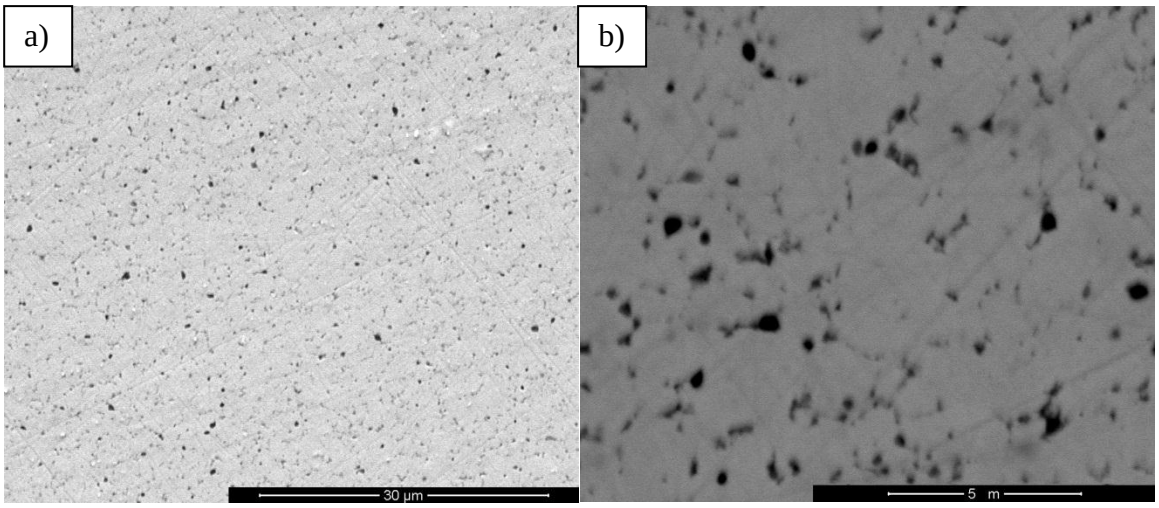

Figure 35: Micrographs of 3%TiC-ZrO_2 sintered at 1500°C 50 MPa at different magnifications and different detectors a) SE b) BS

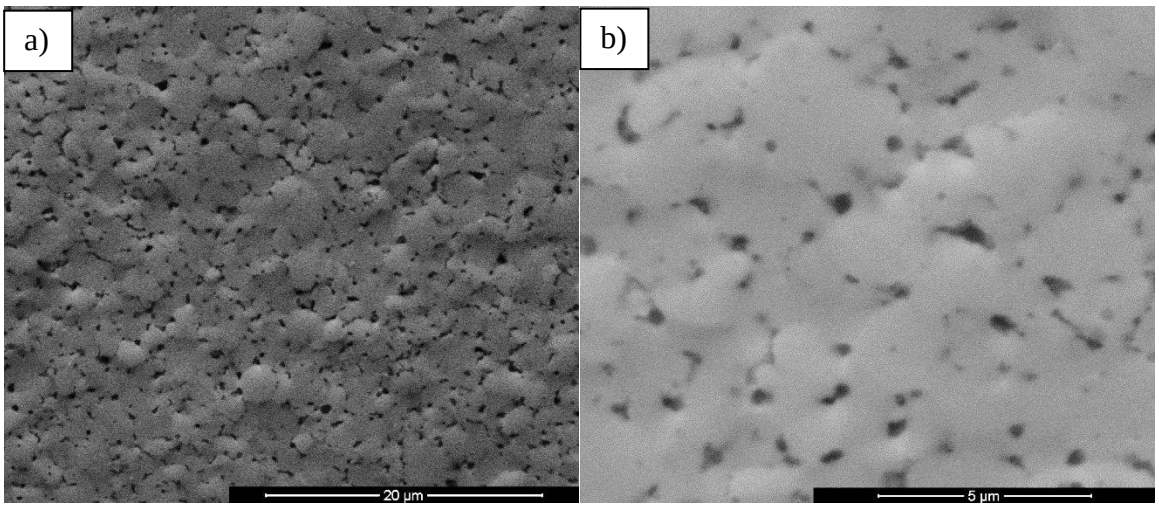

Figure 36: Micrographs of 3%TiC-ZrO_2 sintered at 1600°C 50 MPa at different magnifications

Figures 35 and 36 show the micrographs of the 3% TiC carbide samples sintered at 1500 and 1600^{o}C, both at 50 MPa. The grain growth of the Zirconia has been significant with grain size in the region of 2 µm. The increase in temperature has further increased the grain size but not significantly.

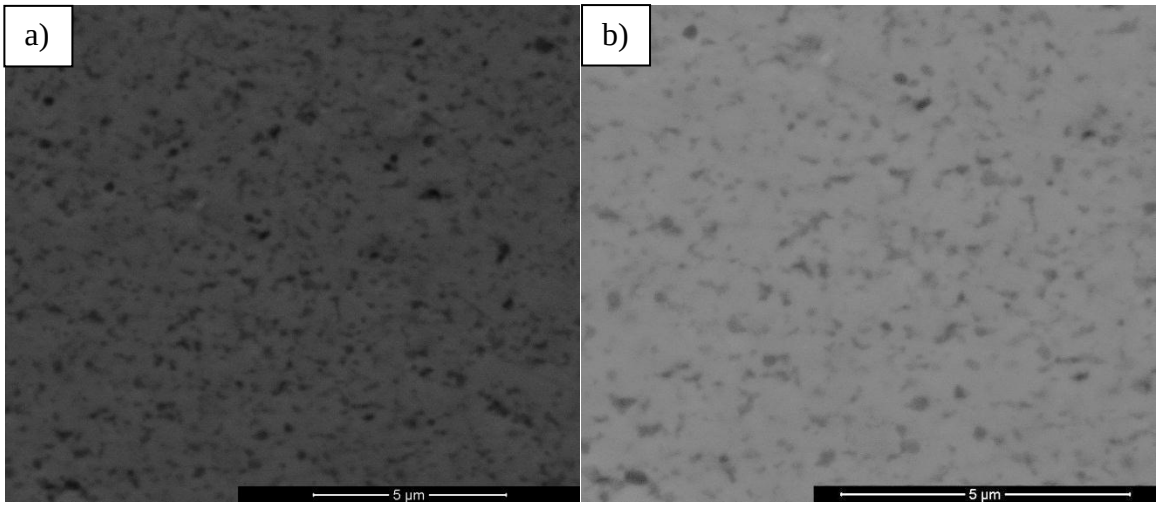

Figure 37: Micrographs of 10%TiC-ZrO_2 sintered at 1500°C 30 MPa at different magnifications

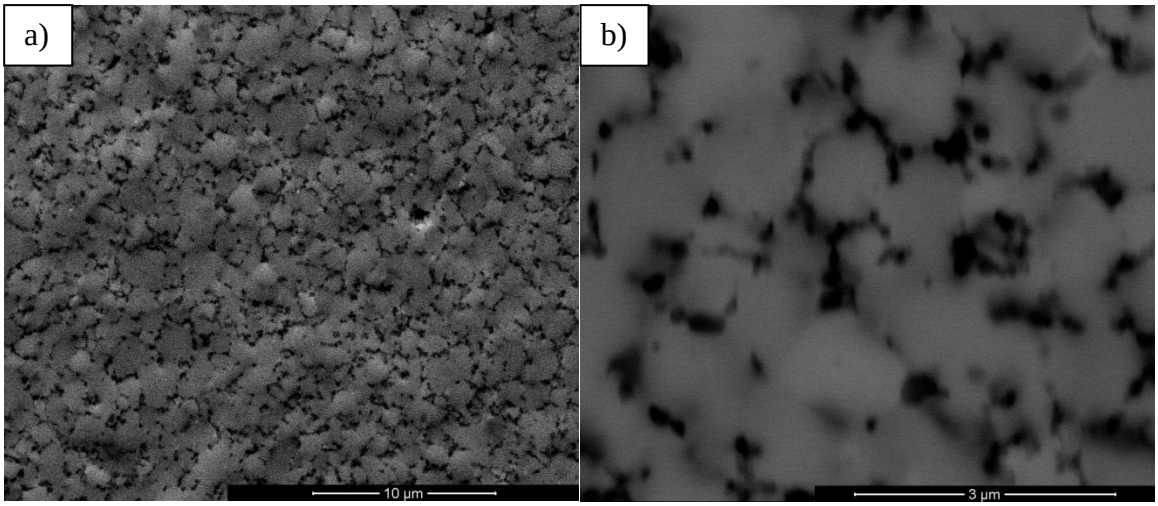

Figure 38: Micrographs of 10%TiC-ZrO_2 sintered at 1600°C 30 MPa at different magnifications and different detectors a) SE b) BS

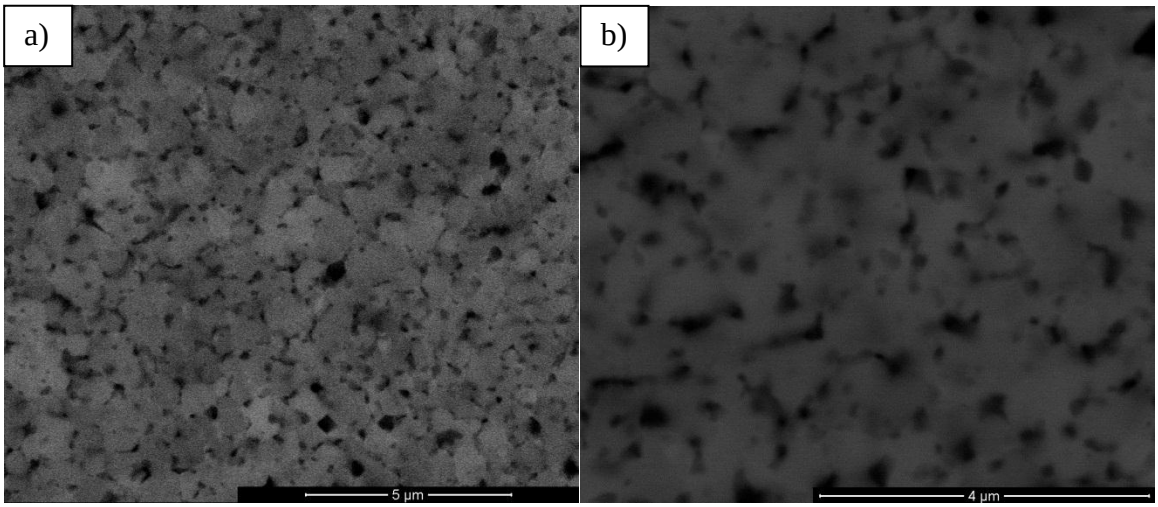

Figure 39: Micrographs of 10%TiC-ZrO_2 sintered at 1600°C 50 MPa at different magnifications and different detectors a) SE b) BS

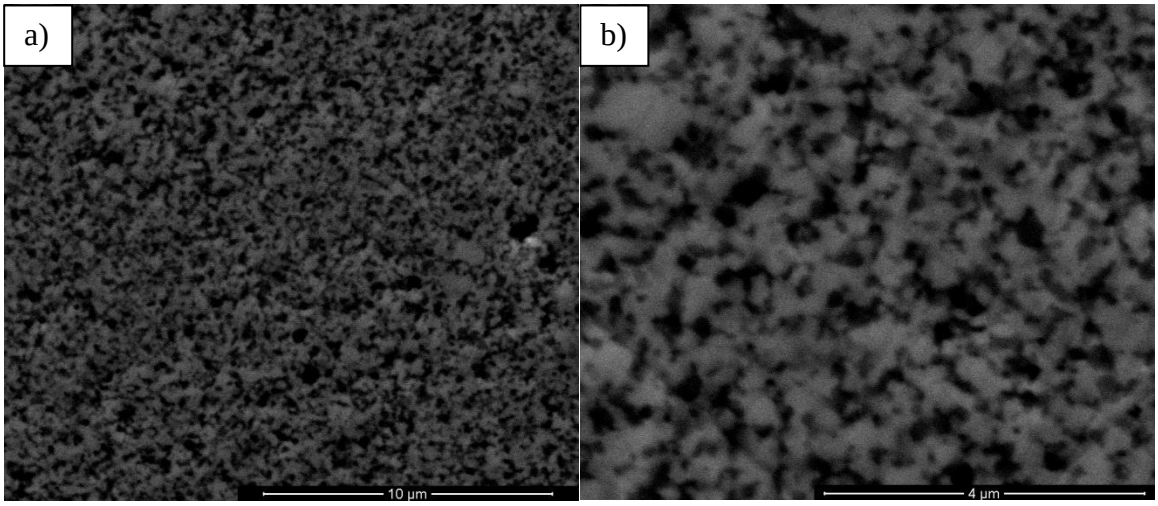

Figure 40: Micrographs of 30%TiC-ZrO_2 sintered at 1600°C 50 MPa at different magnifications

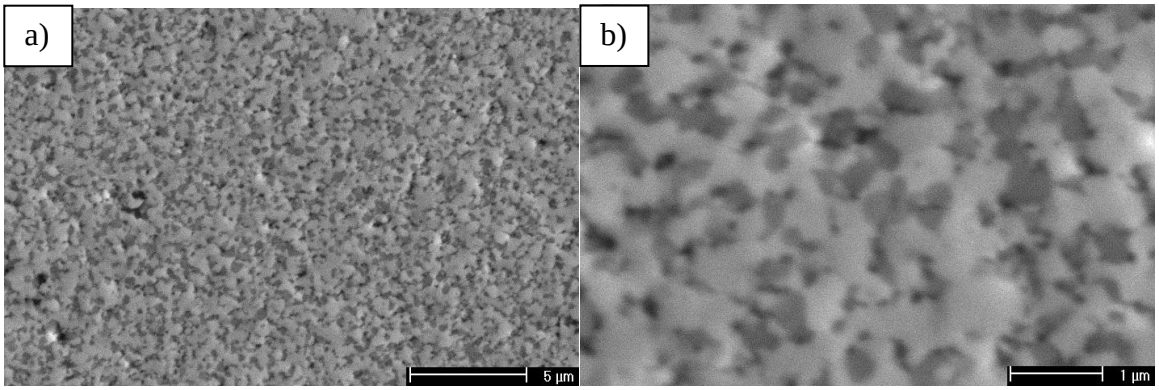

Figure 41: Micrographs of 30%TiC-ZrO_2 sintered at 1700°C 50 MPa at different magnifications

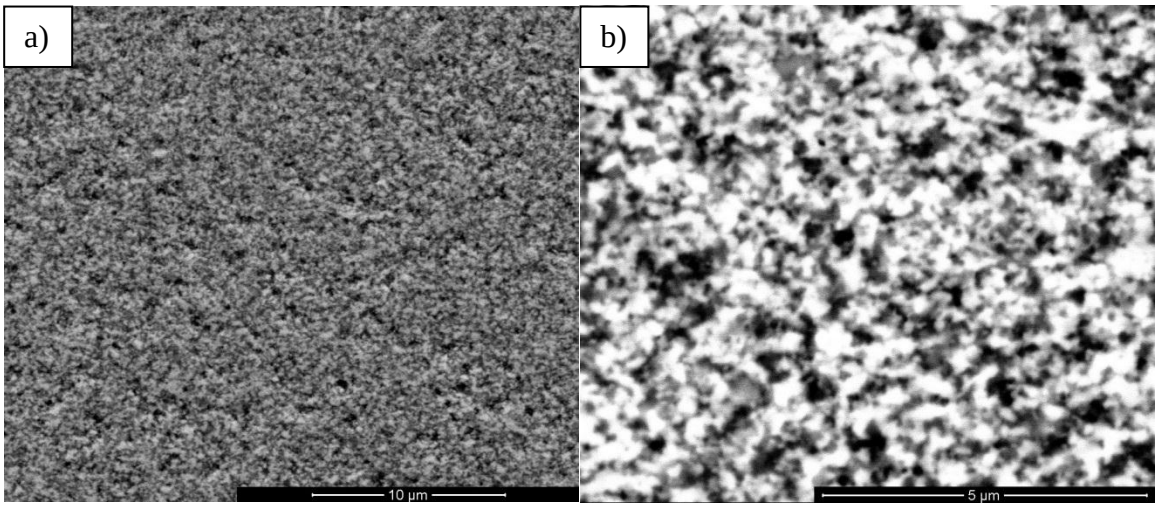

Figure 42: Micrographs of 50%TiC-ZrO_2 sintered at 1500°C 50 MPa at different magnifications and different detectors a) SE b) BS

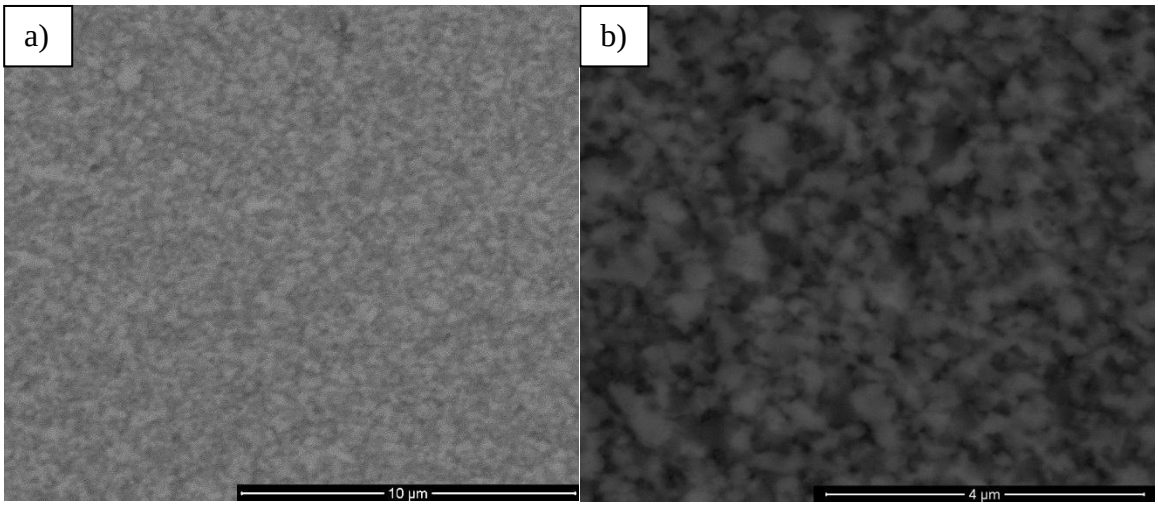

Figure 43: Micrographs of 50%TiC-ZrO_2 sintered at 1600°C 50 MPa at different magnifications

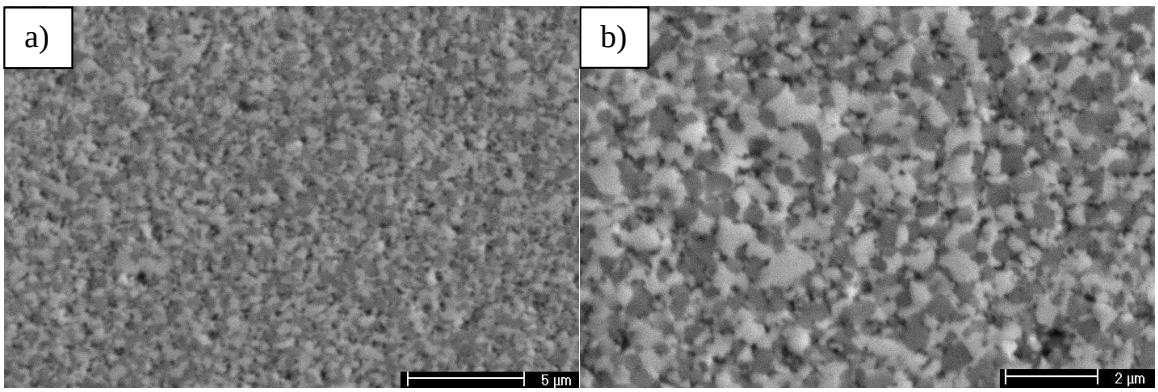

Figure 44: Micrographs of 50%TiC-ZrO_2 sintered at 1800°C 65 MPa a) low magnification b) high magnification

For the 30% TiC content samples sintered at 1500°C, 1600°C and 1700°C at 50 MPa, it can be seen that the increase in temperature has reduced the number of pores with minimum increase in grain size for both phases, with the Zirconia having a grain size average of less than 1 µm. The 50% TiC samples show a similar pattern to the previous TiC content sample. Each of 50% samples is more porous then the 30% sintered at similar conditions. The grain growth of these samples can be seen to be significant when comparing Figures 42 and 44. It can be seen that the grain sizes have approximately doubled, from an average of ±0.5 to ±1 µm by increasing the temperature from 1500°C to 1800°C. However it can also be seen that the higher TiC content has significantly reduced grain growth when comparing these to the 3 and 10% samples.

Zirconia - Titanium Nitride

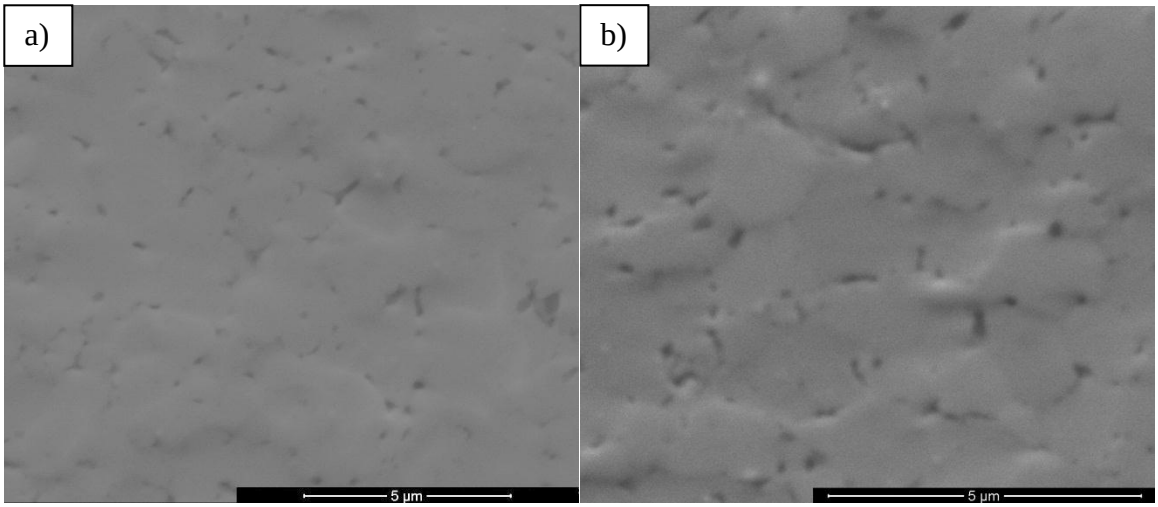

Figure 45: Micrographs of 3%TiN-ZrO_2 sintered at 1500°C 50 MPa at different magnifications

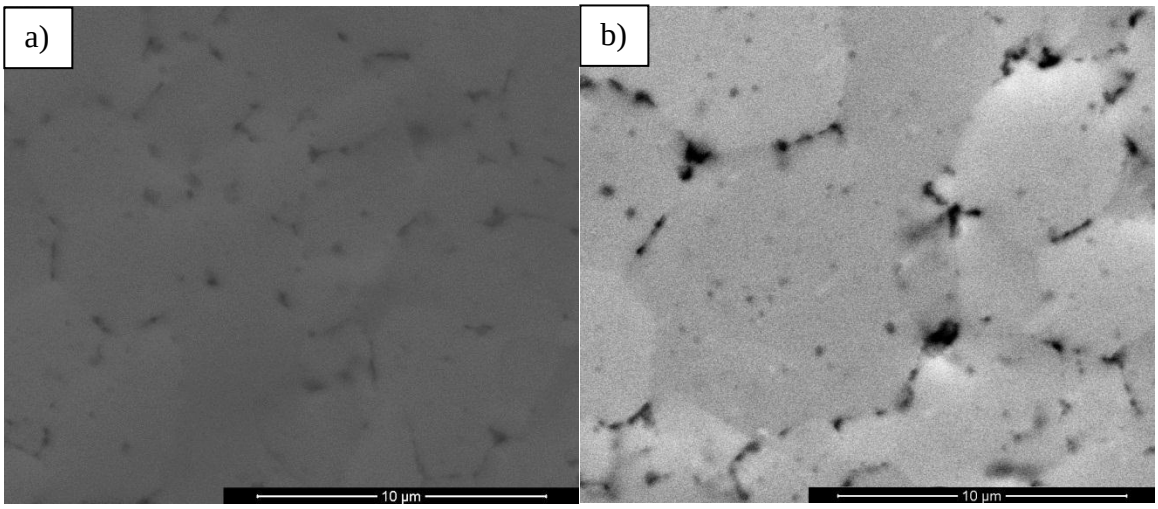

Figure 46: Micrographs of 3%TiN-ZrO_2 sintered at 1600°C 50 MPa at different magnifications

Figures 45 and 46 show the 3 volume percent TiN samples sintered at 1500°C 50 MPa and 1600°C 50 MPa respectively. It can be seen that increasing sintering temperature has increased the grain size, with some very large grains in the 1600°C sample, up to 8 µm with an average of approximately 4 µm, compared to slightly above and below 2 µm for the sample sintered at 1500°C 50 MPa.

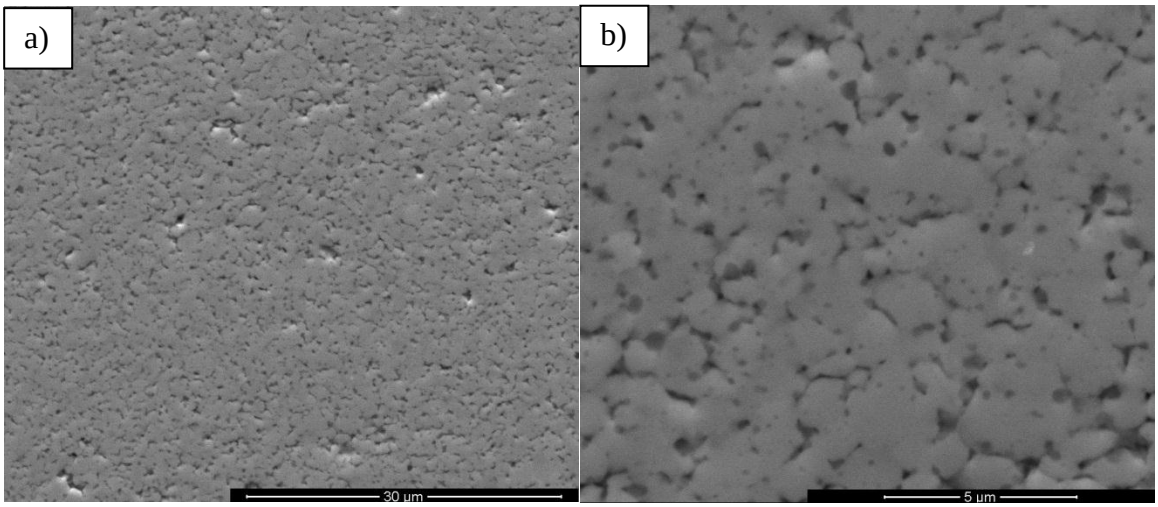

Figure 47: Micrographs of 10%TiN-ZrO_2 sintered at 1500°C 50 MPa at different magnifications and different detectors a) SE b) BS

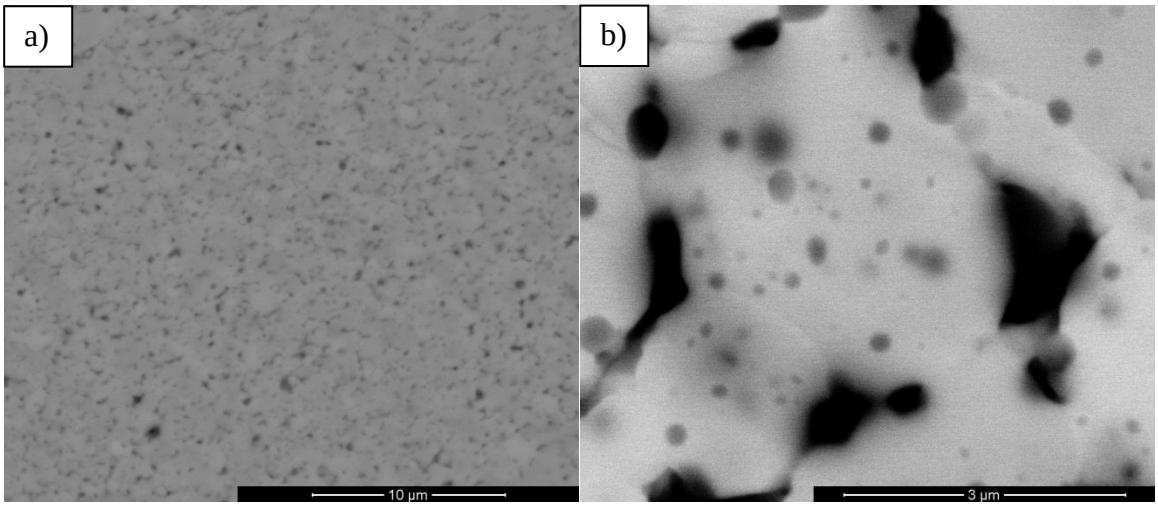

Figure 48: Micrographs of 10%TiN-ZrO_2 sintered at 1600°C 50 MPa at different magnifications and different detectors a) SE b) BS

The micrographs of the 10 vol% TiN content samples sintered at 1500°C 50 MPa and 1600°C 50 MPa are shown in Figures 47 and 48. The increase in density can be seen as a result of the increase in sintering temperature. There is grain growth occurring when increasing the temperature. At the same time an increase in porosity was observed.

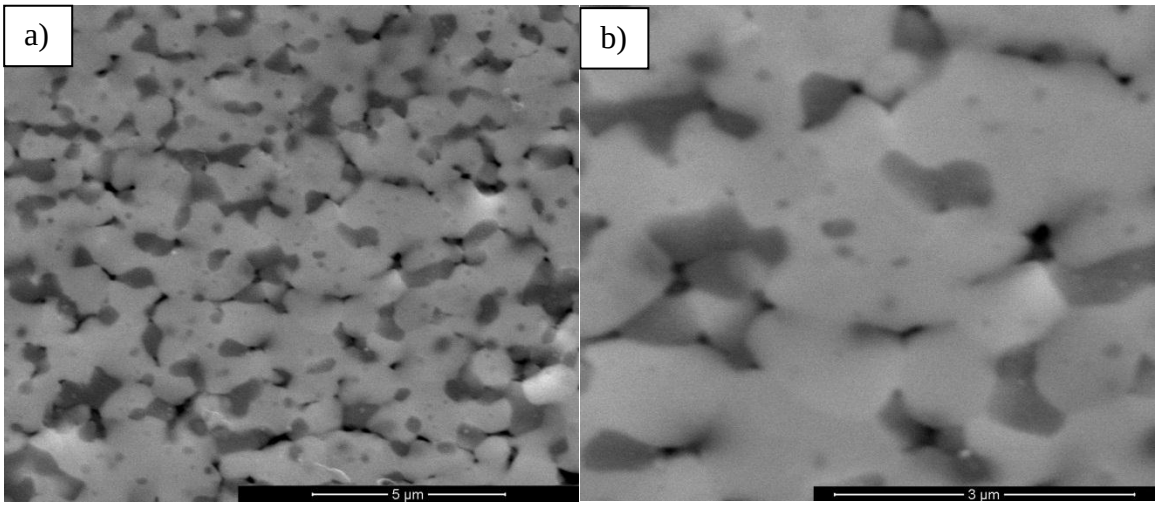

Figure 49: Micrographs of 30%TiN-ZrO_2 sintered at 1600°C 50 MPa at different magnifications

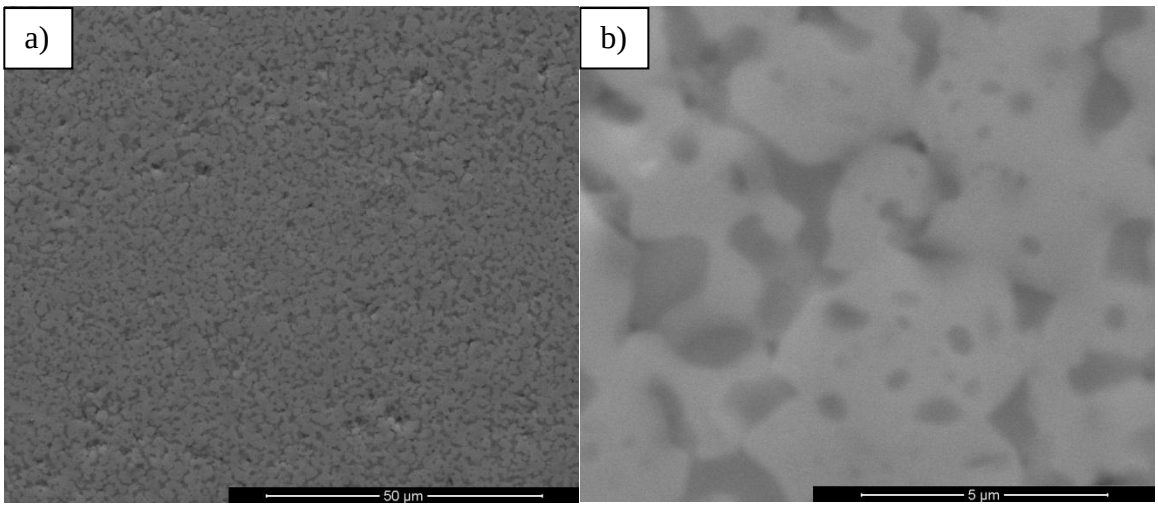

Figure 50: Micrographs of 30%TiN-ZrO_2 sintered at 1700°C 50 MPa at different magnifications

Figures 50 and 51, show the 30% TiN content samples sintered at 1600°C 50 MPa and 1700°C 50 MPa respectively. The samples appear to be dense with minimal porosity. As with previous compositions the amount of pores has been reduced with increasing density. The grain growth can be seen to be hindered by the increase in TiN content when comparing to the 10% samples, with both figures showing Zirconia grains in the region of 2 µm.

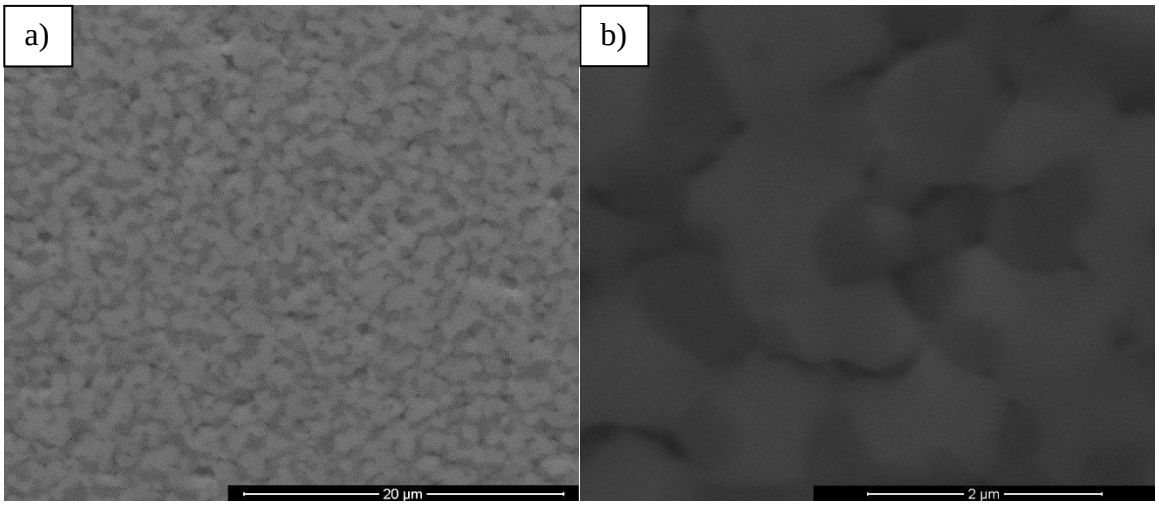

Figure 51: Micrographs of 50%TiN-ZrO_2 sintered at 1600°C 50 MPa at different magnifications

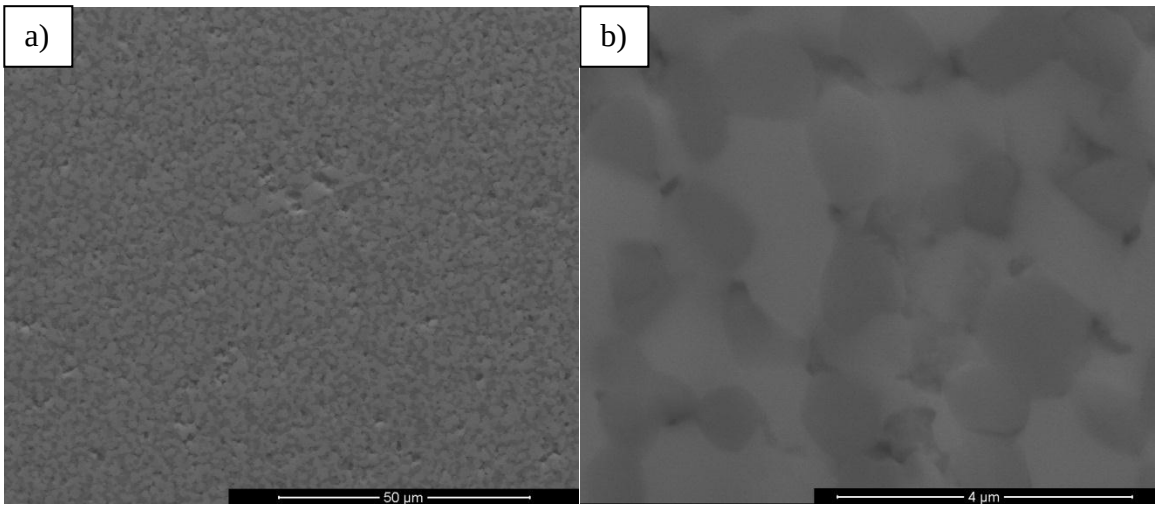

Figure 52: Micrographs of 50%TiN-ZrO_2 sintered at 1700°C 50 MPa at different magnifications

Figure 51 and Figure 52 show the 50% TiN by volume content sample sintered at 1600°C 50 MPa and 1700°C 50 MPa respectively. As is the case for the TiC-containing composites, the 50% TiN samples are more porous than the 30% ones. However both samples do appear to be dense. The Zirconia grains are approximately 1 µm in size. This is smaller than that in the 30% samples.

When referring to the SEM micrograph images, it can be seen that the samples are denser than calculated with the original theoretical density. This is most evident in the higher reinforcing powder content samples. The recalculated theoretical densities including the

oxygen content show a better correlation with these images. This is especially prominent in the TiN samples which were found to have much higher oxygen content. However TiO_2 was not found during SEM of the sample, even after thorough examination. This is because TiO_2 is soluble in ZrO_2 [49] [50] [51], up to 18 mol% [49] [51].

4.2.2.3. Results of Hardness and Fracture Toughness for Nanocomposites

The hardness and fracture toughness results for the ZrO_2-TiC and ZrO_2-TiN nanocomposites are shown in Tables 17 and 18 respectively. The hardness and fracture toughness of the sintered materials were measured by the indentation technique using a Vickers indenter with a LECO V-100-A2 Vickers Hardness Tester machine. A load of 5 kg was used for each measurement.

Table 17: Summary of the properties ZrO_2–TiC composite materials sintered at different conditions

Sample Name.	%TiC	Temperature (°C)	Pressure (MPa)	Theoretical Density (g/cm^3)	Bulk Density (g/cm^3)	Relative Density (%)	Hv (GPa)	Std. Dev.	KiC ($MPa.m^{1/2}$)	Std. Dev.
3 vol% TiC-ZrO_2, 1500°C, 30 MPa	3%	1500	30	5.832	5.830	99.6	13.33	0.21	1.79	0.09
3 vol% TiC-ZrO_2, 1500°C, 50 MPa	3%	1500	50	5.832	5.835	99.7	12.94	0.09	2.08	0.15
3 vol% TiC-ZrO_2, 1600°C, 30 MPa	3%	1600	30	5.832	5.837	99.8	13.40	0.21	1.66	0.05
3 vol% TiC-ZrO_2, 1600°C, 50 MPa	3%	1600	50	5.832	5.849	100	13.12	0.11	2.12	0.01
10 vol% TiC-ZrO_2, 1500°C, 30 MPa	10%	1500	30	5.723	5.684	98.3	13.66	0.25	1.69	0.18
10 vol% TiC-ZrO_2, 1500°C, 50 MPa	10%	1500	50	5.723	5.698	98.5	13.53	0.29	2.26	0.08
10 vol% TiC-ZrO_2, 1600°C, 30 MPa	10%	1600	30	5.723	5.706	98.7	13.70	0.17	1.87	0.06
10 vol% TiC-ZrO_2, 1600°C, 50 MPa	10%	1600	50	5.723	5.722	98.9	13.61	0.26	2.12	0.09
30 vol% TiC-ZrO_2, 1500°C, 30 MPa	30%	1500	30	5.421	5.375	96.1	10.87	0.12	2.41	0.19
30 vol% TiC-ZrO_2, 1500°C, 50 MPa	30%	1500	50	5.421	5.389	96.3	11.88	0.17	2.76	0.09
30 vol% TiC-ZrO_2, 1600°C, 50 MPa	30%	1600	50	5.421	5.406	96.6	12.21	0.33	2.23	0.21
30 vol% TiC-ZrO_2, 1700°C, 50 MPa	30%	1700	50	5.421	5.418	96.9	13.75	0.21	2.29	0.18
50 vol% TiC-ZrO_2, 1500°C, 30 MPa	50%	1500	30	5.357	4.872	90.1	7.20	0.33	3.00	0.14
50 vol% TiC-ZrO_2, 1500°C, 50 MPa	50%	1500	50	5.357	5.085	94.1	9.47	0.50	2.19	0.13
50 vol% TiC-ZrO_2, 1600°C, 30 MPa	50%	1600	30	5.357	5.079	94.0	10.70	0.24	3.61	0.28
50 vol% TiC-ZrO_2, 1600°C, 50 MPa	50%	1600	50	5.357	5.186	96.0	12.08	0.38	2.53	0.23
50 vol% TiC-ZrO_2, 1700°C, 50 MPa	50%	1700	50	5.357	5.207	96.3	12.39	0.29	2.59	0.19
50 vol% TiC-ZrO_2, 1800°C, 65 MPa	50%	1800	65	5.357	5.255	97.2	12.64	0.31	2.65	0.27

Table 18: Summary of the properties ZrO_2–TiN composite materials sintered at different conditions

Sample Name.	%TiN	Temperature (°C)	Pressure (MPa)	Theoretical Density (g/cm^3)	Bulk Density (g/cm^3)	Relative Density (%)	Hv (GPa)	Std. Dev.	KiC ($MPa.m^{1/2}$)	Std. Dev.
3 vol% TiN-ZrO_2, 1500°C, 30 MPa	3%	1500	30	5.853	5.824	99.51	13.24	0.21	1.63	0.09
3 vol% TiN-ZrO_2, 1500°C, 50 MPa	3%	1500	50	5.853	5.832	99.65	13.90	0.25	1.73	0.11
3 vol% TiN-ZrO_2, 1600°C, 30 MPa	3%	1600	30	5.853	5.841	99.80	13.73	0.26	1.61	0.08
3 vol% TiN-ZrO_2, 1600°C, 50 MPa	3%	1600	50	5.853	5.852	99.98	14.25	0.15	1.51	0.12
10 vol% TiN-ZrO_2, 1500°C, 30 MPa	10%	1500	30	5.792	5.710	98.58	13.33	0.34	2.07	0.29
10 vol% TiN-ZrO_2, 1500°C, 50 MPa	10%	1500	50	5.792	5.731	98.94	14.04	0.25	2.39	0.13
10 vol% TiN-ZrO_2, 1600°C, 50 MPa	10%	1600	50	5.792	5.745	99.18	14.47	0.24	1.70	0.10
10 vol% TiN-ZrO_2, 1700°C, 50 MPa	10%	1700	30	5.792	5.773	99.67	13.94	0.39	1.90	0.11
30 vol% TiN-ZrO_2, 1600°C, 50 MPa	30%	1600	50	5.622	5.570	99.06	14.70	0.27	2.52	0.19
30 vol% TiN-ZrO_2, 1700°C, 50 MPa	30%	1700	50	5.622	5.594	99.49	15.79	0.38	2.87	0.17
50 vol% TiN-ZrO_2, 1600°C, 50 MPa	50%	1600	50	5.457	5.313	97.36	12.19	0.31	3.02	0.24
50 vol% TiN-ZrO_2, 1700°C, 50 MPa	50%	1700	50	5.457	5.338	97.83	13.37	0.31	3.64	0.13

5. Discussion

5.1 Powder Characterisation and Preparation before Sintering

From the powder characterisation measurements it is evident that both the micron and nano sized powders were in the expected size ranges. Combining the BET and particle size results shows that the surface areas of the powders were also in the expected range, since the surface area of the powders increased with decreased particle size. It was therefore expected that the amount of Lubrizol to disperse the powders would have increased with decreased particle size and/or increased surface area. This was found to be true as shown in Table 19 and 20, which show a summary of the rheology results for the single powder system of the micron and nano sized powders respectively.

Table 19: Summary of powder characterisation and rheology results for micron powders

Sample	**Particle Size (nm)**	**Surface Area (m^2/g)**	**Optimal Lubrizol Content (wt. %)**	**Solid loading (Volume %)**	**Mass Lubrizol per unit area powder (mg/m^2)**	**Viscosity (@100, Pa.s)**
8Y-ZrO_2	570	5.5	3	30	5.4	0.04
TiC	2500	1.9	1.1	50	5.8	0.09
TiN	2580	1.9	1.7	50	9.0	0.07

Table 20: Summary of powder characterisation and rheology results for nanopowders

Sample	**Particle Size (nm)**	**Surface Area (m^2/g)**	**Optimal Lubrizol content (wt. %)**	**Solid loading (Volume %)**	**Mass Lubrizol per unit area powder (mg/m^2)**	**Viscosity (@100, Pa.s)**
8Y-ZrO_2	28	15.3	5	30	4.1	0.06
TiC	40	23.7	8.3	15	3.5	0.20
TiN	20	61.3	9	3.2	1.5	0.17

It was observed that lower solids loading was used for the micron 8Y-Zirconia than the micron TiC and TiN powders; this is due to the zirconia having smaller particle size and a significantly higher surface area. Because of this a solid loading of above 30 vol% for the 8Y-Zirconia was difficult to disperse, unlike the micron TiC and TiN for which a solids loading of 50 vol% was used. The micron zirconia had a lower viscosity at the optimal suspension conditions which indicated that a higher solids loading or lower Lubrizol weight percentage could be used. It was also clear that the amount of Lubrizol 2155 required was material dependent, since the micron sized TiC and TiN powders had similar surface areas, and particle sizes, but the TiN powder required more Lubrizol in order to be optimally dispersed.

The zirconia systems in each size range were easier to disperse than the TiC and TiN powders, with a lower viscosity being reached at the optimal dispersant level compared to the TiC and TiN powders. When comparing the micron and nanosized zirconia powders, a direct comparison could be made because the same solids loading were used. Due to the increased surface area of the nano sized zirconia powder, more than double that of the micron sized powder, a higher weight percent Lubrizol was required. However it must be noted that the final viscosity for both the micron and nano sized zirconia, at the optimal Lubrizol content, were in a similar range. It can also be seen that the viscosities of the nano reinforcing powders are significantly higher than those of the micron sized powders at the optimal dispersion conditions. This happened even though a higher Lubrizol content and much lower solids loading were used. This was due to the surface area of the nano reinforcing powders being significantly higher than that of the micron powders. Specifically, the surface area of the nanosized TiC and TiN was 10-30 times greater than that of the corresponding micron powders. This difference is much greater than the surface area difference of the micron and nanosized zirconia.

When comparing the rheology results of the nano TiC and TiN to that of the micron TiC and TiN powders it could be seen that a lower amount of Lubrizol mass per unit area of the powder was required for the nanopowders, but at significantly lower solid loading volumes than micron powders. This trend could also be seen when comparing the TiC and TiN nanopowders; the TiN had a lower Lubrizol mass per unit area and a lower solid loading volume compared to the TiC which had a particle size double that than the TiN. The viscosities of the nanosized TiC and TiN

were still significantly higher than those of the micron sized TiC and TiN, at the optimal conditions. This suggested that even lower solids loadings might be required to achieve the same level of dispersion as the micron sized powders.

The optimal amounts of Lubrizol for the mixtures are shown in Table 21, with the expected Lubrizol amounts and expected solids loading. The expected values were calculated using weighted percentages from the individual rheology results. These were used as a basis to begin the rheology studies for the composite mixtures.

It could be seen that the optimal Lubrizol amount was higher than the expected amount for each system. However, the optimal solid loading was the same as the expected amount. This was true for each system apart from the 50%TiN system which had a lower optimal solid loading lower optimal amount of Lubrizol than expected. This could indicate that there was some attraction between the reinforcing powder particles and the zirconia which must have to be overcome by increasing the Lubrizol amount.

By increasing the TiC/TiN content, from 10% to 50%, the viscosity had significantly increased in both the ZrO_2-TiC and ZrO_2-TiN systems. When comparing the viscosities in Tables 20 and 21, it could be seen that the viscosities of the 10% mixtures of TiC/TiN were significantly higher than the pure zirconia and the viscosities of the 50% mixtures were significantly higher than both the pure zirconia and individual reinforcing powders. This further indicated that there was some interaction between the zirconia and reinforcing powders.

Table 21: Summary of rheology results for nano composites mixtures

Material		Composition (Vol. %)	Optimal Solid loading (Vol. %)	Optimal Amount of Dispersant (Wt. %)	Viscosity (@100, Pa.s)	Expected Solid loading (Vol %)	Expected Amount of Dispersant (Wt. %)
ZrO_2	TiC	10	28.5	6.2	0.525	28.5	5.33
		50	22.5	6.9	0.904	22.5	6.65
	TiN	10	27.3	5.9	0.092	27.3	5.4
		50	5	6.8	0.216	16.6	7

5.2 Sintering and Mechanical Properties

It was noticed that the relative densities of the sintered composites differed not only with sintering conditions but also with composition. The sintering parameters changed were temperature and pressure.

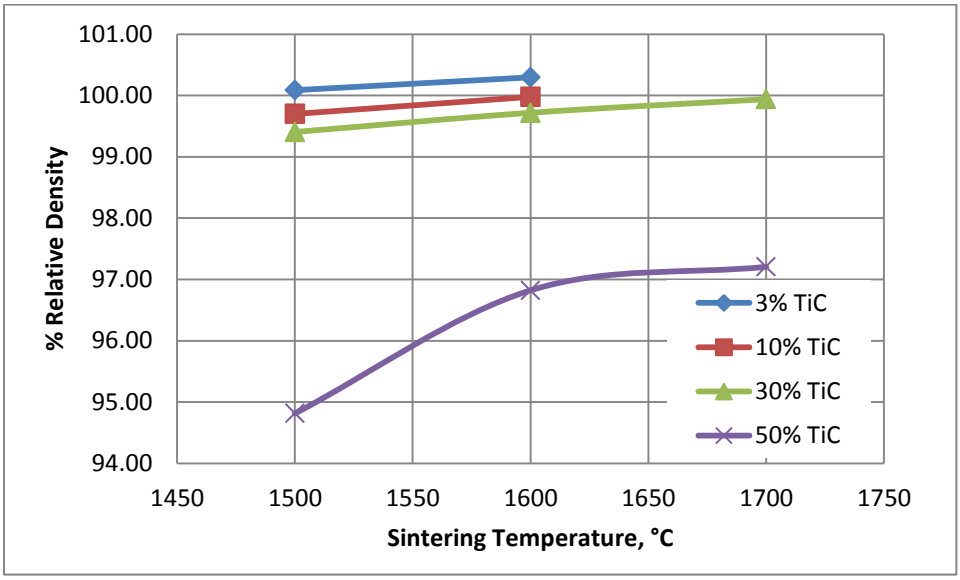

Figure 53: Effect of sintering temperature on density of ZrO_2-TiC nanocomposites, sintered at a pressure of 50 MPa

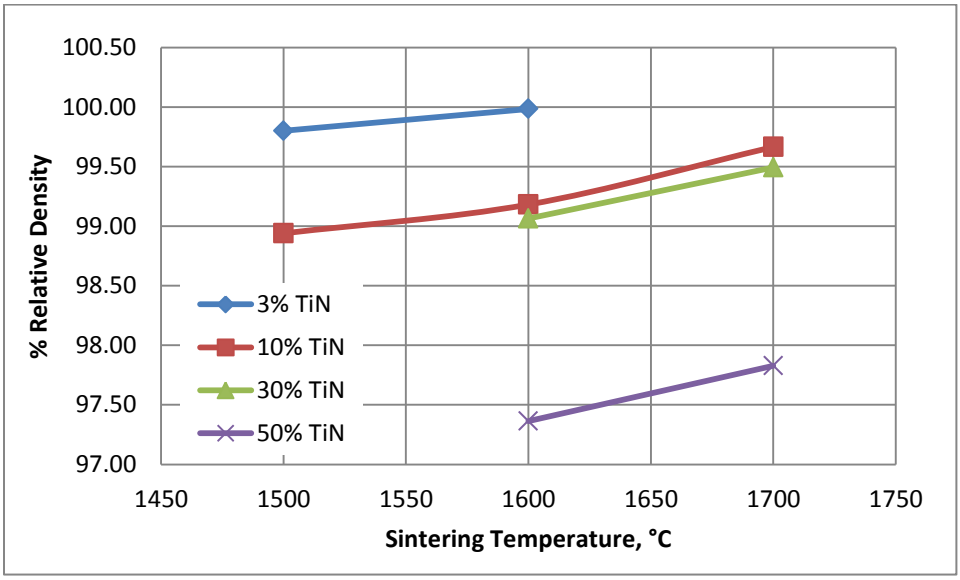

Figure 54: Effect of sintering temperature on density of ZrO_2-TiN nanocomposites, sintered at a pressure of 50 MPa

Figures 53 and 54 show the effect of sintering temperature on the densities of the nanosized ZrO_2-TiC and ZrO_2-TiN systems respectively, sintered at a pressure of 50 MPa. It could be seen that in both groups of materials that increased temperatures has resulted in an increased density at each of the reinforcing powder contents. However, it was noted that the densities of each system are decreasing with increasing TiC/TiN content at similar sintering temperatures. This will be discussed at a later stage.

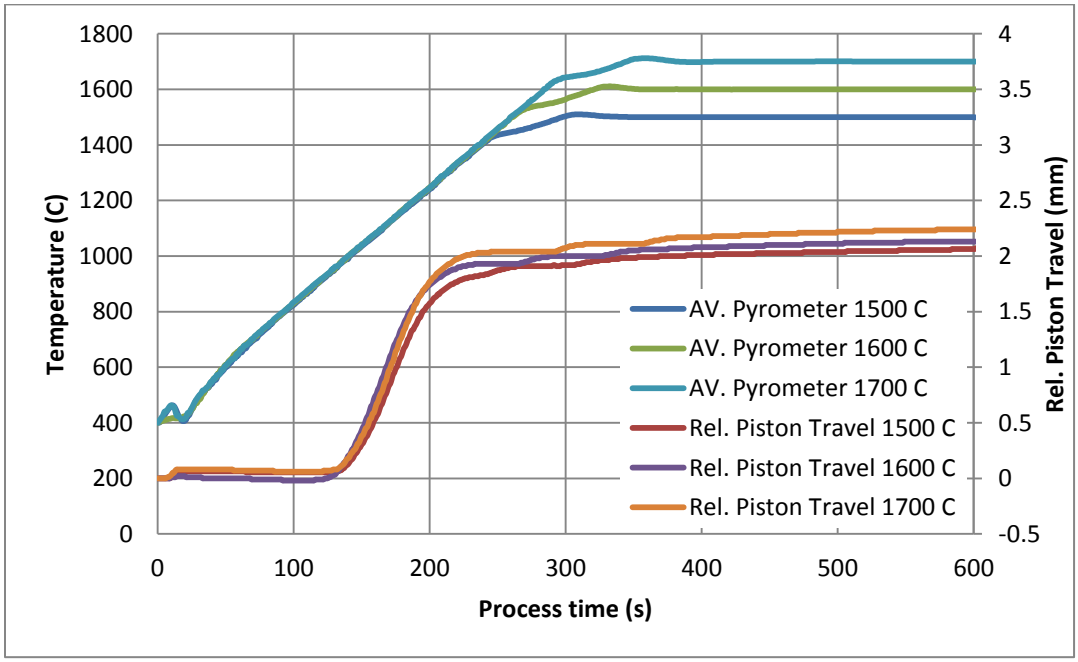

Figure 55: Sintering curves for 50 vol% TiC at varying sintering temperatures, sintered at a pressure of 50 MPa

The effect of temperature on density is shown in Figure 55 which shows sintering curves for 50 vol% TiC-ZrO_2, for varying sintering temperatures at 50 MPa. It could be seen that increased sintering temperatures resulted in greater densification due to a greater piston travel during the final sintering temperature. The reason for this increase in piston travel with increased temperature was due to the increase in densification during the sintering process; as a result this caused a better packing of the powders and hence allowed a greater piston travel. This confirmed that there was better densification achieved when the temperature was increased. This was found to be true for both systems for each of the TiC/TiN contents.

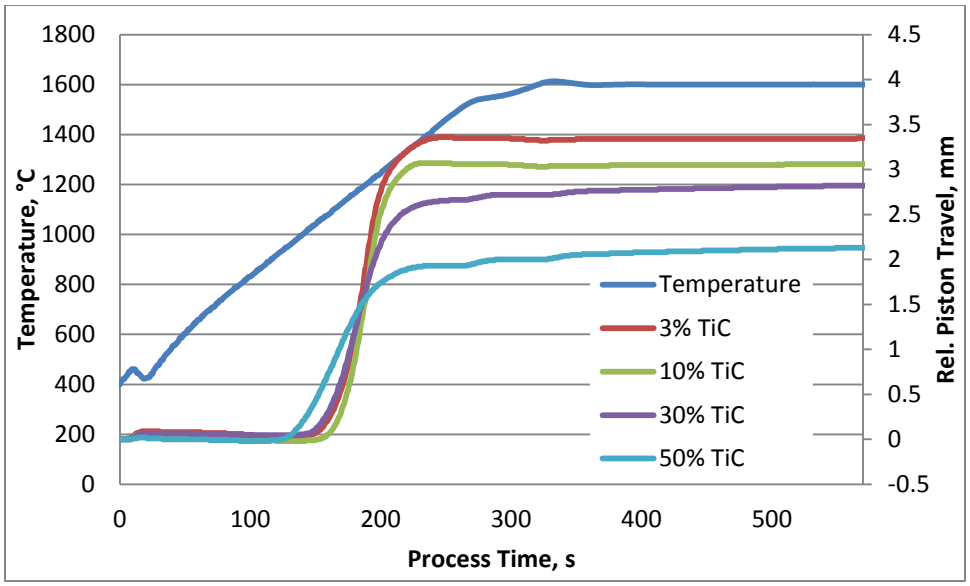

Figure 56: Sintering curves for ZrO_2-TiC nanocomposites at a sintering temperature of 1600°C

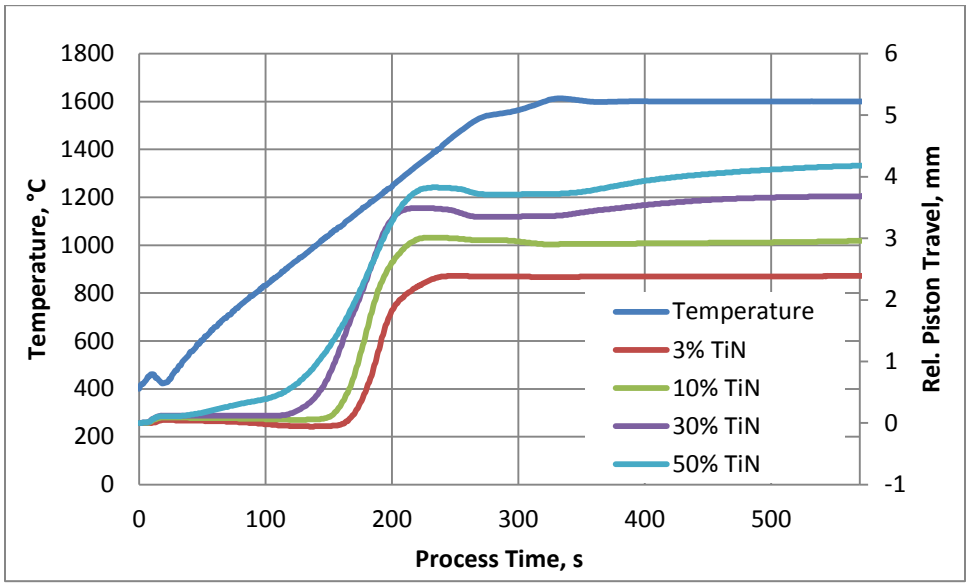

Figure 57: Sintering curves for ZrO_2-TiN nanocomposites at a sintering temperature of 1600°C

Figures 56 and 57 show the sintering curve for the various amounts of TiC and TiN respectively, sintered at a temperature of 1600°C and a pressure of 50 MPa. For the ZrO_2-TiC nanocomposites systems it could be seen that the piston travel was greatest for lower TiC contents. This might explain why higher densities were achieved for the lower TiC contents at 1600°C. The opposite was found to be true for the ZrO_2-TiN nanocomposite with a greater piston travel being achieved

for the higher TiN content sample. Yet better densities were obtained for the lower TiN-content samples similarly to the TiC-containing composites. This was because the TiN nanopowder was far more 'fluffy' than both the ZrO_2 and TiC nanopowders, with a small mass of powder occupying a far larger volume than the ZrO_2 and TiC nanopowders. Thus, during sintering the piston was allowed to travel further for the higher TiN contents than the lower contents.

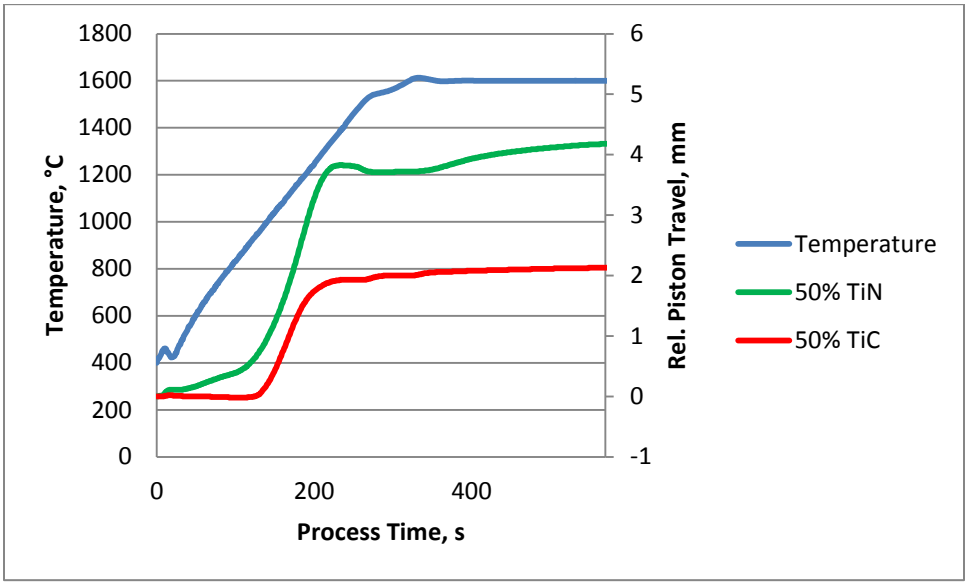

Figure 58: Comparison of sintering curves for ZrO_2-TiC and ZrO_2-TiN nanocomposites at a sintering temperature of 1600°C

A comparison between the sintering curves for the 50 volume percent TiC and TiN is shown in Figure 58. The difference in piston travel was clearly seen, indicating that the piston travel was far greater in the TiN nanocomposite. This, as described earlier, was due to the nano TiN being more of a 'fluffy' powder than the nano TiC.

The lower relative densities of the higher reinforcing powder content samples was due to the samples not fully densifying, even when going to high sintering temperatures and a higher sintering pressure. This effect was most notable in the 50 volume percent of TiC/TiN samples. An explanation for this might be that the reinforcing particles retarded the sintering rate of the zirconia matrix. At higher TiC and TiN contents there are formations of rigid percolating networks which were a major impedance to densification[20]. Towards a 30 volume percent

reinforcing powder content there was a percolation limit that was reached which prevented the zirconia grains from growing and plastically deforming, thus it reduced the sinterability of the samples. Therefore, in order to densify higher sintering temperatures were required. A similar finding was also made in a study on cubic zirconia and SiC, in which the presence of SiC particles inhibited grain growth and densification and hence high sintering temperatures of 1680-1720°C were required to densify the samples [23].

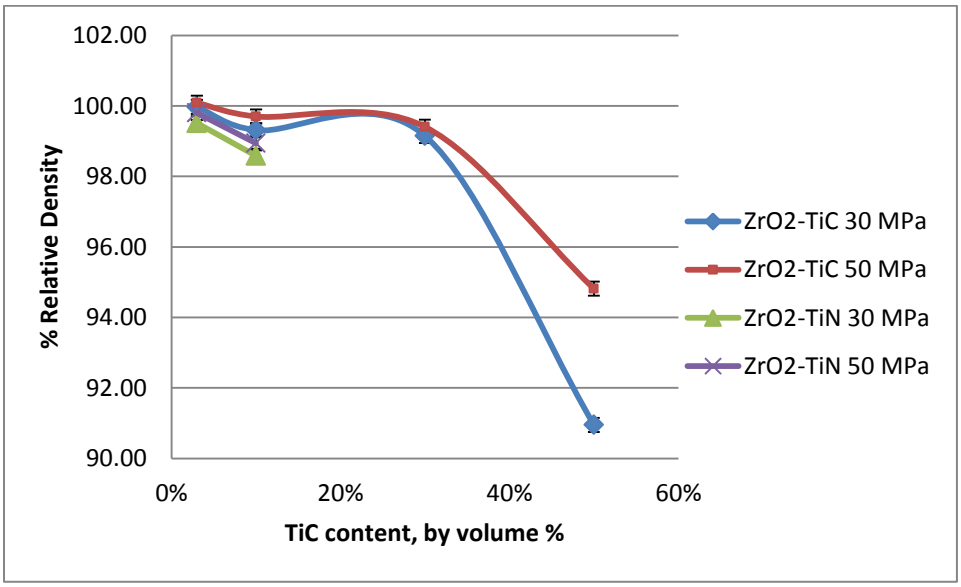

Figure 59: The effect of pressure on density of ZrO_2-TiC and ZrO_2-TiN nanocomposites

The effects of pressure on the density of the ZrO_2-TiC and ZrO_2-TiN nanocomposites, sintered at a temperature of 1500°C are shown in Figure 59. It could be seen in both images that the increase in pressure resulted in an increase in density for both composite systems; however, this effect was minimal, within the error, at lower reinforcing phase volume fractions. The increased densification as a result of pressure for the 50% TiC-ZrO_2 was caused by improved particle packing resulting from the additional pressure applied prior to the rise in temperature. Since the densities of the samples were greatly influenced by the percolating networks which eventually inhibited densification, the additional pressure increased the final density of the samples by having broken down the network of particles and improved the particle packing [20].

Because of the better densities achieved when a pressure of 50 MPa was used, the 30 and 50 volume percent TiN composites were only sintered at 50 MPa, and hence no comparison could be made for these compositions at 30 MPa. It could further be seen in Figure 59 that increased TiC content resulted in lower relative densities.

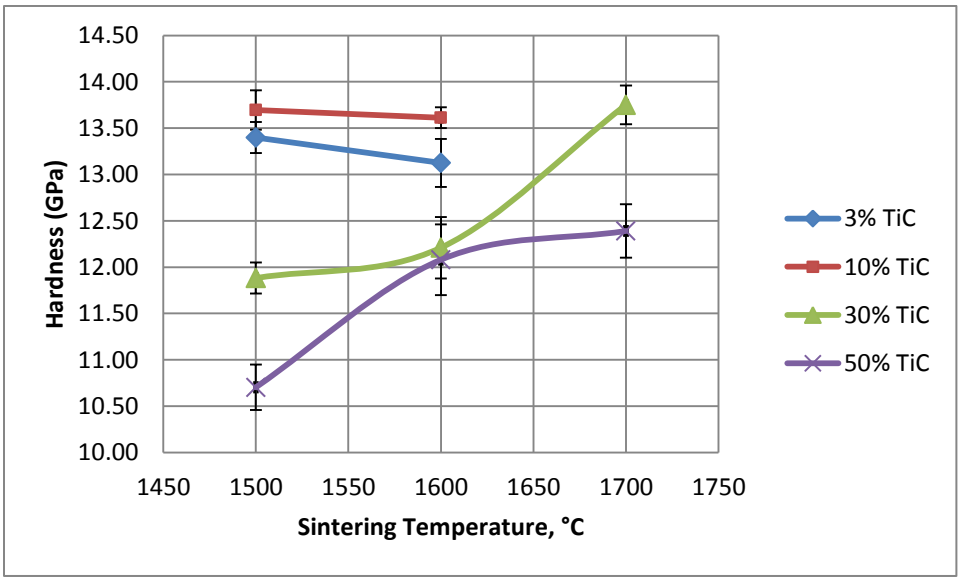

Figure 60: Effect of sintering temperature on hardness of ZrO_2-TiC nanocomposites

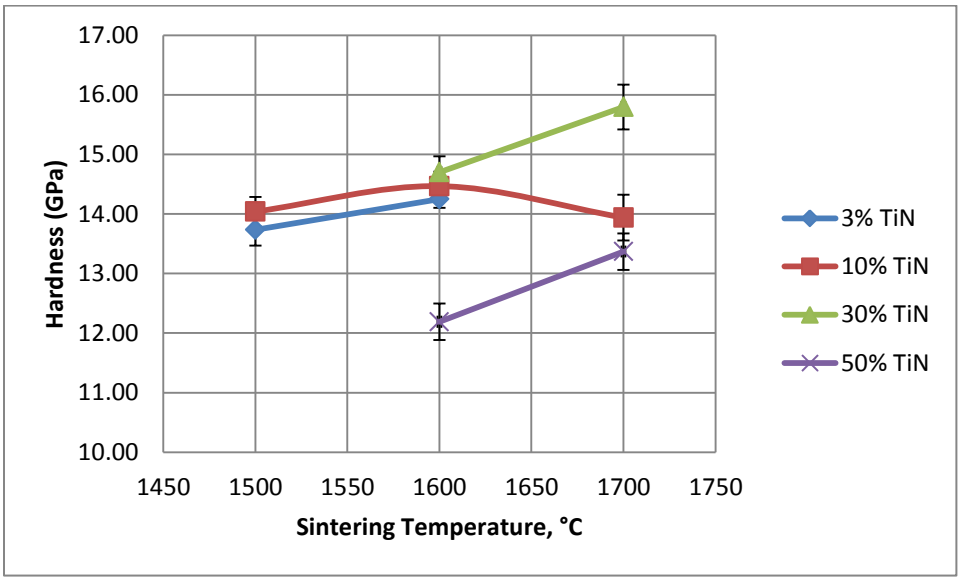

Figure 61: Effect of sintering temperature on hardness of ZrO_2-TiN nanocomposites

The effect of sintering temperature on the hardness of the ZrO_2-TiC and ZrO_2-TiN nanocomposites are shown in Figures 60 and 61. For the 3 and 10% TiC samples it appeared that their hardnesses decreased as the sintering temperature increased from 1500°C to 1600°C. This could be explained by the effect of grain growth on hardness with increased sintering temperature resulted in increased grain size without a significant change in density. This could be further illustrated when referring to the microstructure of the samples. A similar case was found for the 10%TiN content samples. This effect was found at a higher sintering temperature of 1700°C. A similar case would be expected for the 3%TiN content samples if a sintering temperature of 1700°C was used. This illustrated the Hall-Petch relationship for the lower TiC content samples, which were 'fully' densified at lower temperatures. A further increase in sintering temperature only increased the grain growth without affecting the densification significantly; hence the hardness deceased. This was not found to be the case for the 30 and 50% TiC/TiN samples which showed an increase in hardness with an increase in sintering temperature; this was as a result of increased density with increased sintering temperature, shown in Figures 53 and 54.

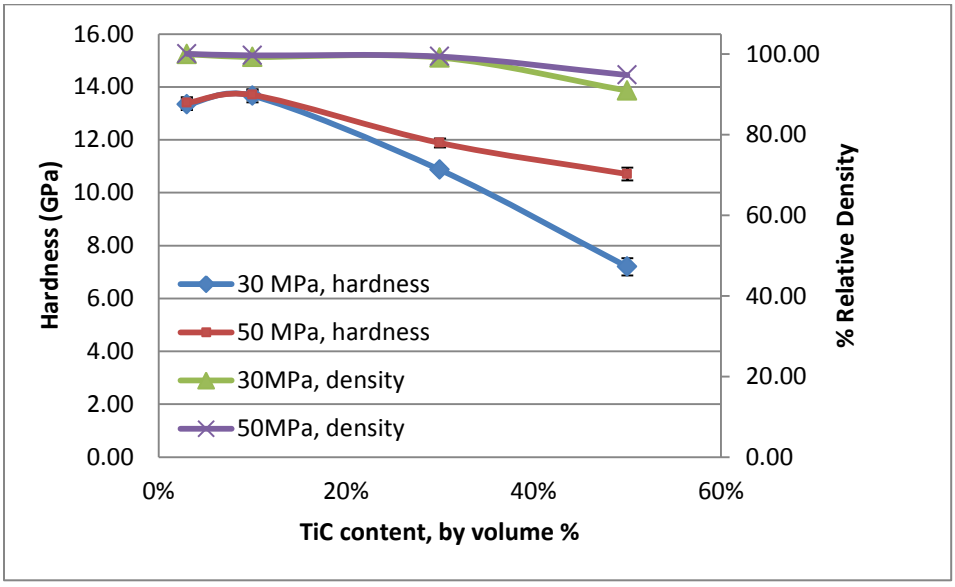

Figure 62: Effect of pressure on density and hardness for the ZrO_2-TiC nanocomposites sintered at 1500°C

Because the application of pressure increased the relative density without causing grain growth it was expected that the hardness would have increased with increased pressure. This is shown in Figure 62; the effect of pressure on hardness for varying TiC content was noticed. It could be seen that the hardness increased for the samples sintered at higher pressures. The densities of the samples are also shown in the figure, which showed that increased pressure resulted in an increased density. The effect of pressure was most notable on the hardness and density at higher TiC contents. This was discussed earlier as being a result of the additional pressure breaking down network of the reinforcing powder particles thus improving particle packing. A similar case was found to be true for the 3 and 10%TiN nanocomposites which were sintered at different pressures, and hence the 30 and 50% TiN nanocomposites were sintered only using a pressure of 50 MPa.

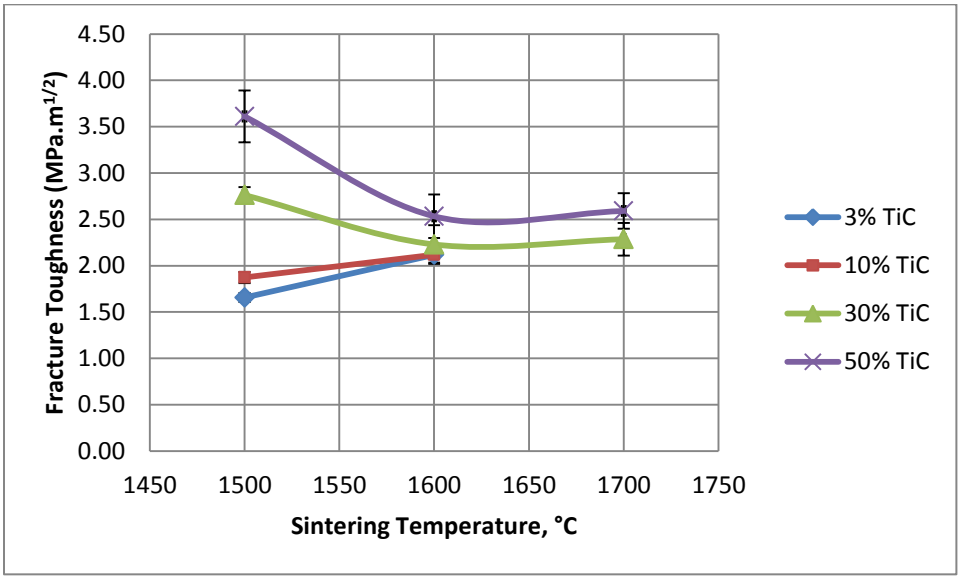

Figure 63: Effect of sintering temperature on fracture toughness of ZrO_2-TiC nanocomposites

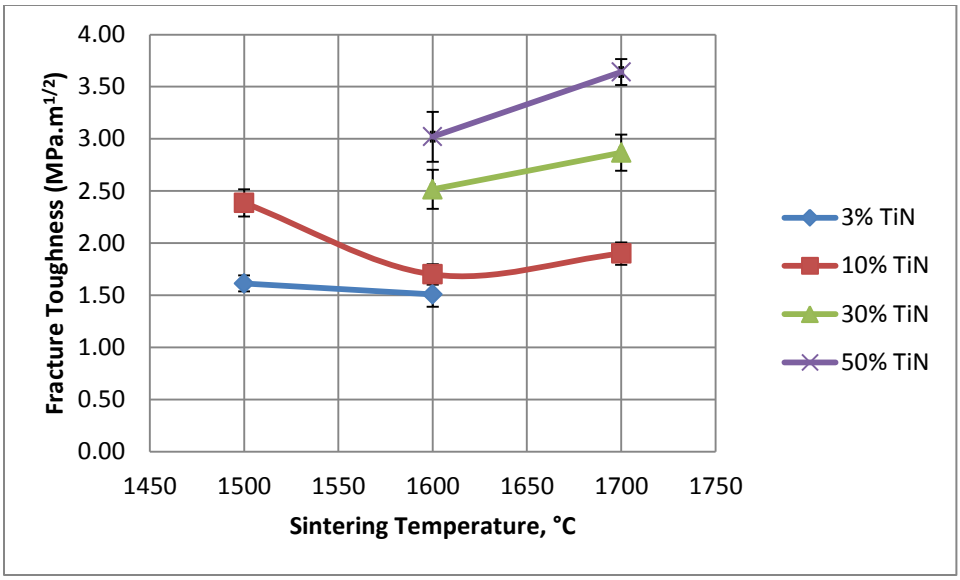

Figure 64: Effect of sintering temperature on fracture toughness of ZrO_2-TiN nanocomposites

The effect of sintering temperature on fracture toughness is shown in Figure 63 and Figure 64 for the ZrO_2-TiC and ZrO_2-TiN nanocomposites respectively, sintered at a pressure of 50 MPa. A similar trend could be seen in both figures which showed that the fracture toughness was increased with increased TiC and TiN content, due to the additional toughening effect of these reinforcing powders. The fracture toughness for each of the TiC and TiN containing composites were in similar ranges for similar volume contents.

For the 30 and 50% TiC content samples it could be seen that the fracture toughness initially decreased with increased sintering temperature and then increaseed with a further increase in temperature. This was most likely due to initial lower densities of the samples, in which there would be an overestimation of the fracture toughness as the presence of pores would prevent a crack from propagating. The increased density as a result of the sintering temperature increasing would initially cause the fracture toughness to decrease, as a result of the porosity decreasing. A further increase in temperature then caused the fracture toughness to increase as a result of the density increase. A similar case was found for the 10%TiN samples. The effect of density on the fracture toughness is further explained in Figure 65.

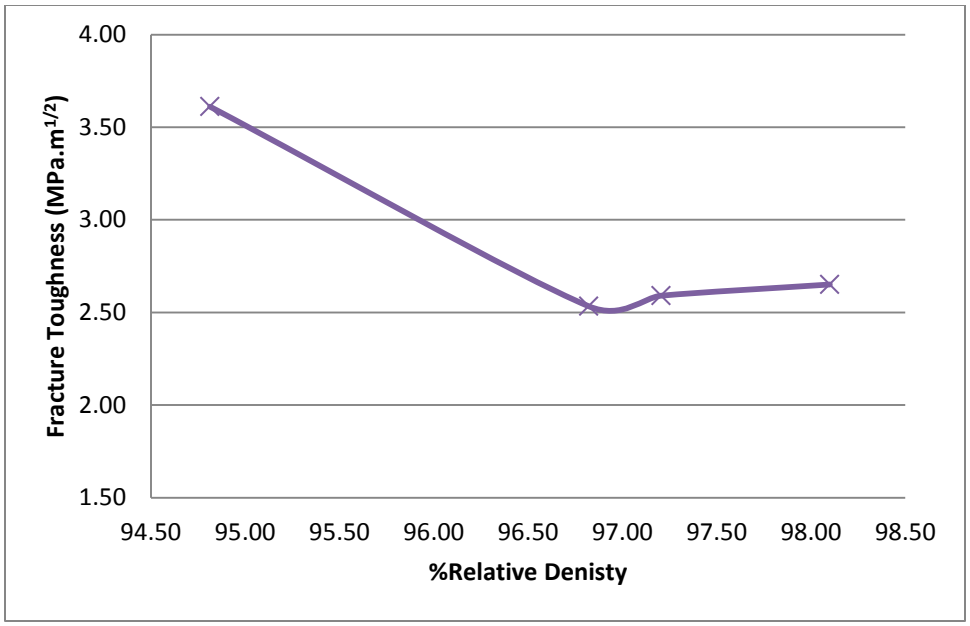

Figure 65: The effect of relative density on fracture toughness of the 50%TiC content samples

From Figure 65, as described earlier, it could be seen that the relative density of the sample caused an increase in the fracture toughness at higher densities, where there was minimal porosity, with the opposite being true for lower densities due to porosity.

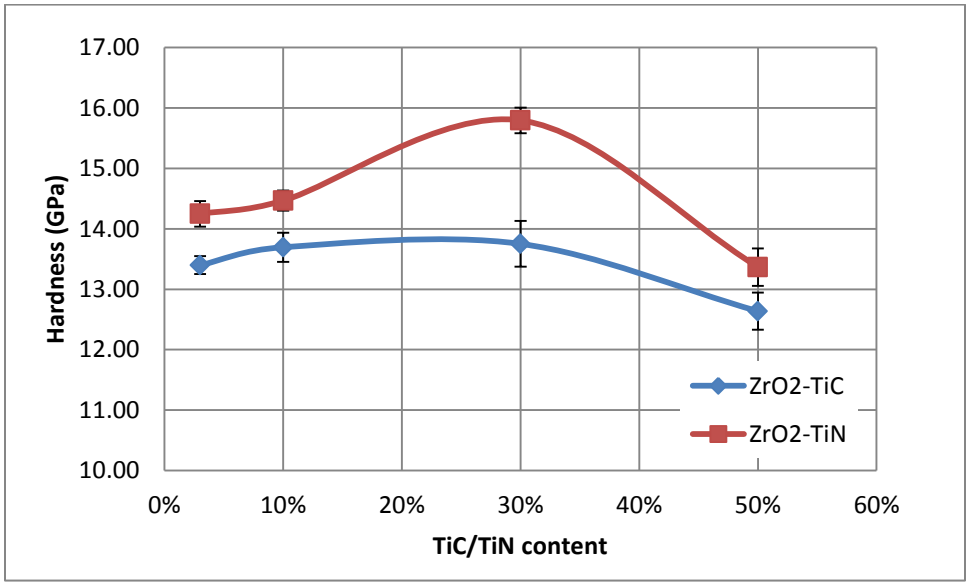

Figure 66: The effect of TiC/TiN content on hardness

Figure 66 shows the effect of increased reinforcing powder content, for both TiC and TiN, on the hardness of the nanocomposite. The samples shown were those with the highest densities for each composition. Both show that the hardness was increasing with increasing TiC and TiN content but decreases at 50 volume percent. 30 volume percent TiC and TiN show the highest hardness.

It could be seen from the SEM images of the samples that the higher reinforced powder content has significantly reduced the grain growth of zirconia, as it was acting as a grain growth inhibitor. This was shown by increased reinforcing powder content resulted in smaller zirconia grains at similar sintering temperatures and that the largest zirconia grains were found in the lower TiC and TiN contents. According to Reed, this effect is most prominent when the reinforcing powder is dispersed homogenously with the matrix powder [(52)]. This effect of the TiC and TiN particles adds to the increased hardness of the higher content composites, due to increased hardness with smaller grain sizes as predicted by the Hall-Petch relationship. This was shown in Figure 66, which indicated that the hardness of samples for varying TiC and TiN contents are increased with increased TiC/TiN content. The reason for the decreased hardness at 50 volume percent was due to the lower relative densities the 50 volume percent samples.

It must be noted also that the TiN samples had a higher hardness than the TiC samples. The grain size for the Zirconia was smaller for similar compositions in the TiN compared to the TiC samples, at similar sintering conditions. Even though TiC is a harder material than TiN, the TiN samples had higher hardness values. This was attributed to the zirconia grain growth hindered more effectively with TiN than the TiC grains, and to the fact that the small grain sizes resulted in higher hardness value as expected by the Hall-Petch relationship. This could also be seen when comparing the grain sizes in the SEM microstructure images of the TiC and TiN nanocomposites.

The mechanical properties of the sintered composites are in similar region to those found in literature. Some of these are shown in the Table 22.

Table 22: Mechanical Properties of similar composites from literature

Material	Particle size	Sintering Conditions	Hardness (Gpa)	Fracture Toughness ($MPa.m^{1/2}$)
8YSZ [53]	28 nm	Isostatically pressed 200 MPa, 1400°C, 2Hr	12.1	1.7
3YSZ [53]	26 nm	Isostatically pressed 200 MPa, 1400°C, 2Hr	12.8	5.8
8Y-ZrO_2/ 5 vol. % SiC [23]	-/90 nm	HP, 1710°C, 20 MPa, 1Hr	13.81	1.27
3Y-ZrO_2/ 35 vol. % TiN [38]	27 nm/1.03 µm	HP, 1550°C, 28 MPa, 1 Hr	13.75	7.1
3Y-ZrO_2/ 50 vol. % TiN [38]	27 nm/1.03 µm	HP, 1550°C, 28 MPa, 1 Hr	13.49	6.3
3Y-ZrO_2/25% TiC [36]	-	Isostatically pressed 350 MPa, 1400°C, 2Hr	11.2	4.6

The hardnesses of the nanocomposites in this report were within the range given in literature, with some sintered samples having slightly higher in that property than that reported in literature. This was similarly found for the fracture toughness of the cubic zirconia and cubic zirconia composites in literature. The fracture toughness of the partially stabilised zirconia had a much higher fracture toughness. This was because of the additional transformation toughening effect in this material, and hence data on composites containing that variant of zirconia could not be used for an accurate comparison. However it must be noted that for biomedical application this would be a far superior ceramic due to this property.

6. Conclusion

From the rheology studies carried out on the micron powders it was found that each of the powders (8Y-ZrO_2, TiC and TiN) could be dispersed using Lubrizol 2155 as a dispersant and hexane as the solvent. This was also found to be the case for the ZrO_2-TiC and the ZrO_2-TiN systems. The surface area of the powders affected the optimal amount of dispersant required with the micron sized zirconia have required a larger amount of dispersant, due to its larger surface area, than the micron sized TiN and TiC. The optimal amount of dispersant was also found to be material dependent, with the optimal amount of dispersant for the micron TiC and TiN required even though they have similar surface areas and particles sizes.

The rheology carried out on the nanopowders showed that due to the finer particle size of these powders and hence a larger surface area they were harder to disperse. Because of this, lower solids loading were used; this also influenced the amount of Lubrizol 2155 required. The influence of the surface area also played the greatest role on the solid loading and the optimal amount of Lubrizol. Again the amount of dispersant was material dependent with the amount of Lubrizol and solids loadings differing greatly for the nanosized zirconia and TiC even though they had similar surface areas and particle sizes.

The densification of the nanocomposites showed that there was a decrease in density with increasing content of the reinforcing powders. This was particularly apparent for the composites that contained above 30 vol. % of the reinforcing component as a result of the percolation limit being surpassed. Due to this the zirconia particles were being restricted by the reinforcing powder to plastically deform and move through the reinforcing powder. This accounted for the low relative densities obtained for the 50 volume percent compositions of the reinforcing powders.

The oxygen contamination played a significant role on the final densities obtained, with the relative densities increasing when accounting for the oxygen content. The corrected densities were consistent with the micrographs of the sintered samples found through SEM.

The nanocomposites showed that there was an increase in the fracture toughness with increased reinforcing component composition. The hardness was found to be dependent on both the reinforcing component additions as well as the density of the material. However, due to the densification having decreased with increased reinforcing component concentration, the increases in hardness that were expected did not materialise. In both systems the highest hardnesses were found in the 30 volume percent samples.

The hardness values of the ZrO_2-TiN system were found to typically be higher than those of the ZrO_2-TiC system. In the ZrO_2-TiC system hardness values of up to 13.40, 13.66, 13.75, 12.64GPa were found for each of the 3%, 10%, 30% and 50% TiC containing systems respectively. In the ZrO_2-TiN system hardness values of up to 14.25, 14.47, 15.79, 13.37 GPa were found for each of the 3%, 10%, 30% and 50% TiN containing systems respectively.

The fracture toughness increased with increased reinforcing component composition for both systems with higher fracture toughness achieved in the TiN system. The highest fracture toughness found, for samples with a relative density above 97 percent, were 2.65 and 3.64 $MPa.m^{1/2}$ respectively for the TiC and TiN systems.

To conclude the use of fully stabilised zirconia, 8Y-ZrO_2, as a bioceramic instead of partially stabilised zirconia, 3Y-ZrO_2, is not advisable due to the low fracture toughness obtained. The nanocomposites made in this work did show better hardness compared to either forms of the pure zirconia, however the fracture toughness values were very low compared to pure 3Y-ZrO_2 and 3Y-ZrO_2-composites.

7. Bibliography

1. **Gross, K.** *Bioceramics – An Overview Including Calcium Phosphates, Hydroxyapatite, Alumina, Zirconia and Pyrolytic Carbon.* AZoM™.com : Azo Materials, 2002.

2. **Japan Medical Materials.** *Bioceramics and their clinical applications.* Cambridge : Woodhead Publishing Limited, 2008. pp. 28-30, 243-263.

3. **Chevalier, J., et al., et al.** *Critical effect of cubic phase on aging in 3 mol% yttria-stabilized zirconia ceramics for hip replacement prosthesis.* s.l. : Elsevier, 2004, Biomaterials, Vol. 25, pp. 5539–5545.

4. **Sharif, A.A., et al., et al.** *Control of grain growth using intergranular silicate phases in cubic yttria stabilized zirconia.* 11, s.l. : Elsevier, 1998, Acta Mater., Vol. 46, pp. 3863-3872.

5. **Li, X, et al., et al.** *Micro/Nanoscale Mechanical and Tribological Characterization of SiC for Orthopedic Applications.* 72, South Carolina : Wiley, 2004, J Biomed Mater Res, Vol. B.

6. **Basu, B.** *Nanoceramics and nanocomposites*.* 5, September 2008, Current Science, Vol. 95.

7. **VaBen, R. and Stover, D.** *Processing and properties of nanophase ceramics. , 92-93 (1999)* . s.l. : Elsevier, 1999, Journal of Materials Processing Technology, Vols. 92-93, pp. 77-84.

8. **Best, S.M., et al., et al.** *Bioceramics: Past, present and for the future.* 28, Cambridge : Elsevier, 2008, Journal of the European Ceramic Society, Vol. 1.

9. **Lewis, K., et al., et al.** *Bioceramics – The Changing Role of Ceramics and Nanoceramics in Medical Applications.* 3, 2007, Materials Australia Magazine, Vol. 40.

10. **Doremus, R.H.** *Review Bioceramics.* 27, 1992, Journal Of Material Science, Vol. 1.

11. **Hench, L. L.** *Bioceramics: From concept to clinic.* 1991, Journal of the American Ceramic Society, Vol. 77, pp. pp. 1487-1510.

12. **Chraska, T., King, A.H. and Berndt, C.C.** *On the size-dependent phase transformation in nanoparticulate zriconia.* New York : Elsevier, 2000, Materials Science and Engineering A , Vol. 266, pp. 169 – 178.

13. **Tekeli, S. and Demir, U.** *Colloidal processing, sintering and static grain growth behaviour of alumina-doped cubic zirconia.* s.l. : Elsevier, 2005, Ceramics International, Vol. 31, pp. 973–980.

14. **Smallman, R E and Bishop, R.J.** *Modern Physical Metallurgy and Materials Engineering 6th ed.* Oxford : Butterworth-Heinemann, 1999. pp. 330-331.

15. **Kumara, B.V.M, et al., et al.** *Effect of grain size on wear behavior in Y-TZP ceramics.* 527, Seoul : Elsevier, 2009, Materials Science and Engineering, Vol. A, pp. 474–479.

16. **Averback, R.S, Hofler, H.J and Tao, R.** *Processing of nano-grained materials.* 166, 1993, Materials Science and Engineering, Vol. A, pp. 169-177 .

17. **Brinkiene, K. and Kezelis, R.** *Effect of alumina addition on the microstructure of plasma sprayed YSZ.* s.l. : Elsevier, 2005, Journal of the European Ceramic Society 25 (2005), Vol. 25, pp. 2181–2184.

18. **Edelstein, A.S and Cammarata, R.C.** *Nanomaterials: synthesis, properties, and applications.* Abingdon : Taylor & Francis Group, 1996. pp. 57-59.

19. **Rahaman, MN.** *Ceramic processing and sinterind (2nd ed.).* New York : Dekker, 2003. pp. 30-32, 343.

20. **Rahaman, M.N.** *Ceramic Processing and Sintering 2nd ed.* 2nd. New York : Marcel Dekker, 2003. pp. 230-233, 828, 778-779.

21. **Zhanga, J, et al., et al.** *Aqueous processing of fine ZrO2 particles.* Osaka : Elsevier, 2005, Colloids and Surfaces A: Physicochem. Eng. Aspect, Vol. A254, pp. 199–205.

22. **Tulliani, J.M, et al., et al.** *Porous alumina and zirconia bodies obtained by a novel gel casting process.* s.l. : Wiley, January-February 2008, Advances in bioceramics and porous ceramics.

23. **Donzel, L. and Roberts, S.G.** *Microstructure and mechanical properties of cubic zirconia (8YSZ)/SiC nanocomposites.* Oxford : Elsevier, 2000, Journal of the European Ceramic Society, Vol. 20, pp. 2457-2462.

24. **Rao, S.R, Tripathy, S.S and Raichur, A.M.** *Dispersion studies of sub-micron zirconia using Dolapix CE 64.* Bangalore : Elsevier, 2007, Colloids and Surfaces A: Physicochem. Eng. Aspects, Vol. A302, pp. 553–558.

25. **Bamba, N., et al., et al.** *Mechanical properties and microstructure for 3 mol% yttria doped zirconia silicon carbide nanocomposites.* Osaka : Elsevier, 2002, Vol. 23.

26. **Riedel, R. and Chen, I.W.** *Ceramics Science and Technology.* s.l. : John Wiley & Sons, 2011. Vol. 1: Structures.

27. **Aalund, Robert.** Spark Plasma Sintering. *Ceramic Industry.* [Online] May 1, 2008 . [Cited: April 4, 2010.] http://www.ceramicindustry.com/Articles/Feature_Article/BNP_GUID_9-5-2006_A_10000000000000321084.

28. **Rogers, B.** Hot-Press Furnace Systems Handle Extreme Operating Conditions. *Industrial Heating.* [Online] September 14, 2004 . [Cited: April 8, 2010.] http://www.industrialheating.com/Articles/Feature_Article/f9f65c9915cb7010VgnVCM100000f932a8c0.

29. **Barsoum, M.W.** *Fundamental of Ceramics.* Bristol and Philadelphia : Institute of Physics Publishing, 2003. p. 343.

30. **Jian, J., et al., et al.** *Electrical property of 8-mol% yttria-stabilized zirconia electrolyte by spark-plasma sintering.* 5, 2004, Science in China Ser. E Engineering & Material Science, Vol. 47, pp. 569-576.

31. **Takeuchi, T., et al., et al.** *Improvement of Mechanical Strength of 8 mol % Yttria-Stabilized Zirconia Ceramics by Spark-Plasma Sintering.* 4, 2002, Journal of The Electrochemical Society, Vol. 149, pp. A455-A461.

32. **Chen, X.J., et al., et al.** *Preparation yttria-stabilized zirconia electrolyte by spark-plasma sintering.* Singapore : Elsevier, 2002, Materials Science and Engineering A, Vol. 341, pp. 43-48.

33. **Chen, L., Jia, C. and Wang, K.***Spark plasma sintering of high-toughness ZrO2 materials doped with yttrium.* 5, Beijing : Elsevier, 2008, Rare Metals, Vol. 27, pp. 479-483 .

34. **Li, J, Hermansson, R and Soremark, R.** *High-strength biofunctional zirconia: mechanical properties and static fatigue behaviour of zirconia-apatite composites.* 1993, Journal of Materials Science: Materials In Medcine, Vol. 4, pp. 50-54.

35. **Ran, S and Gao, L.** *Mechanical properties and microstructure of TiN/TZP nanocomposites.* 447, Shanghai : Elsevier, 2007, Materials Science and Engineering A, Vol. A, pp. 83–86.

36. **Pyda, W.** *Microstructure and properties of zirconia-based nanocomposites derived from a powder containing TiC crystallised in situ and carbon.* Cracow : Elsevier, 2004, Ceramics International, Vol. 30, pp. 333–342.

37. **Haberko, K., et al., et al.** *A TZP matrix composite with in situ grown TiC inclusions.* s.l. : Elsevier, 2000, Journal of the European Ceramic Society, Vol. 20, pp. 2649 - 2654.

38. **Salehi, S., Van der Biest, O. and Vleugels, J.** *Electrically conductive ZrO2–TiN composites.* s.l. : Elsevier, 2006, Journal of the European Ceramic Society, Vol. 26, pp. 3173–3179.

39. **Yoshimura, M, et al., et al.** *Rapid rate sintering of nano-grained ZrO2-based composites using pulse electric current sintering method.* 17, 1988, Journal of Materials Science Letters, pp. 1389-1391.

40. **Liu, D.** *Densification of zirconia from submicron-sized to nano-sized powder particles.* s.l. : Chapman & Hall, 1998, Journal of Materials Science Letters, Vol. 17, pp. 467-469.

41. **Nygren, M. and Shen, Z.** *On the preparation of bio-, nano- and structural ceramics and composites by spark plasma sintering.* 5, s.l. : Elsevier, 2002, Solid State Sciences.

42. **German, R.M. and Park, S.J.** *Mathematical relations in particulate materials processing: ceramics, powder metals, cermets, carbides, hard materials, and minerals.* s.l. : John Wiley & Sons, 2008. p. 419.

43. **Fischer-Cripps, A.C.** *Nanoindentation.* 3rd. s.l. : Springer, 2011.

44. **D Casellas, I Ràfols, L Llanes, M Anglada.** *Fracture toughness of zirconia–alumina composites.* 1-3, s.l. : Elsevier, 1998, International Journal of Refractory Metals and Hard Materials, Vol. 17.

45. **Tekeli, S.** *Fracture toughness (KIC), hardness, sintering and grain growth behaviour of 8YSCZ/Al2O3 composites produced by colloidal processing.* 1-2, s.l. : Elsevier, 2004, Journal of Alloys and Compounds, Vol. 391.

46. **Tosoh.** Zirconia Powders TZ Series. *Tosoh Products.* [Online] [Cited: November 27, 2011.] http://www.tosoh.com/Products/basic_grades.htm.

47. **Basu, B. and Balani, K.** *Advanced Structural Ceramics.* New Jersey : John Wiley & Sons, 2011. p. 329.

48. **Santos, E. and Schmickler, W.** *Catalysis In Electrochemistry: From fundamental Aspects to Strategies for Fuel Cell Developemwnt.* s.l. : John Wiley & Sons, 2011. pp. 385-386.

49. **Lin, C.L., Gan, D. and Shen, P.** *The Effects of TiO2 Addition on the Microstructure and Transformation of ZrO z with 3 and 6 mol.% Y203.* 129, Kaohsiung : Elsevier, 1990, Materials Science and Engineering, Vol. A, pp. 147-155.

50. **Capel, F., et al., et al.** *Structure and electrical behavior in air of TiO2-doped stabilized tetragonal zirconia ceramics.* 68, s.l. : Springer, 1999, Applied Physics, Vol. A: Materials Science & Processing, pp. 41–48.

51. **Tsukuma, K.***Transparent titania-yttria-zirconia ceramics.* s.l. : Chapman and Hall Ltd., 1986, Journal of Material Science Letters, Vol. 5, pp. 1143-1144.

52. **Reed, J.S.** *Principles of ceramics processing.* 2nd. New York : John Wiley and Sons, Inc., 1995.

53. **Ghatee, M., Shariat, M.H and Irvine, J.T.S.** *Investigation of electrical and mechanical properties of 3YSZ/8YSZ composite electrolytes.* s.l. : Elsevier, 2009, Solid State Ionics, Vol. 180.

Appendix A – Archimedes' Principle

$$True\ Volume\ of\ sample = \frac{W_1 - W_3}{\rho_w} \quad \textbf{Equation 7}$$

$$True\ Density\ of\ sample = \frac{W_1 \rho_w}{W_1 - W_3} \quad \textbf{Equation 8}$$

$$Volume\ of\ Open\ Porosity = \frac{W_2 - W_1}{\rho_w} \quad \textbf{Equation 9}$$

$$\begin{aligned} Bulk\ Volume \\ &= Volume\ of\ Sample \\ &- Volume\ of\ Open\ Porosity \end{aligned} \quad \textbf{Equation 10}$$

$$Bulk\ Volume = \frac{W_1 - W_3}{\rho_w} + \frac{W_2 - W_1}{\rho_w} = \frac{W_2 - W_3}{\rho_w}$$

$$Bulk\ Density = \frac{W_1 \rho_w}{W_2 - W_3} \quad \textbf{Equation 11}$$

$$Volume\ Fraction\ of\ Open\ Porosity = \frac{W_2 - W_1}{W_2 - W_3} \quad \textbf{Equation 12}$$

Appendix B – Theoretical Density

$$\frac{1}{\rho} = \frac{x_A}{\rho_A} + \frac{x_B}{\rho_B} + \frac{x_C}{\rho_C} \qquad \textbf{Equation 13}$$

Where;

ρ = Theoretical Density of the Material (g/cm^3)

x_A = Mass Fraction of Material A

x_B = Mass Fraction of Material B

x_C = Mass Fraction of Material C – if necessary

ρ_A = Theoretical Density of the Material A (g/cm^3)

ρ_B = Theoretical Density of the Material B (g/cm^3)

ρ_C = Theoretical Density of the Material C (g/cm^3) – if necessary

Appendix C – Equations for Oxygen Content

How theoretical densities with oxygen content was calculated

First the moles of oxygen was calculated using

$$\boldsymbol{M_{O_2} = (M_{TiX})\left(\frac{x}{100}\right)/M_{wO_2}} \qquad \textbf{Equation 14}$$

Where

M_{TiX} is the mass of TiC/TiN used in the sample (if no oxidation took place)

n_{O_2} is the number of moles of oxygen in the TiN powder (mol)

x is the weight percent oxygen found from the leco test (wt%)

M_{wo_2} is the molecular weight of oxygen (32 g.mol^{-1})

The total mass of TiO_2 was then calculated using the following equation, since there is one mole of oxygen per mole of TiO_2 present

$$\boldsymbol{M_{TiO_2} = n_{O_2}.M_{wTiO_2}} \qquad \textbf{Equation 15}$$

Where

M_{wTiO_2} is the molecular weight of TiO_2 (80 g.mol^{-1})

The mass of TiC/TiN was calculated using the following

$$\boldsymbol{M_{TiC/TiN} = M_{TiX} - M_{TiO_2}} \qquad \textbf{Equation 16}$$

Where

$M_{TiC/TiC}$ is the actual mass of TiC/TiN used in the sample

Using the mass of the TiO_2 and new mass for TiN/TiC a new theoretical density could be calculated using Equation 13.